Using VOCALS REx C-130 aircraft measurements to understand aerosol-cloud-precipitation interactions in marine stratocumulus

Christopher R. Terai

A dissertation
submitted in partial fulfillment of the
requirements for the degree of

Doctor of Philosophy

University of Washington

2014

Reading Committee:

Robert Wood, Chair

Christopher S. Bretherton, Chair

Sandra E. Yuter

Program Authorized to Offer Degree:
Atmospheric Sciences

University of Washington

Abstract

Using VOCALS REx C-130 aircraft measurements to understand aerosol-cloud-precipitation interactions in marine stratocumulus

Christopher R. Terai

Co-Chairs of the Supervisory Committee:
Professor Robert Wood
Atmospheric Sciences

Professor Christopher S. Bretherton
Atmospheric Sciences

The high albedo and weak greenhouse-effect of marine stratocumulus provide a strong cooling effect on the regional climate. The concentrations of aerosols, particularly those large enough to act as cloud condensation nuclei, can influence the properties of marine stratocumulus by modifying the cloud droplet size distributions and influencing drizzle production.

This dissertation mainly presents results inferred from aircraft measurements taken aboard the NSF/NCAR C-130 research flights flown during the VOCALS Regional Experiment (Oct. to Nov. 2008). These measurements are used to shed light on the interaction between the marine stratocumulus and aerosol particles. Satellite retrievals and simple models are also used to identify and simulate the various processes that modulate aerosol concentrations and drizzle formation. The dissertation is organized into the following three sections:

- Characterizing pocket of open cells (POC)

  The aerosol, cloud, precipitation, and boundary layer properties from five POCs are studied using measurements from the C-130 aircraft. We find that POCs are observed in a wide range of conditions (inversion heights, surface wind speeds, surface and free tropospheric conditions, and background accumulation-mode aerosol concentrations).

Despite the wide range of background conditions that POCs are observed under, they all exhibit low cloud droplet number concentrations, higher column maximum precipitation rates, and a narrow range of accumulation-mode aerosol concentrations in the subcloud layer. In all POCs, an ultraclean layer exists below the inversion, where accumulation-model aerosol concentrations are $< 5\,\mathrm{cm}^{-3}$. All POCs are also populated by two types of clouds: deeper, cumuliform, active clouds and thin, stratiform, quiescent clouds.

- Estimating the microphysical process rates in POCs

  Using the same C-130 aircraft data, the collision-coalescence rates in POCs are estimated to quantify the various budgets of cloud droplet number concentration, drizzle number concentration, cloud water mixing ratio, and drizzle water mixing ratio. The rates in POC clouds are compared to rates in the surrounding overcast clouds. Accretion is found to be the largest contributor to both the loss of cloud droplet number concentration and the conversion of cloud water into drizzle water. Although decreases in cloud droplet number concentration due to accretion are not always stronger in POC compared to the surrounding overcast region, because of the lower cloud droplet number concentrations, the timescales of cleaning out cloud droplets is shorter in the POC. A parcel model with bin microphysics is employed to determine whether collision coalescence processes can explain the high concentration of drizzle drops with radii $< 100\,\mu$m in quiescent clouds of POCs. Collision-coalescence of drops and condensation due to typical updraft speeds found in POCs are unable to explain the high concentration of drizzle drops.

- Comparing the precipitation susceptibility of marine stratocumulus from satellite retrievals and a diagnostic precipitation model

  A combined MODIS and CloudSat satellite dataset of coincident cloud and drizzle properties and a diagnostic precipitation model with stochastically perturbed micro-

physics are used to calculate the precipitation susceptibility in marine stratocumulus. The precipitation susceptibility quantifies the fractional decrease in precipitation rate due to a fractional increase in cloud droplet number concentration, such that a positive susceptibility means a suppression of precipitation due to increasing precipitation rate. Precipitation susceptibility are found to be positive in both satellite and model precipitation. Both satellite and model precipitation also show decreases in the susceptibility of probability of precipitation (POP) with increasing LWP, where the values largely agree between the two. Model sensitivities to parameter choices and regional differences in the satellite data are explored. Finally, the connection between susceptibility values and collision-coalescence processes (autoconversion and accretion) in the model are investigated. Although previous studies found that increasing ratio between accretion and autoconversion (A_c/A_u) explained decreases in susceptibilities, the modeling results show that this is not always the case.

TABLE OF CONTENTS

LIST OF FIGURES

LIST OF TABLES

GLOSSARY AND ABBREVIATIONS

AEROSOL: A colloidal system in which the dispersed phase is composed of either solid or liquid particles, and in which the dispersion medium is some gas, usually air. [AMS glossary] In the text, the term is used interchangeably to refer to the colloidal system or the particles.

BOUNDARY LAYER: The bottom layer of the troposphere that is in contact with the surface of the earth. [AMS glossary]

STRATOCUMULUS: A principal cloud type (cloud genus), predominantly stratiform, in the form of a gray and/or whitish layer or patch, which nearly always has dark parts and is nonfibrous (except for virga). [AMS glossary]

A_C: accretion rate

A_U: autoconversion rate

LWP: cloud liquid water path

POC: pocket of open cells

POP: probability of precipitation

VAMOS: Variability of the American Monsoon Systems

VOCALS-REX: VAMOS Ocean-Cloud-Aerosol-Land Study Regional Experiment

ACKNOWLEDGMENTS

Many people have helped me along during my graduate studies to make this dissertation what it is. First, I wish to thank Rob Wood for being a fantastic advisor and mentor. I've learned much from the countless conversations I have had with him. Rob's enthusiastic urging to explore different questions, datasets, and skill sets have helped me grow and learn in directions I had not expected, leading to the projects discussed in this thesis. I also wish to thank Chris Bretherton for the guidance provided throughout my graduate studies, often taking the form of questions that have pointed me towards different ways of thinking about problems and findings, which have allowed me to discover new research directions.

I wish to thank Sandra Yuter for taking the time to read through the dissertation and providing extensive feedback on the chapters. The dissertation has much improved in clarity because of the specific comments. I wish to thank Bob Houze for being on my PhD committee as well as providing insights that come out of comparing marine stratocumulus with deep convection. I also wish to thank Alberto Aliseda and Peter Shaffer for being on my committee and providing an outside perspective.

The majority of the work presented in this dissertation is made possible because of the efforts of the scientists, staff, ground-crew and aircrew at the NCAR Research Aviation Facility, and the C-130 scientists who were instrumental in the collection of the aircraft data during VOCALS-REx. The funding for this work was provided by the National Science Foundation grants ATM-0745702 and AGS-1242639.

Various parts of the dissertation have also been developed and clarified from fruitful discussions and collaborations with Andrew Gettelman, Terrence Kubar, Gallia Painter, and Hugh Morrison.

I wish to acknowledge and thank the faculty and staff of the Department of Atmospheric Sciences and of the Program on Climate Change who have engendered a sense of community

and collegiality that has made my graduate education very enjoyable. I wish to thank the help of and great conversations with my officemates Andy Berner and Bryce Harrop. Both have acted as great resources and sources of laughter for almost any problem I encountered. They are the first people I have gone to for help.

I have made good friends during my time in Seattle. My graduate career will not have been as enjoyable, productive, and fulfilling had it not been for your friendship. And finally, I thank my family for encouraging me to pursue my curiosity and for the endless support for whatever path I have chosen.

DEDICATION

To all the teachers and mentors who have helped and inspired me to learn.

Chapter 1

INTRODUCTION

Clouds, especially low-level marine stratocumulus, have a strong cooling effect on the underlying ocean and the atmospheric boundary layer. These same clouds, when examined at the scale of the cloud droplet, form from the condensation of water vapor onto submicron-sized aerosol particles suspended in the air. In conditions observed in our current atmosphere, clouds cannot form except for the existence of these aerosol particles. Of all aerosol particles, those with radii $> 0.1\,\mu$m will activate under typical supersaturations reached in clouds and are defined as cloud condensation nuclei (CCN). Their concentrations are largely captured by the concentration of accumulation-mode aerosols, which are defined by a size range of 0.1 to $1\,\mu$m [Martin et al., 1994, Seinfeld and Pandis, 2006]. When cloud formation is examined at these scales, it is apparent that the concentration of accumulation-mode aerosols can have a strong influence on cloud properties.

However, when global cloud properties are examined, the geographic distribution of cloud types are largely determined by large-scale dynamics and thermodynamic profiles [Eastman et al., 2011, Atkinson and Zhang, 1996]. Even at the regional scale, meteorological influences are the main drivers that influence the formation and radiative properties of observed clouds [George and Wood, 2010, Mechem et al., 2012]. This confounds attempts to quantify the effect that variations of aerosol concentrations have on cloud properties, commonly known as aerosol indirect effects [AIE - Quaas et al., 2009] or aerosol-cloud interactions [ACI - Boucher et al., 2013].

This poses a problem as increasing numbers of modeling groups have started incorporating representations of cloud physics that try to capture the aerosol-cloud interactions. For example, there are large discrepancies amongst models on the role of anthropogenic aerosols on cloud radiative properties [Quaas et al., 2009]. At the same time, it appears that model estimates of the strength of the ACI and estimates based on satellite retrievals do not agree;

models show a stronger ACI than what satellite retrievals indicate [Boucher et al., 2013]. This issue stems not only from our lack of understanding of aerosol-cloud interactions, but also from our lack of understanding of how large-scale dynamics and thermodynamics influence cloud formation. Observationally, the meteorological effect and aerosol effect are difficult to disentangle from each other [Mauger and Norris, 2007, George and Wood, 2010].

This dissertation contains two approaches to better understand the ACI in marine stratocumulus. The data used here are largely based on measurements collected by the NCAR/NSF C-130 flown during the VOCALS Regional Experiment [Wood et al., 2011b]. The following two chapters describe the properties and inferred process rates in pockets of open cells (POCs). Properties of the clouds in the POCs are distinctly different from those in the surrounding area. At the same time large-scale dynamic and thermodynamic fields have been found to be similar over the POCs. This combination makes POCs a particularly interesting natural laboratory where processes internal to the atmospheric boundary layer are likely maintaining and possibly forming these pockets where cloud properties are drastically different.

The following chapter takes a different approach to examine ACI and examines a particular step in the range of possible aerosol-cloud interactions, namely the influence of cloud droplet number concentration on precipitation. Various estimates exist and a recent study [Wang et al., 2012] indicates that the sensitivity of precipitation to aerosol concentrations in models is higher than what is observed by satellites. This work extends on their work to identify whether this is the case and what particular aspects of the models may lead to discrepancies between the model and observations.

The dissertation is organized as follows. Chapter 2 examines the cloud, boundary layer, and lower free tropospheric properties in and around POCs. Chapter 3 estimates the in-cloud collision-coalescence properties that determine both drizzle formation and CCN concentration losses in the POCs. Chapter 4 examines the precipitation susceptibility metric in marine stratocumulus in both satellite retrievals and a column precipitation model with a diagnostic treatment of precipitation. Chapter 5 provides a summary of results and remaining questions and issues that follow on from the work presented here.

Chapter 2

CHARACTERISTICS OF POCKETS OF OPEN CELLS

A large part of the following chapter has been published in Atmospheric Chemistry and Physics Discussion under the citation, Terai et al. [2014].

2.1 Introduction

During most of the year, a large stratocumulus cloud deck covers the southeast Pacific Ocean (SEP), extending westward from the South American continent. Due to a strong albedo and weak greenhouse effect, the stratocumulus exerts a strong cooling effect on the ocean and the atmospheric boundary layer [de Szoeke et al., 2012]. The extensive stratocumulus cloud deck is occasionally interrupted by cloud breaks in the form of pockets of open cells, where the lower cloud cover exposes the darker sea surface, effectively lowering the albedo of the area where these features form.

Pockets of open cells (POCs) have previously been defined as regions of open-cell convection completely or largely embedded within a larger region of closed-cell convection [Stevens et al., 2005, Wood et al., 2008]. In regions of open-cell convection, patches of descending clear air are ringed by ascending cloudy air, giving it a honeycomb-like pattern when viewed from above. On the other hand, closed-cell convection are characterized by patches of cloudy ascending air that are ringed by clearer descending air, leading to higher albedos [Atkinson and Zhang, 1996, Wood and Hartmann, 2006]. Subsequent studies have found, however, that POCs also support thin and extensive stratiform clouds in addition to the honeycomb-like patterns or isolated clusters of deeper cumulus clouds [Wood et al., 2011a] and that horizontal gradients in cloud microphysical properties exist at the transition from closed to open cellular convection, with often dramatic decreases in cloud droplet number concentrations inside the POCs [Stevens et al., 2005, Sharon et al., 2006, Wood et al., 2008, 2011a]. In this paper, POCs are defined as regions of broken cumuliform convection,

possibly overlaid by thin patchy stratocumulus, that (a) are embedded within regions of closed-cell stratocumulus clouds and (b) that also show cloud microphysical changes at the transition, evident in daytime satellite images as an increase in cloud effective radius at the POC edges. This stricter definition of POCs excludes instances of cloud break up that accompany cloud thinning due to increased subsidence and evaporation, and also many cloud breaks at the western edge of stratocumulus cloud decks.

POCs have been observed in satellite imagery [Garay et al., 2004] and in various field experiments [Bretherton et al., 2004, Stevens et al., 2005, Sharon et al., 2006, Wood et al., 2011a, Cui et al., 2014]. Because the cloud cover is relatively low in POCs, their formation can influence the amount of incident solar radiation that is absorbed at the Earth's surface. Up to 10–15 % of the southeast Pacific region can be covered by open cells during the October and November months of extensive cloud cover [Wood et al., 2008]. Although regional models have started to simulate episodic changes in cloud cover and albedo due to synoptic forcing [Abel et al., 2010] and transport of aerosol plumes from coastal pollution sources [Yang et al., 2011, Saide et al., 2012, George et al., 2013], models still do not clearly demonstrate the formation of reduced cloud cover in the form of POCs [Abel et al., 2010, Toniazzo et al., 2011]. An exception exists for Mechem and Kogan [2003] who employed a nested 2 km resolution mesoscale model within a larger regional model to form drizzle-induced cloud break up in overcast stratocumulus. The low aerosol concentrations observed within POCs [Petters et al., 2006, Sharon et al., 2006, Wood et al., 2008, 2011a] strongly suggest a mechanism by which aerosols affect clouds and suggest the need to incorporate aerosol–cloud interactions occurring on scales of a few kilometers and smaller to simulate POC formation in models.

Various aspects of the POCs have been convincingly simulated by large-eddy simulations (LES) and high-resolution, cloud-resolving simulations [Wang and Feingold, 2009a,b, Wang et al., 2010, Berner et al., 2011, Kazil et al., 2011, Berner et al., 2013]. Several of these studies initialize a region of the model domain with lower cloud droplet number concentration to initiate POC formation [e.g., Wang and Feingold, 2009a,b, Berner et al., 2011]. The simulations point to the importance of cold pools in transforming closed-cell circulation to open-cell circulation [Wang et al., 2010], and indicate horizontal coupling of inversion

heights that allows for the coexistence of closed-cell and open-cell clouds within a region of hundreds of kilometers [Berner et al., 2011]. Kazil et al. [2011] implemented a more sophisticated model of the sulfur cycle and aerosol processing within an LES and was able to reproduce the observed structure of the aerosol-depleted "ultraclean layer" [as detailed in observations by Wood et al., 2011a] and its potential for supporting spontaneous nucleation of ultrafine aerosol. More recently, Berner et al. [2013] showed that a large-domain cloud-resolving simulation with interactive aerosols can develop long-lived, mutually-supporting regions of open and closed cells existing side by side, suggesting that under some large-scale meteorological and aerosol conditions, the POC-overcast system is a self-maintaining form of mesoscale cloud organization. POC modeling studies have been initialized based on one DYCOMS-II RF02 case [Wang and Feingold, 2009a,b] and one VOCALS case, RF06 [Wang et al., 2010, Berner et al., 2011, Kazil et al., 2011]. The boundary layer heights of the two cases range from 800 m [VanZanten and Stevens, 2005] to 1600 m [Wood et al., 2011a], suggesting diverse environments in which POCs exist. More observational analyses of POCs are therefore necessary to identify the boundary layer properties that are common across different POC cases and those properties that are more variable.

Early observations of POCs were fortuitous because their formation cannot be easily forecast and because they form over remote oceans. The VAMOS Ocean Cloud Atmosphere Land Study Regional Experiment (VOCALS REx), conducted over the southeast Pacific Ocean during October and November of 2008, was the first concerted field campaign for which POCs developing in a larger region were systematically targeted for observational sampling [Wood et al., 2011b, Mechoso et al., 2014]. Wood et al. [2011a] provides a detailed analysis of one VOCALS case (RF06) using data from two aircraft. Cui et al. [2014] describe measurements from another VOCALS POC case sampled by the UK BAe-146 aircraft before the C-130 sampled it during RF13. The current study investigates the commonalities and variations across five different VOCALS POC cases, including RF06 and RF13. We assess our current conceptual model of POC structure and the conditions necessary to form and maintain them. Section 2.2 gives an overview of the measurements available from the C-130 and describes how POCs are differentiated from the surrounding overcast region using satellite infrared imagery. The following five sections present our results, including the large

scale context in which the POCs were observed (Sect. 2.3) and comparisons of their boundary layer (Sect. 2.4), cloud and precipitation (Sect. 2.5), and aerosol (Sect. 2.6) characteristics with the surrounding overcast regions and two POC-like cases (Sect. 2.7). A discussion and summary of the results is given in Sect. 2.8.

2.2 Data and methods

2.2.1 Data

During VOCALS REx, six research flights flown by the NSF/NCAR C-130 sampled the atmospheric conditions across transitions from closed-to-open cellular clouds accompanied by clear corresponding changes in cloud microphysics [Wood et al., 2011b]. Five of those six research flights are used in this analysis, because the diurnal break-up of the closed-cell stratocumulus made it difficult to distinguish the closed-cell from the open-cell regions during RF14 (15 November). The five remaining research flights examined here are RF06 (28 October), RF07 (31 October), RF08 (2 November), RF09 (4 November), and RF13 (13 November). During VOCALS-REx, if a suspected POC was present within aircraft range when flight plans were made for a given day, the C-130 was directed to sample the POC. The flight strategy consists of sawtooth profile legs from above the inversion to below cloud base, profile legs through the depth of the atmospheric boundary layer, and level flight legs flown ~ 150 m above the surface in the subcloud layer, at cloud base (~ 700 m), at cloud level (~ 1000 m), and above cloud (~ 1500 m). Level flight legs ranged in length from 120 to 240 km. Figure 2.1 shows a typical flight strategy of POC sampling, followed by most flights, except for RF06 and RF13, in which an additional subcloud and cloud level flight leg was flown.

For all flight legs, a suite of instruments measured thermodynamic quantities [temperature, water mixing ratio, pressure, etc., described in Wood et al., 2011b] to help characterize the structure of the boundary layer and lower free troposphere. Because the humidity measurements were found to be biased high in previous analyses [Bretherton et al., 2010], the humidity measurements from the Lyman-alpha hygrometer are corrected according to Bretherton et al. [2010]. The Wyoming Cloud Radar (WCR), also aboard the C-130, pro-

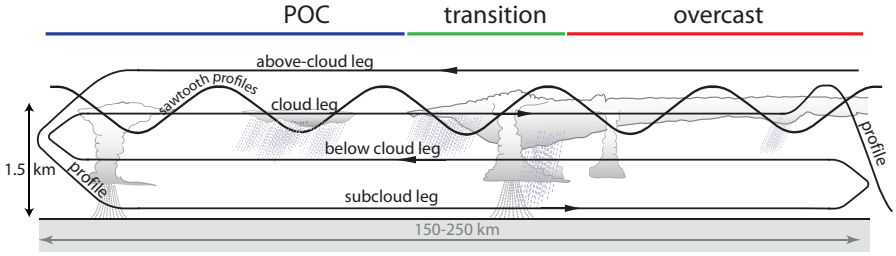

Figure 2.1: Typical flight strategy taken by the NSF/NCAR C-130 during POC sampling [adapted from Fig. 7 of Wood et al., 2011a].

vided radar reflectivity from cloud and precipitation hydrometeors above and below the aircraft. The column-maximum reflectivity from the WCR is used to estimate precipitation rates at cloud base inside and outside the POCs using the Z–R relationship from Comstock et al. [2004]. From the subcloud flight legs, the cloud fraction, cloud base height, and cloud liquid water path are estimated using the upward pointing Wyoming Cloud Lidar (WCL) and G-band Vapor Radiometer (GVR) [Zuidema et al., 2012], respectively. Sea surface temperatures (SSTs) are remotely sensed by downward viewing Heimann radiometric sensors and corrected by 1 K to correct a warm bias found by Bretherton et al. [2010].

Concentrations of aerosols of size $> 0.1\,\mu$m in clear air are obtained from the Passive Cavity Aerosol Spectrometer Probe (PCASP) that measures the size distribution of aerosols with diameter between 0.1 and 3 μm. This size range encompasses most of the accumulation-mode aerosols and is representative of concentrations of cloud condensation nuclei (CCN) at supersaturations typical of those in marine stratocumulus [Martin et al., 1994, Terai et al., 2012]. Total aerosol concentrations (CN) for particle diameters > 10 nm were obtained by the 3010 CN Counter [Clarke et al., 2007]. Aerosol data are all filtered for possible splashing and shattering events from drizzle drops by removing aerosol data if any of the following conditions are met: liquid water content $> 0.04\,\mathrm{g\,m^{-3}}$ (as measured by the Gerber PV-100 Probe); drizzle drop concentration $> 1\,\mathrm{L^{-1}}$ (as measured by the 2DC Probe); a 10 s-forward-lagged, 11 s-moving-window-mean drizzle water content $> 10^{-4}\,\mathrm{g\,m^{-3}}$ (as measured by the 2DC Probe).

Measurements of cloud droplet concentrations (N_d) and mixing ratios (q_c) are obtained

from a Cloud Droplet Probe (CDP), which measures drops with radii between 1 and 23.5 μm. Similarly, measurements of drizzle drop concentrations (N_{D}) and mixing ratios (q_{D}) are obtained from a 2DC optical array probe for drops with radii larger than 30 μm [Wood et al., 2011b]. Unless otherwise stated, all measurements are analyzed at 1 Hz time resolution, corresponding to a spatial resolution of $\sim$ 100 m. Cloudy air is distinguished from clear air in the cloud-level flight legs when the liquid water mixing ratio from either the Gerber PV-100 Probe or the CDP+2DC exceeded 0.03 g kg^{-1}.

In order to locate the POC boundaries regardless of the time of day, infrared brightness temperature imagery from Channel 4 (centered on 11 μm) of the Geostationary Operational Environmental Satellite imager (GOES-10), obtained roughly every fifteen minutes, is used to locate the flight legs in relation to the POC boundary.

2.2.2 Differentiating between POC and overcast regions

We divide each relevant flight leg into POC, transition, and overcast (OVC) subsections by visual inspection of the GOES-10 infrared (IR) imagery. This allows us to compare the various boundary layer properties in the POC with those in the overcast region. This approach is similar, but not identical to Wood et al. [2011a] and Berner et al. [2011], who instead used radar reflectivity to distinguish the regions. Figure 2.2 shows subcloud flight legs from each of the five POC cases overlaid on GOES-10 IR images taken closest to the leg time. The transition region is identified to ensure that POC and overcast sections of the flight leg solely sampled the corresponding cloud types, with its width determined from the sharpness in the transition from overcast to broken clouds along the leg. In the following analysis, we compare the thermodynamic, macrophysical, and microphysical characteristics in the POC region and the overcast region.

2.3 Large scale context

2.3.1 Geographical and diurnal context

Four of the POC flights in this study were located at 80° W and just to the north and south of 20° S. The RF13 POC was located slightly to the east at 78° W (see Table 2.1 and Fig. 2.2).

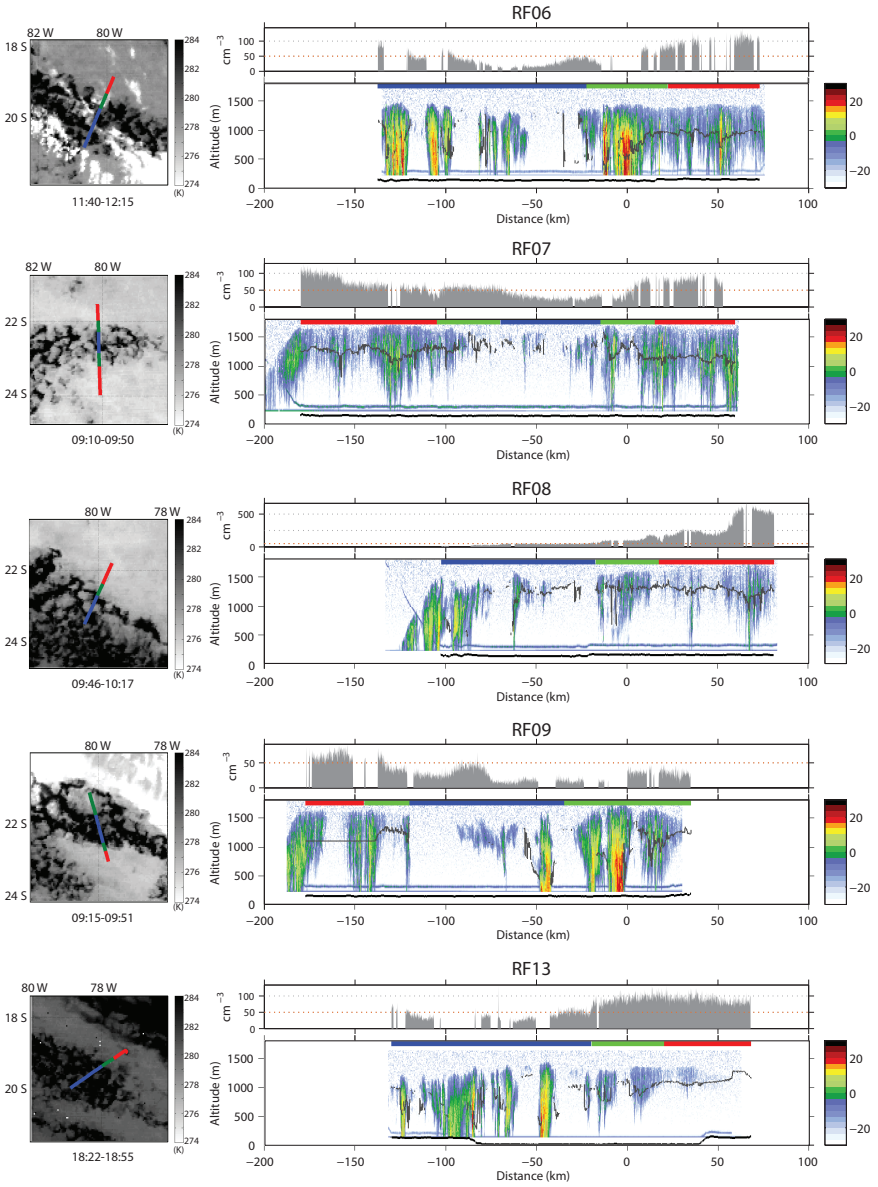

Figure 2.2: C-130 flight tracks overlaid on GOES-10 satellite imagery, in situ PCASP concentrations, and Wyoming Cloud Radar (WCR) reflectivity cross-sections from subcloud legs of the five POC cases analyzed in this study. For each POC case, the left panel shows the location of the flight legs in relation to the overall POC structure. The flight track is colored by distinction between POC (blue), overcast (red), and transition (green). The time of the flight leg (in UTC) is listed below each satellite image. The top panel for each case shows the aerosol concentration as measured by the PCASP ($0.1\,\mu\text{m} < D < 3\,\mu\text{m}$), where concentrations are filtered for drizzle events. The dotted line indicating $50\,\text{cm}^{-3}$ is highlighted in orange to remind the reader of the changing scale along the ordinate. The panel below the PCASP concentrations shows the WCR column reflectivities with the cloud base height from Wyoming Cloud Lidar traced in gray. All radar cross-sections and aerosol concentration time series are aligned along the middle of the north transition region.

The region around 20° S and 80° W has been characterized by a combination of aircraft and shipboard measurements made during VOCALS REx [Bretherton et al., 2010, Allen et al., 2011] and shipboard measurements from seven research cruises conducted from 2001 to 2008 [de Szoeke et al., 2012], for which the values are summarized in Tables 2.2–2.4. During the October and November months, the region was characterized by a median inversion height of $\sim 1240\,\mathrm{m}$ (25th–75th percentile range of 1220–1330 m; Bretherton et al., 2010), a diurnal mean cloud thickness of 250 m, corresponding to a mean liquid water path of $81\,\mathrm{g\,m^{-2}}$ [de Szoeke et al., 2012], and a mean cloud fraction of 90 % [de Szoeke et al., 2012]. Surface mixed layer accumulation-mode aerosol concentrations in the region average approximately $140\,\mathrm{cm^{-3}}$, but with large variations such that the 25th–75th percentile range is 70–220 $\mathrm{cm^{-3}}$ [Allen et al., 2011]. Because stratocumulus cloud cover and drizzle rates tend to maximize in the early morning hours [Wood et al., 2008, Leon et al., 2008, de Szoeke et al., 2012], and because a goal of VOCALS-REx was to observe the precipitation characteristics in POCs, four of the five POC-sampling research flights were conducted in the early morning hours (Table 2.1). Large differences in cloud properties between the one POC sampled during mid-day (RF13) and the four POCs sampled during early morning are apparent in the precipitation rate and in-cloud turbulence (Table 2.3 and Sect. 2.5.3).

Table 2.1: Time and location of POC flights in which POC-legs were flown. The local standard time is UTC – 5.3 h at 80° W. Location denotes the center of all flight legs flown for POC sampling.

Flight	Date	Time sampled - UTC	Location sampled
RF06	28 Oct 2008	08:24–13:23	18° S 80° W
RF07	31 Oct 2008	08:32–11:37	22.5° S 80° W
RF08	2 Nov 2008	09:07–12:24	22.5° S 80° W
RF09	4 Nov 2008	08:39–11:32	22° S 80° W
RF13	13 Nov 2008	16:03–20:11	19.5° S 78° W

2.3.2 Synoptic setting

The C-130 VOCALS sampling period of 15 October to 15 November 2008 was characterized as a quiescent period, in which little synoptic activity propagated from the mid-latitudes into the VOCALS region [Toniazzo et al., 2011]. During this quiescent period, however, POCs contributed substantially to cloud cover variability [Toniazzo et al., 2011]. Although no evidence has been found to show that the synoptic waves directly cause the POC features to form or that they help maintain POC features, because mid-latitude storms have the potential of affecting air masses advecting into VOCALS region [George and Wood, 2010], we cannot discount a possible influence from mid-latitude synoptic activity on the formation of POCs.

2.3.3 Free troposphere

Lower tropospheric stability (LTS) over the subtropical stratocumulus regions is positively correlated with low cloud cover [Klein and Hartmann, 1993, Leon et al., 2008]. In Table 2.2, we compare the LTS, calculated as the potential temperature difference between 700 hPa level and the surface, over the POCs and surrounding overcast region. We find no indication that the VOCALS POCs formed under remarkably high or low LTS conditions. Because the aircraft did not fly many profiles up to 700 hPa ($\sim$ 3100 m), the same 700 hPa potential temperatures are used to calculate LTS in POCs and overcast regions in Table 2.2. The surface potential temperatures are the mean potential temperature from the subcloud legs in each region. Because surface potential temperatures did not vary by much between separate POC cases (287–289 K), variations in LTS between cases are largely due to differences in the 700 hPa temperatures.

Stevens et al. [2005] observed a moister free troposphere (FT) above a northeast Pacific POC, which led to the hypothesis that POCs formed under regions with moister FT. Wood et al. [2008], however, found no evidence in the southeast Pacific that POCs formed preferentially in regions with a moister FT. Likewise, if we compare the water vapor mixing ratio (q_{v}) from the above-cloud flight legs flown over the POC and overcast region, then we find that q_{v} is not consistently higher above the VOCALS POCs (Table 2.2).

Table 2.2: Boundary layer and free tropospheric conditions in the POC and overcast (OVC) regions of the five observed POC cases. In addition to the five VOCALS cases examined in this study, the mean conditions at 80° W during the VOCALS field campaign and measurements reported in previous studies are listed for comparison. Mean and standard deviations are recorded as $\mu \pm \sigma$, whereas 25th–75th percentile ranges are shown as a range $x_{25\text{th}} - x_{75\text{th}}$. For conditions that vary with height level, the variables are preceded by SC (subcloud), CL (cloud), and AC (above cloud) to indicate the height level at which the measurements were taken. The inversion base height ($z_{\text{i, base}}$) is estimated from the profile legs as the height of the coldest temperature in the lower troposphere. The inversion height (z_{i}) is estimated from the profile legs as the height of the maximum of the 5 s-running-mean of $\mathrm{d}\theta/\mathrm{d}z$. The lower-tropospheric stability (LTS), defined as the potential temperature difference between 700 hPa and the surface, was calculated from taking the difference between the mean SC leg potential temperature and the mean potential temperatures calculated by the C-130 between 699 and 701 hPa and within ± 2.5° latitude and longitude of the POC location in Table 2.1.
[a] Inferred from Bretherton et al. [2010].
[b] Estimated from flight-mean C-130 data taken between 77.5 and 82.5° W across eleven research flights.
[c] VanZanten and Stevens [2005].
[d] Petters et al. [2006].
[e] Sharon et al. [2006].

Case	Region	$z_{\text{i, base}}$ (m)	z_{i} (m)	LTS (K)	AC q_{v} ($\mathrm{g\,kg^{-1}}$)	SST (°C)	$T_0 - \text{SST}$ (K)	SC U ($\mathrm{m\,s^{-1}}$)
RF06	POC	1262 ± 74	1411 ± 22	27	0.53 ± 0.21	17.3	−1.0	11.3 ± 0.9
	OVC	1338 ± 49	1393 ± 18	26	0.21 ± 0.03	17.7	−0.5	11.1 ± 0.9
RF07	POC	1587 ± 15	1658 ± 25	22	0.27 ± 0.03	17.3	−1.6	8.0 ± 1.4
	OVC	1613 ± 41	1654 ± 23	21	0.23 ± 0.07	17.7	−1.0	9.7 ± 1.1
RF08	POC	1599 ± 92	1642 ± 113	23	0.31 ± 0.05	17.5	−0.6	7.7 ± 1.1
	OVC	1656 ± 34	1672 ± 24	23	0.24 ± 0.06	17.6	−0.0	8.2 ± 0.7
RF09	POC	1420 ± 58	1543 ± 129	24	0.26 ± 0.12	17.5	−1.5	7.2 ± 1.1
	OVC	1521 ± 107	1539 ± 101	23	0.68 ± 0.10	17.8	−0.8	5.7 ± 0.7
RF13	POC	1343 ± 31	1365 ± 16	30	0.78 ± 0.12	17.9	−1.7	4.9 ± 1.2
	OVC	1298 ± 15	1307 ± 19	29	0.33 ± 0.09	17.5	−0.3	5.0 ± 1.2
Mean 20S 80W		1220–1330[a]		24.7 ± 2.4[b]		17.8 ± 0.4[a]		8.0 ± 1.9[b]
DYCOMS II								
VS05[c]	POC	794						
	OVC	794						
P06[d]	POC	794						
DECS								
S06[e]	POC	740–800						
	OVC	710 ± 75						

2.4 Boundary layer structure

2.4.1 Air–sea temperature difference

Air-sea temperature differences and wind speeds determine the temperature flux at the surface. Except for RF13, the SSTs are slightly lower in the POC than in the overcast region (Table 2.2). However, the apparent SST decrease in the POC is likely a sampling artifact. First, the approximately 1 K decrease in the subcloud temperature and $1\,\mathrm{g\,kg^{-1}}$ increase in the water vapor mixing ratio in the POC can lead to a low bias in the SST retrieved over the POC. Second, the decrease in cloud cover in the POC can decrease the amount of reflected infrared radiation, also leading to a low bias in SST retrieved over the POC [Smith et al., 1996]. Indeed, when the retrieved SST and downward infrared irradiance are compared within the POC segments of the flight legs, they somewhat correlate with each other. Despite this potential low bias of the POC SSTs, the estimated air–sea temperature difference inside the POC is larger than in the overcast region (Table 2.2). The cooler surface air temperatures in the POC, likely a result of cold pool formation, increase the air–sea temperature difference in the POC.

Relative changes in wind speed across the POC-overcast transition are small (Table 2.2). Therefore, any systematic changes in the surface sensible and latent heat fluxes are likely due to air–sea temperature and moisture differences in the POC. Across different POCs, a large range in surface-level horizontal wind speeds was measured (Table 2.2), which indicates that the maintenance of POCs does not require stronger or weaker winds.

2.4.2 Inversion height and structure

A critical parameter in marine boundary layer (MBL) evolution is the inversion height, which determines the cloud top height and affects the likelihood of boundary layer decoupling [Jones et al., 2011]. The inversion base height ($z_{\mathrm{i,\ base}}$) is estimated from the profile legs as the height of the lowest temperature in the lower troposphere [Jones et al., 2011, Wood et al., 2011a]. The $z_{\mathrm{i,\ base}}$ of the observed POCs and the surrounding clouds range from 1250 to 1650 m (Table 2.2), which is on the higher end of the range of $z_{\mathrm{i,\ base}}$ observed at 80° W during all the VOCALS-REx flights [Bretherton et al., 2010], but there is no in-

dication that POCs only form in deeper boundary layers. If we compare the POC with the surrounding overcast region, the inversion base height is 25 to 100 m lower in the POC than in the overcast region in RF06, RF07, RF08, and RF09, but 50 m higher for RF13, the one POC sampled during the daytime. Inadequate sampling precludes attributing this difference to the diurnal cycle. The $z_{\mathrm{i,\ base}}$ observed in the VOCALS POCs are substantially deeper than the 700–800 m inversion base heights of POCs observed previously over the northeast Pacific [see Table 2.2; VanZanten and Stevens, 2005, Sharon et al., 2006]. We conclude that POCs can be produced in boundary layers with a range of inversion heights.

The strength of the inversion determines how easily free tropospheric air can be entrained into the MBL. We compare the inversion structure over the POC and overcast region in Fig. 2.3. A mean profile for the overcast and POC region is constructed for each case from averaging the potential temperature from the profiles in 25 m height bins. To compare results from different POC cases, the mean inversion height (z_{i}) from each POC and overcast case found in Table 2.2 is subtracted from each profile. Rather than using $z_{\mathrm{i,\ base}}$ for this purpose (which would align the bottom of the gradient regions in the profiles), we define the z_{i} in each flight profile to correspond to the maximum of the 5 s-running-mean of $\mathrm{d}\theta/\mathrm{d}z$ and subtract the mean of those heights from each averaged profile. Table 2.2 gives this mean z_{i} for the POC and overcast (OVC) regions of each flight; for the four early-morning flights, the mean z_{i} is quite similar in the POC and OVC regions, even though $z_{\mathrm{i,\ base}}$ is lower in the POC. Figure 2.3 shows that the inversion is typically sharper in the OVC region than in the POC. This is expected given how radiative cooling from thick overcast clouds helps to sharpen the inversion. However, the inversion structure also differs from case to case. For example, the inversion in the overcast profile from RF09 is especially hard to identify. This is partly a result of averaging four different overcast profiles into one, but visual inspection shows that the inversions in individual profiles from the overcast region of RF09 are also less sharp than in other cases.

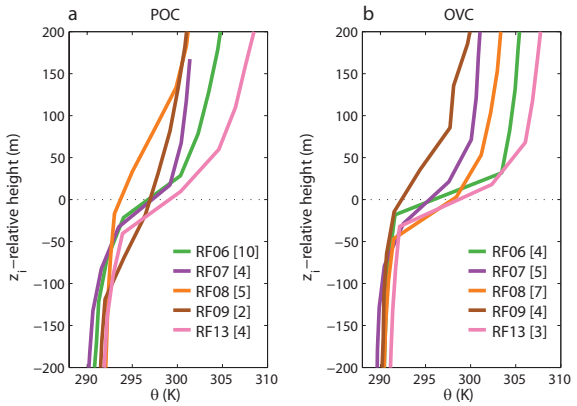

Figure 2.3: Potential temperature (θ) structure in POCs (left) and in overcast regions (right). Profiles are mean profiles based on data from profiles binned every 25 m. The number of individual profiles that are used to calculate the mean profiles is indicated in brackets next to each flight number. The mean height of maximum potential temperature increase is subtracted from each profile to examine the structures relative to the inversion height. Instead of the inversion base height, the mean height of the maximum vertical gradient in potential temperature is chosen for the reference height so that the temperature changes in each area are better aligned.

2.4.3 Decoupling

The degree to which the boundary layer is decoupled can be quantified by taking the difference (Δz) between the cloud base height and the lifting condensation level (LCL) from the subcloud flight legs [Jones et al., 2011]. Defined this way, the decoupling gives an indication of the relative timescales between boundary layer mixing and processes that act to stabilize the boundary layer. From Table 2.3, we see that for all cases, the POC has a significantly (150–350 m) lower LCL. In the nocturnal cases, the Δz is larger (indicating stronger decoupling) in the POC than the surrounding OVC region. In the one daytime flight (RF13), the OVC is more decoupled, consistent with observational and large eddy simulation studies that find that solar insolation strongly decouples the daytime overcast boundary layer [Turton and Nicholls, 1987, Bretherton et al., 2004, Caldwell and Bretherton, 2009]. Although Wood et al. [2011a] noted that the OVC region surrounding the RF06 POC was well-mixed ($\Delta z = 86$ m), we find that this feature is not shared across the other POC cases.

The stronger decoupling in POCs is likely a manifestation of strong drizzle evaporation in the subcloud layer that leads to the stabilization and decoupling of the lower boundary

layer. This traps surface fluxes in the lower levels of the boundary layer and leads to lower LCL. LES studies have shown that the increased stability from subcloud drizzle evaporation enhances the transition from closed to open cellular convection [Savic-Jovcic and Stevens, 2008] and that cold pools help to organize cumulus cloud convection [Wang et al., 2010, Berner et al., 2011]. It should however be noted that cold pools are not exclusive to POCs, but are also observed under non-POC forming overcast stratocumulus, and hence do not serve as a sufficient condition for POC formation [Terai and Wood, 2013].

2.4.4 Vertical wind variance ($\overline{w'^2}$)

Counteracting the stabilization of the boundary layer, the radiative cooling at cloud top drives turbulence and enhances the mixing between the cloud layer and underlying surface mixed layer. The strength of the turbulence can be quantified by the vertical velocity variance ($\overline{w'^2}$) measured within cloud-layer legs. The cloud-layer leg $\overline{w'^2}$ is calculated by taking the variance of the vertical velocity in each of the POC and overcast segments of the cloud-layer flight leg. Corroborating Wood et al. [2011a], we find that $\overline{w'^2}$ is lower in the POC across all cases (Table 2.3). The very low $\overline{w'^2}$ values in both POC and OVC regions in the RF13 case sampled during mid-day are probably due to absorption of solar radiation, which reduces the net cloud-layer radiative cooling that helps drive turbulence. It is illuminating to see local variations in $\overline{w'^2}$ over the course of a flight leg, which we calculate based on a 21 s ($\sim$2 km) moving window, which acts as a crude high-pass filter to isolate turbulent motions from mesoscale fluctuations. In Fig. 2.4, measurements from the cloud-level flight leg of the RF08 POC are shown to illustrate the observed changes in cloud, drizzle, and vertical wind speed across the POC-to-OVC transition. Figure 2.4b shows that $\overline{w'^2}$ is intermittent in the POC. Long stretches of very low $\overline{w'^2}$ are interrupted by short bursts of elevated $\overline{w'^2}$, which are associated with cumulus clouds. Although there are fluctuations in $\overline{w'^2}$ in the overcast region, the values are generally high. Cloud level $\overline{w'^2}$ also gives an indication of how much turbulence is available to entrain air from the FT. The much lower values of cloud-layer $\overline{w'^2}$ within POC regions compared to surrounding overcast regions with similar inversion temperature jumps suggest that the entrainment rates over

the POCs are much smaller than in the surrounding overcast regions, as found with LES [Berner et al., 2011].

2.5 Clouds and precipitation

2.5.1 Cloud macrophysics

A defining difference between the POC and overcast regions in a satellite image is the difference in cloud fraction. For cloud fraction estimates we use the upward-pointing Wyoming Cloud Lidar to detect overlying cloud during the C-130 subcloud flight legs. Cloud fraction in overcast regions are nearly 100 %, while on average, the POC regions have more variable cloud fraction between 56 % and 83 % (Table 2.3). The all-sky mean LWP can be higher or lower in the POC than in the OVC region, but the relative standard deviation of LWP (the ratio of the standard deviation of LWP to its mean, both given in Table 2.3), tends to be larger in the POC. This, together with enhanced decoupling, is an indicator of more cumulus-like convection within the POC [Jones et al., 2011].

These differences in cloud structures also manifest themselves in the precipitation rates. The mean precipitation rates are higher in the POCs than in the surrounding OVC regions (Table 2.3). POC radar reflectivities are also more broadly distributed. The column-maximum radar reflectivity ($Z_{\max}$) is plotted against the fraction of columns with reflectivity greater than that value in Fig. 2.5a. The broader distribution in the POC is evident from the shallower slope of the POC cumulative distribution, compared to the OVC. In particular, there is a much larger fractional coverage of strong drizzle > 10 dBZ for all POC cases. This contrast is consistent with statistics of the distribution of reflectivities within open and closed cell stratocumulus observed previously over the SEP with shipboard cloud radar [Comstock et al., 2007] and over the global oceans with CloudSat [Muhlbauer et al., 2014].

Terai and Wood [2013] found that precipitation at lower elevations is a better indicator of cold pool formation than the occurrence of precipitation at cloud base (where the column-maximum reflectivity is observed). Similarly, by examining the reflectivity at 250 m (Z_{250}) in Fig. 2.5b, instead of the column maximum ($Z_{\max}$), we find that reflectivities greater than 0 dBZ occur on average 10 % of the time in POCs compared to only ~ 1.5 % of the

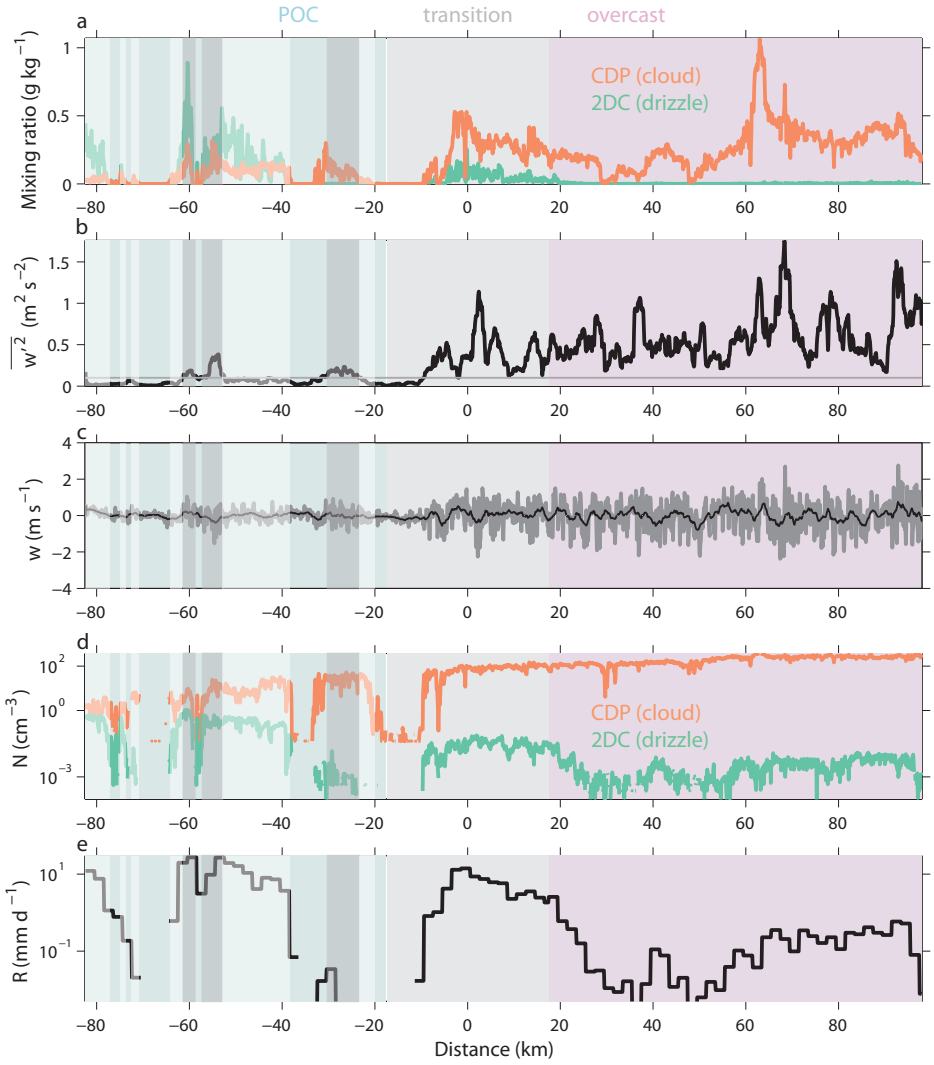

Figure 2.4: Cloud level measurements from cloud level flight leg showing **(a)** cloud (q_c – orange) and drizzle (q_D – green) water mixing ratio; **(b)** 21 s running vertical wind variance ($\overline{w'^2}$); **(c)** 1 Hz vertical wind speed (w – gray) and 21 s mean w (black); **(d)** cloud (orange – N_d) and drizzle (green – N_D) drop number concentration; and **(e)** precipitation rate R, based on 10 s averaged drizzle drop size distributions. In the POC segment of the flight leg, active clouds, defined as cloudy and drizzling data with $\overline{w'^2} \geq 0.1\,\mathrm{m^2\,s^{-2}}$, are shaded in dark gray. Quiescent clouds, defined as cloudy and drizzling data with $\overline{w'^2} < 0.1\,\mathrm{m^2\,s^{-2}}$, are shaded in white. The clear regions in the POC, where liquid water mixing ratios measured by the CDP or the PVM did not exceed $0.03\,\mathrm{g\,kg^{-1}}$, are left unshaded.

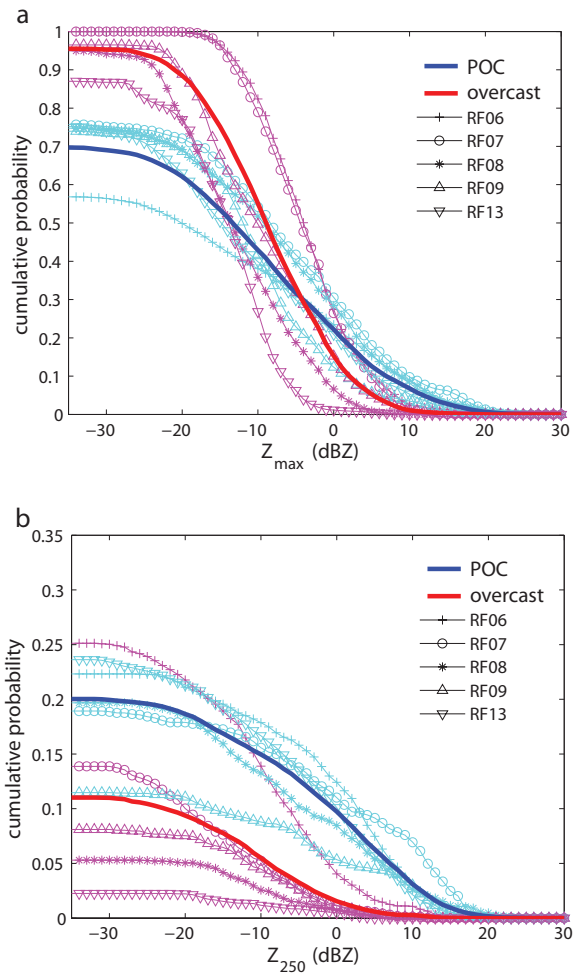

Figure 2.5: **(a)** The cumulative probability of column-maximum radar reflectivity $Z_{\max}$ greater than the abscissal value for overcast (red) and POC (blue) regions. The mean distribution are shown as bold lines, while individual flight legs are shown as thinner lines with markers. Radar reflectivities from all level flight legs are used to make the distribution. **(b)** Same as Fig. 5a, but for radar reflectivity at 250 m.

time in the OVC region. Among the different precipitation characteristics, this best differentiates the POC precipitation from the OVC precipitation. The reflectivities at 250 m are likely influenced by the amount of subcloud evaporation between the cloud base and 250 m. Therefore, the higher occurrence of > 0 dBZ precipitation at 250 m in the POC may reflect lower cloud base heights in the POCs rather than a difference in the drizzle drop size distributions.

The macrophysical signatures of the cloud and precipitation properties in POCs all point to more vigorous convection and correspondingly patchier and heavier precipitation within the POC than the surrounding overcast region.

2.5.2 Cloud microphysics

We now consider the cloud microphysical properties in the POCs. Consistent with previous POC observations [Petters et al., 2006, Sharon et al., 2006, VanZanten and Stevens, 2005, Wood et al., 2011a], all five of the POC cases examined here show cloud droplet number concentrations (N_d) decrease by more than a factor of eight from the OVC region (Table 2.4). Whereas the mean cloud-layer N_d inside the POCs has a range between 4 and 13 cm^{-3} across cases, the N_d in the surrounding OVC region range from 52 to 207 cm^{-3}, further showing that POCs can persist when surrounded by a wide range of microphysical environments. In the surrounding OVC, the case-to-case variations in N_d are highly correlated ($r = 0.98$) with the variations in subcloud PCASP aerosol concentrations (N_a). In the POCs, the relative changes in N_d is much more spatially variable than in OVC clouds, and N_d is at least a factor of three lower than the subcloud N_a. As we discuss below (Sect. 2.5.3), this is due to dramatically lower N_d in "quiescent" stratocumulus clouds than in the "active" cumulus clouds that bring up the subcloud-layer aerosol. Despite this, the mean subcloud N_a is correlated to N_d in the POCs ($r = 0.76$). We use a $\overline{w'^2}$ threshold of 0.1 $\mathrm{m}^2\,\mathrm{s}^{-2}$ as a means of distinguishing between the quiescent and active clouds inside the POC, except for the daytime case RF13, where the overall cloud-level vertical wind variance is low and hence where a threshold of 0.03 $\mathrm{m}^2\,\mathrm{s}^{-2}$ is used.

The horizontal-mean cloud water mixing ratio (q_c) drops drastically inside the POCs

(Table 2.4), due in part to a lower cloud fraction. In contrast, the horizontal-mean drizzle water mixing ratio (q_{D}) at least doubles inside the POCs, such that in all five POC cases the mass of water in the drizzle mode is larger than that in the cloud mode; remarkably, the $q_{\mathrm{D}}/q_{\mathrm{c}}$ ratio is at least twenty-fold larger in the five POCs than in the OVC regions. The increase in the estimated precipitation rate from the surrounding OVC region to the POC is not as large as that in q_{D}.

This apparent discrepancy is explained by the distinct size distribution of cloud and drizzle drops in the POC (Fig. 2.6). If we examine the cloud and drizzle drop size distributions measured by the CDP and 2DC in Fig. 2.6, we note a large increase in the drizzle drop concentrations in the POCs. Because the increase mainly occurs in the size range of smaller drops ($30\,\mu\mathrm{m} < 100\,\mu\mathrm{m}$), the larger concentrations in the POC do not contribute to large differences in the precipitation rate. The increase in the number of large cloud and small drizzle drops ($15\,\mu\mathrm{m} < 100\,\mu\mathrm{m}$) is curious and may be related to the very low N_{d} and different cloud types in POCs.

2.5.3 Active vs. quiescent clouds

A closer examination of the clouds found in POCs reveals two general types of clouds: thinner, stratiform, quiescent clouds and cumulus-like active clouds [Wood et al., 2011a]. We use a $\overline{w'^2}$ threshold of $0.1\,\mathrm{m^2\,s^{-2}}$ as a means of distinguishing between the quiescent and active clouds inside the POC, except for the daytime case RF13, where the overall cloud-level vertical wind variance is low and hence where a threshold of $0.03\,\mathrm{m^2\,s^{-2}}$ is used. Here we calculate the $\overline{w'^2}$ as the 21-s running mean $\overline{w'^2}$. In the RF08 example (Fig. 2.4), one can see lower N_{d}, lower vertical velocities, and consistently elevated drizzle drop number concentrations (N_{D}) in the quiescent clouds than in the active clouds. Table 2.5 quantifies and summarizes differences between the active and quiescent clouds in the POC regions, averaged for each of the five cases. Note that unlike Table 2.4, all of the listed variables are only averaged over cloudy portions of the flight leg. Although there are uncertainties in taking area estimates from one or two cloud-level flight legs, we find that across all POC cases, the quiescent clouds make up most of the observed clouds in the POCs. The cloud

droplet number concentration N_d is consistently lower within the quiescent clouds than in the active clouds, the latter having mean N_d on the order of $15\,cm^{-3}$. RF07 is an apparent exception, but active clouds were rarely sampled on this flight, with only 2 km of the flight leg sampling active clouds. The ratio between q_c and q_D differ between the two regions, much like the change in ratio between overcast and POC clouds; in active clouds, q_c and q_D are comparable, whereas in quiescent clouds, q_D is far greater. Nonetheless, it is important to note that the q_D in both active and quiescent clouds of the POC is far greater than in the overcast clouds. The high q_D is likely to increase the accretion and self-collection rates in POCs. Table 2.5 shows, however, that in each POC case higher q_D in quiescent clouds does not always translate to higher precipitation rates, which are estimated from the in situ 2DC-measured drizzle size distribution averaged over the appropriate cloud type. As in the POC-overcast comparison, this discrepancy exists because much of the drizzle mass difference resides at the smaller sizes, which have a smaller influence on precipitation rate.

2.6 Aerosol

2.6.1 Accumulation-mode aerosol

Some of the macrophysical difference between the overcast and POC cloud characteristics are attributable to differences in inversion structure and LCL height. Many of the microphysical differences, such as differences in N_d, are attributable to the low accumulation-mode aerosol concentrations (N_a) in POCs. The POC subcloud-layer N_a of $\sim 30\,cm^{-3}$ (Table 2.4), as measured by the PCASP, are much lower than the typical 25–75th percentile range of 70–$220\,cm^{-3}$ [Allen et al., 2011] in the 80° W region during the VOCALS-REx time period. N_a in the surrounding overcast regions range between 64 and $330\,cm^{-3}$ across the five cases, similar to the REx-mean distribution near 80° W, and are well-correlated with N_d (Table 2.4). The cases (e.g., RF08) with higher N_a in the overcast region are related to hook features associated with localized offshore aerosol transport in the free-troposphere and boundary layer, described by George et al. [2013]. The subcloud N_a in the POC is uncorrelated with N_a in the surrounding overcast and shows remarkable small variation (24–$40\,cm^{-3}$) across the five POC cases. If we extend the comparison to other previously

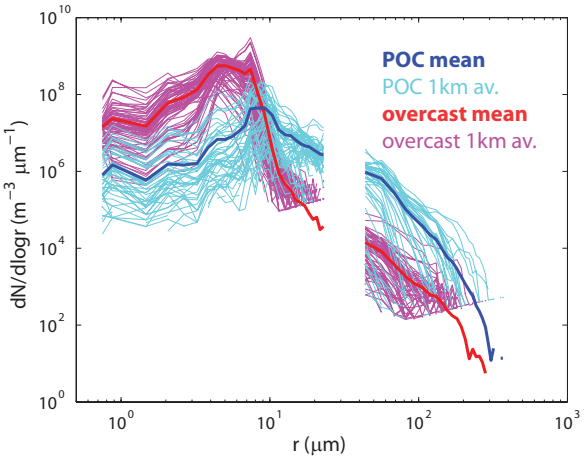

Figure 2.6: Droplet size distribution from the CDP and 2DC during a cloud-level flight leg from RF08. The cyan lines indicate distributions estimated from 1 km averages in the POC, while the heavier blue line indicates the mean of those distributions. The magenta lines indicate distributions estimated from 1 km averages in the overcast region, while the heavier red line indicates the mean of those distributions.

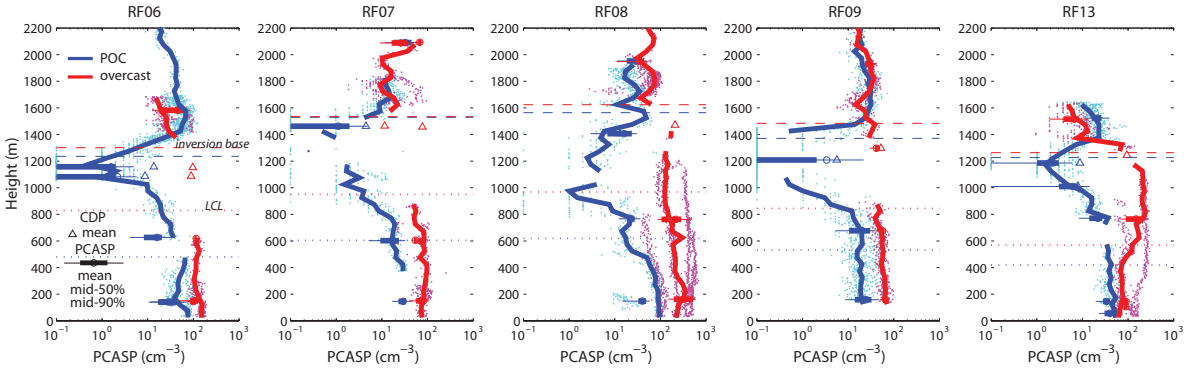

Figure 2.7: Profiles of PCASP aerosol concentration from the POC (blue) and overcast (red) region. Cyan (POC) and magenta (overcast) dots indicate individual data points from profiles flown in the two regions. Concentrations $< 0.1\,\mathrm{cm}^{-3}$ are set at $0.1\,\mathrm{cm}^{-3}$ to allow for easier plotting on the log-scale abscissa. Heavier profile line indicates the median taken from the profile data. PCASP data from level flight legs are also included in the form of whisker plots. For reference, cloud-mean cloud droplet number concentrations from the CDP are shown as open triangles, mean inversion base heights calculated from profile measurements are shown as dashed lines, and mean lifting condensation levels calculated from subcloud flight legs are shown as dotted lines.

observed POC cases [Sharon et al., 2006, Petters et al., 2006, Wood et al., 2008], the similarity in subcloud N_a still holds (Table 2.4). Spatially, across the overcast-to-POC transition, subcloud N_a gradually decreases over tens of kilometers across the transition (Fig. 2.2), whose gradients across the transition vary from case to case. Even within the POC, Fig. 2.2 and Table 2.4 show that subcloud N_a can spatially vary by more than 25 %.

Whereas we have mostly examined data collected during the level flight legs to examine horizontal gradients in N_a, we use both the profiles and level flight legs to examine the vertical distribution of N_a (Fig. 2.7). In the RF06 case, Wood et al. [2011a] noted a layer of ultraclean air in the POC region where mean PCASP aerosol concentrations are considerably lower than $10\,\mathrm{cm}^{-3}$. We find that an ultraclean layer exists in all of the other POC cases examined during VOCALS. The ultraclean layers typically extend from roughly the stratocumulus cloud base height to the inversion base, with a broad range of thicknesses (from 200 m for RF06 to 700 m for RF07). The concentrations in the ultraclean layer also vary from case to case, ranging from the very clean RF09 case, where a 400 m layer with concentrations $< 1\,\mathrm{cm}^{-3}$ was observed, to the more polluted RF08 case, where concentrations mostly hovered around $5\,\mathrm{cm}^{-3}$ and those concentrations $< 1\,\mathrm{cm}^{-3}$ were rarely observed. Concerning the structure of the ultraclean layer, with the exception of RF08, the vertical gradient in aerosol concentration is sharper at the inversion compared to the more gradual change from relatively well-mixed subcloud layer to the ultraclean layer.

2.6.2 Aitken-mode aerosol

Whereas N_a is much lower in the POC at all heights, the same is not true for concentrations of smaller aerosol particles. Past shipboard measurements [Kollias et al., 2004, Petters et al., 2006, Tomlinson et al., 2007, Wood et al., 2008] reported an increase in the number of Aitken-mode aerosols in the very clean regions of the POCs, suggesting that the low aerosol concentrations in the POC allow for the nucleation of Aitken-mode aerosols. Their growth to accumulation-mode sizes may potentially provide a source of cloud condensation nuclei (CCN) in the POC [Kazil et al., 2011]. The Aitken-mode aerosol concentration is estimated from our C-130 observations as the difference between total aerosol concentrations

for particles with diameter $> 10\,\mathrm{nm}$ (CN) and those from the PCASP ($> 100\,\mathrm{nm}$). From our observations of the five POC cases, no clear picture of enhanced or depleted Aitken-mode aerosols emerges. Subcloud Aitken-mode aerosol concentrations in the POC only increase for three of the five cases (RF06, RF08, and RF09; Table 2.4), and their concentrations do not correlate with subcloud N_a. We also find that except for the daytime RF13 flight, the concentration of Aitken-mode aerosols decreases in the ultraclean layer, where we expect the highest nucleation rates due to low aerosol surface concentrations. It must be noted that four of the POCs were sampled during the night, when photochemical production of nucleation mode precursor gases is absent. Whereas the processes that determine the sources and sinks of accumulation-mode aerosols appear to have a clear vertical structure, the Aitken-mode aerosols appear to be modulated by a variety of processes that are not as well constrained across different POC cases.

2.6.3 Accumulation-mode aerosol budget in POCs

Although we should entertain the possibility that the relatively small variation between cases in POC subcloud N_a is coincidental, it certainly warrants attention. The similarity across different POCs indicates that the source and sink balance of accumulation-mode aerosols somehow gives rise to relatively constant concentrations. Such a stable equilibrium at low aerosol concentrations is suggested by the modeling study of Baker and Charlson [1990]. The small spread between cases is surprising given that the observations are strongly suggestive of a surface source of aerosols and that mean surface wind speeds vary between 5 and $11\,\mathrm{m\,s^{-1}}$ between cases. Surface aerosol fluxes from sea-salt flux parameterizations are strong functions of wind speed [e.g., de Leeuw et al., 2011].

If we assume that the primary source of aerosols in the POC is indeed the ocean surface, then a steady-state CCN concentration in the POC subcloud layer (N_s) can be estimated with the equation:

$$N_\mathrm{s} = N_+ + \frac{F}{M_\mathrm{Cu}}, \tag{2.1}$$

where N_+ is the CCN concentration just above the subcloud layer, F is the surface source of CCN-sized aerosols, and M_Cu is the entrained mass flux into the subcloud layer from

above, that keeps the surface layer partially coupled to the cloud layer in the POC. This must equal the cumulus mass flux out of the subcloud layer. In other words, the surface flux of CCN is balanced by the mixing of CCN-depleted air into the top of the subcloud layer.

We may obtain estimates of N_+, F, and M_{Cu} to verify whether this balance equation applies to the observed POC cases. N_+ is estimated as the mean PCASP aerosol concentration from the below cloud flight legs. F is estimated using the sea salt flux parameterization from Clarke et al. [2006], integrated over the same size range as that sampled by the PCASP. The 10 m mean wind speed (u_{10}) that is needed for the calculation is estimated from the mean wind speed measured in the subcloud legs and assuming a log-wind profile with a surface roughness of 1.86×10^{-4} m [Wood et al., 2011a]. Because the parameterized aerosol flux has a dependence of $u_{10}^{3.41}$, an order of magnitude difference in fluxes exists between the low and high wind conditions (see Table 2.6).

The cumulus mass flux (M_{Cu}) can be estimated from examining the water balance at the top of the subcloud layer. If we assume that the upward moisture flux in the cumulus clouds is balanced by precipitation rates, then M_{Cu} can be estimated as

$$M_{\mathrm{Cu}} = \frac{R_{500}}{\Delta q}\rho, \tag{2.2}$$

where R_{500} is the precipitation rate at 500 m, Δq is the moisture difference between cloudy and clear parcels at the top of the subcloud layer, and ρ is the air density, which we assume to be $1\,\mathrm{kg\,m^{-3}}$. The precipitation rate at 500 m is chosen, because this is the approximate height of the LCL (Table 2.3), which typically coincides with the height of the top of the subcloud layer. The estimated cumulus mass fluxes, reported in Table 2.6, range between 1.0 and $2.8\,\mathrm{cm\,s^{-1}}$.

Except in RF09, the estimated F/M_{Cu} is much smaller than the observed $N_{\mathrm{s}} - N_+$, inconsistent with the balance (Eq. 3.1). There are several possible reasons for this discrepancy, in addition to the simplicity of the budget in Eq. 3.1. First, determining an appropriate N_+ is made difficult by the vertical gradient in N_{a} at the top of the subcloud layer, as evident in Fig. 2.7. Rather than decreasing abruptly at the top of the subcloud layer, N_{a} gradually decreases upward into the cloud layer. Second, we have neglected any other sources

of CCN-sized aerosols, such as the growth of Aitken-mode aerosols to accumulation-mode sized particles. Third, other budget terms such as losses from precipitation scavenging of aerosols in the subcloud layer could be significant. What we can say from the values in Table 2.6 is that F/M_{Cu} can easily vary by more than a factor of four, and their variations do not correlate with N_{s} or $N_{\mathrm{s}} - N_{+}$. We are therefore left without an explanation to why the subcloud N_{a} in POC varies so weakly across different POC cases.

2.7 Non-POC cases

Two cases of cloud breaks which may appear as contenders for POCs, but which are excluded from our definition of POCs, are examined here. The first case of cloud break-up sampled during RF02 (18 October) and shown in Fig. 2.8a was sampled to the south of a hook-like cloud feature of enhanced N_{d} from the transport and entrainment from the free troposphere of anthropogenic aerosols [George et al., 2013]. Despite the break in the cloud to the south of the hook feature, we do not identify this feature as a POC, because it lacks the microphysical change (a substantial increase in effective radius at its edges) that we associate with POCs. In situ observations show that instead of a decrease in accumulation-mode aerosols, there is a subsequent increase in subcloud N_{a} from ~ 200 to $\sim 300\,\mathrm{cm}^{-3}$ to the south. Likewise, the N_{d} increases from ~ 100 to $\sim 200\,\mathrm{cm}^{-3}$ (not shown). From the C-130 observation alone, however, we cannot determine the reason for the cloud break-up to the south. We do find that the inversion at approximately 1000 m around 83° W is anomalously low, and the decrease in cloud cell size to the south in the satellite visible imagery hints at a lowering of the inversion height to the south that might mean a lowering of cloud top heights to the south.

The second case (Fig. 2.8b) corresponds to western edge of the stratocumulus cloud deck observed during RF04 (23 October), where large drizzle rates were observed. High radar reflectivities ($> 10\,\mathrm{dBZ}$), representing heavy drizzle, cold pool formation, and an increase in cloud effective radius towards the edge of the cloud deck were observed in daytime satellite retrievals of this case, but no open cellular convection was observed beyond the edge of the overcast clouds, excluding this case from our definition of POCs. We also do not observe a decrease in N_{a} to the west of the break up, although a decrease of aerosols in the clear region

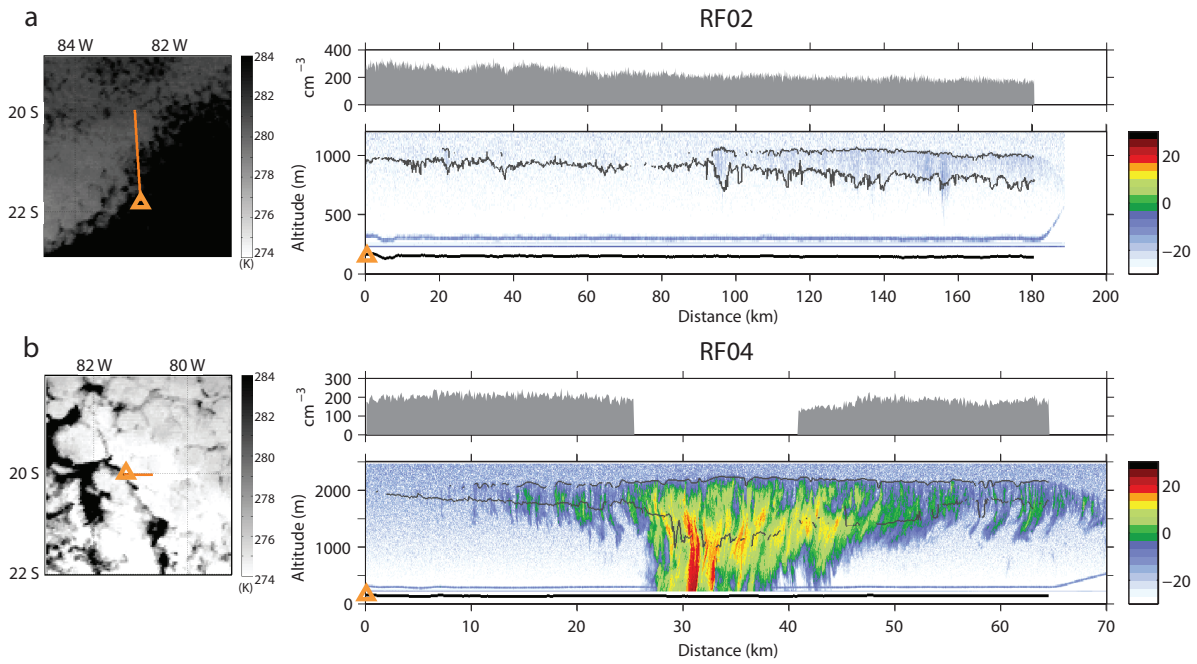

Figure 2.8: **(a)** C-130 subcloud flight track from RF02 (18 October 2008 16:50 UTC) is overlaid on GOES-10 infrared satellite imagery taken at the same time. As in Fig. 2.2, the top right panel shows the in situ PCASP aerosol concentrations at ~ 150 m. The bottom right panel shows the WCR reflectivity with the flight altitude indicated in bold black and the WCR/WCL-derived cloud top height and cloud base height indicated in gray. **(b)** Same as **(a)** but for a subcloud flight track from RF04 (23 October 2008 10:20 UTC).

is not part of the definition of POCs in this study. This suggests that higher precipitation rates at the edges of overcast clouds do not always indicate that the strong aerosol–cloud–precipitation interactions that we observe in POCs are the cause for the break-up in the clouds.

2.8 Discussion and conclusions

Five pockets of open cells (POCs) sampled during VOCALS-REx by the NSF/NCAR C-130 are comprehensively compared with their surrounding overcast regions. Free tropospheric water vapor and temperature, sea surface temperatures, inversion height, and near-surface winds were not found to differ appreciably in the POCs compared with the surrounding

overcast stratocumulus areas, and are not very different from the REx-mean conditions in the sampled regions. This latter fact indicates that POCs can be maintained under typical large-scale meteorological conditions found over the Southeast Pacific.

A consistent feature of POCs is the presence of heavy drizzle rates ($>10\,\mathrm{dBZ}$) and associated cold pools, which are largely absent in the surrounding overcast regions. All five of the observed POCs also contain both active, cumuliform and quiescent, stratiform clouds. Active clouds associated with cumulus-like convection, make up a smaller proportion of the cloud cover ($\mathrm{CF} < 25\,\%$) in the POC and have larger cloud droplet number concentrations (N_d) and larger cloud water mixing ratios (q_c). Although collision-coalescence rates are expected to be high in the active clouds, their comparatively high N_d ($20\,\mathrm{cm}^{-3}$) suggests that active clouds loft relatively aerosol-rich subcloud-layer air to the cloud layer. They detrain some of this aerosol into surrounding quiescent clouds, which cover more of the POCs and are characterized by very low N_d ($<10\,\mathrm{cm}^{-3}$) and high drizzle water mixing ratio (q_D). We cannot determine from these observations whether quiescent clouds are spatial extensions of active cells, as in the trailing stratiform region of larger mesoscale convective systems, are remnants of decaying active clouds, or are formed in situ. Snapshots of POC cloud fields from LES studies of Berner et al. [2011] and Kazil et al. [2011] suggest that quiescent clouds are spatial extensions of active cumulus clouds, but a closer examination of the time evolution of quiescent clouds will be necessary to resolve this issue.

The efficiency of the in-cloud coalescence scavenging in cleaning out accumulation-mode aerosols in POCs is most evident in the apparently omnipresent ultraclean layer observed in all five POCs. The presence of the ultraclean layer, combined with the low values of vertical velocity variance in the cloud layer within the POC and increased aerosol concentrations at lower altitudes, also strongly suggests that the surface source of accumulation-mode aerosols, and hence of cloud condensation nuclei, is more important than a free tropospheric source. In addition, we find that the spread of mean subcloud-layer accumulation-mode aerosol concentration (N_a) in the POCs is remarkably narrow, with a mean value ($\sim 30\,\mathrm{cm}^{-3}$) that is close to values found in previously studied cases from other locations and times [Sharon et al., 2006, Petters et al., 2006, Wood et al., 2008]. This mean value appears to be insensitive to N_a in the surrounding overcast region, suggesting that the factors controlling

the aerosol budget in the POC are independent of those in the surrounding overcast.

The factors that determine the N_a budget in the POC subcloud layer in the simple aerosol budget of Eq. (3.1) are quantified in Table 2.6. We find that our simple budget calculation does not shed light on explaining the narrow range of observed subcloud N_a in POCs. Instead it leaves us with a puzzle as to how the narrow range of N_a exists when the surface source of aerosols can differ by more than an order of magnitude. Because high resolution cloud resolving model studies with interactive aerosols also show similar accumulation-mode aerosol concentrations in the subcloud layer [Kazil et al., 2011, Berner et al., 2013], further modeling studies with variable surface source functions may help shed light on whether there is indeed a physical explanation for the similarity.

Finally it is important to state that while this study informs the mechanisms involved in POC maintenance, it does not inform the mechanisms by which POCs form. Previous modeling studies have looked at the transition from closed-cell to open cell convection mediated by cold pool formation [Wang et al., 2010], cloud-aerosol interactions [Kazil et al., 2011], or high liquid water path [Wang et al., 2010, Berner et al., 2013]. Observational studies have noted the possible role of gravity waves [Allen et al., 2013] or larger cloud droplet sizes [Wood et al., 2008] in POC formation, but widespread observational data is still lacking, largely because POCs preferentially form overnight [Wood et al., 2008]. A concerted effort to combine satellite retrievals and regional models will likely be necessary to pin down the key factors that contribute to POC formation; in a future paper, we will present a satellite-based study of the evolution of the five VOCALS-REx POC cases prior to the in situ aircraft observations.

Table 2.3: Similar to Table 2.2 but for boundary layer thermodynamic and cloud macrophysical properties. The lifting condensation levels (LCL) from the SC legs are reported here. Cloud fraction (CF) is based on the WCL cloud detection from the subcloud legs (1 Hz resolution). The decoupling parameter Δz is the mean height difference between the cloud base height and the LCL. $Z_{\max}R$ are segment means, and therefore include drizzling, as well as non-drizzling portions of the legs (1 Hz resolution).
[a] Estimated from flight-mean C-130 data taken between 77.5 and 82.5° W across eleven research flights.
[b] Inferred from de Szoeke et al. [2012].
[c] VanZanten and Stevens [2005].

Case	Region	Δz (m)	LCL (m)	CL $\overline{w'^2}$ ($m^2\,s^{-2}$)	CF (%)	SC LWP ($g\,m^{-2}$)	$Z_{\max}R$ ($mm\,d^{-1}$)
RF06	POC	343	480	0.17	56	251 ± 238	4.3
	OVC	89	829	0.69	100	173 ± 86	2.6
RF07	POC	781	605	0.05	75	27 ± 25	5.8
	OVC	255	950	0.52	100	166 ± 79	2.1
RF08	POC	545	619	0.09	80	110 ± 81	5.0
	OVC	299	968	0.67	100	131 ± 107	0.6
RF09	POC	429	532	0.08	73	107 ± 194	1.7
	OVC	–	845	0.37	–	137 ± 62	1.3
RF13	POC	372	419	0.03	83	215 ± 206	2.8
	OVC	517	569	0.12	100	59 ± 39	0.3
Mean 20° S 80° W		309 ± 147[a]	840 ± 60[b]	0.53 ± 0.14[a]	90 ± 4[b]	81 ± 10[b]	0.3–2.3[a]
DYCOMS II							
VS05[c]	POC			0.42 ± 0.03			
	OVC			0.32 ± 0.03			

Table 2.4: Similar to Table 2.2 but for cloud microphysical and aerosol properties. Aerosol concentrations are filtered for possible drizzle shattering events.
[a] Estimated from leg-mean C-130 data taken between 77.5 and 82.5° W across eleven research flights.
[b] Inferred from Allen et al. [2011].
[c] VanZanten and Stevens [2005].
[d] Petters et al. [2006].
[e] Sharon et al. [2006].
[f] Wood et al. [2008].

Case	Region	N_d (cm^{-3})	N_D (L^{-1})	CL q_c ($g\,kg^{-1}$)	CL q_D ($g\,kg^{-1}$)	SC N_a (cm^{-3})	CL N_a (cm^{-3})	SC CN (cm^{-3})	CL CN (cm^{-3})
RF06	POC	10 ± 13	275 ± 264	0.06	0.11	32 ± 18	1.7 ± 4.7	137	80
	OVC	94 ± 21	12 ± 7	0.31	0.03	103 ± 25	–	145	–
RF07	POC	4 ± 3	316 ± 128	0.03	0.08	29 ± 9	1.1 ± 1.8	140	80
	OVC	67 ± 29	44 ± 95	0.34	0.04	74 ± 20	–	195	–
RF08	POC	13 ± 12	251 ± 217	0.06	0.09	40 ± 13	22.0 ± 11.4	383	261
	OVC	208 ± 75	4 ± 4	0.27	0.00	324 ± 166	–	636	–
RF09	POC	6 ± 11	171 ± 143	0.02	0.05	24 ± 12	6.1 ± 12.2	307	214
	OVC	52 ± 20	25 ± 33	0.14	0.02	65 ± 9	–	207	–
RF13	POC	8 ± 8	270 ± 232	0.04	0.06	37 ± 11	4.2 ± 3.9	177	316
	OVC	94 ± 62	40 ± 22	0.26	0.02	90 ± 13	–	247	–
Mean									
20° S 80° W		133 ± 57[a]		0.09–0.29[a]	0.00–0.04[a]	70–220[b]	–	300–480[b]	–
DYCOMS II									
VS05[c]	POC	55 ± 16							
	OVC	70 ± 17							
P06[d]	POC	30 ± 15				40			
DECS									
S06[e]	POC	20				~ 10			
	OVC	40–60				~ 50			
W08[f]	POC					$\sim$ 20–50			
	OVC					$\sim$ 100–300			

Table 2.5: In situ measurements of cloud and drizzle properties of active and quiescent clouds observed across the five POC cases. A $\overline{w'^2}$ threshold of $0.1\,\mathrm{m^2\,s^{-2}}$ is used to categorize cloud measurements as either active or quiescent, except for the day-time flight RF13, where a threshold of $0.03\,\mathrm{m^2\,s^{-2}}$ is used. All active and quiescent values are averaged over in-cloud measurements, defined as measurements for which the combined liquid water mixing ratio from CDP and 2DC is greater than $0.03\,\mathrm{g\,kg^{-1}}$ or the PVM liquid water content is greater than $0.03\,\mathrm{g\,kg^{-1}}$.

Case	Cloud	Length (km)	Fraction (%)	$\overline{w'^2}$ ($\mathrm{m^2\,s^{-2}}$)	N_d ($\mathrm{cm^{-3}}$)	N_D ($\mathrm{L^{-1}}$)	q_c ($\mathrm{g\,kg^{-1}}$)	q_D ($\mathrm{g\,kg^{-1}}$)	R_insitu ($\mathrm{mm\,d^{-1}}$)
RF06	Active	32.5	14.6	0.70	21	280	0.29	0.22	24.0
	Quiescent	78.2	35.1	0.03	5	272	0.05	0.22	15.1
RF07	Active	2.0	3.3	0.17	5	233	0.07	0.09	3.5
	Quiescent	24.4	40.6	0.04	5	323	0.06	0.19	9.3
RF08	Active	14.6	22.5	0.18	19	213	0.12	0.15	11.5
	Quiescent	23.6	36.3	0.05	9	274	0.08	0.16	7.9
RF09	Active	5.2	4.3	0.55	26	49	0.15	0.02	2.1
	Quiescent	37.4	31.2	0.03	3	188	0.03	0.15	8.6
RF13	Active	32.0	15.1	0.06	15	214	0.16	0.11	5.9
	Quiescent	52.5	24.8	0.01	4	307	0.06	0.16	9.9

Table 2.6: Aerosol budget values. Values relevant to the aerosol budget of Eq. (3.1) are listed. Measured values include, PCASP-sized aerosols from subcloud (N_s) and below cloud (N_+) flight legs and Δq, the mean difference in water (vapor + cloud) mixing ratio between cloudy and clear conditions measured in below cloud legs. The surface aerosol flux (F) of PCASP-sized aerosols is estimated from the subcloud leg-mean wind speed (see Table 2.2) using the parameterization from Clarke et al. [2006]. POC-mean precipitation rate (R_{500}) at 500 m is estimated from the radar reflectivity at 500 m using the Z–R relationship proposed by Comstock et al. [2004] (R (mm d^{-1}) = 2.01 $Z^{0.77}$). The cumulus mass flux M_{Cu} is estimated using the relationship in Eq. (3.2).

Case	N_s (cm^{-3})	N_+ (cm^{-3})	$N_s - N_+$ (cm^{-3})	F ($\times 10^3$ m^2 s^{-2})	R_{500} (mm d^{-1})	Δq (g kg^{-1})	M_{Cu} (cm s^{-1})	F/M_{Cu} cm^{-3})
RF06	32	16	16	230	2.2	0.9	2.8	8.1
RF07	29	18	11	70	2.8	1.2	2.7	2.6
RF08	40	23	17	62	2.7	1.1	2.8	2.2
RF09	24	20	4	49	0.8	0.9	1.0	4.8
RF13	37	12	15	13	1.5	0.8	2.2	0.6

Chapter 3

MICROPHYSICAL PROCESSES IN POCKETS OF OPEN CELLS

The previous chapter addressed the measurable boundary layer and cloud differences between the POC and the surrounding overcast region. In POCs, the cloud drop number concentrations, drizzle drop concentrations, and droplet size distributions all suggest the strong influence of microphysical process rates in enhancing drizzle production and in cleaning out the cloud condensation nuclei (CCN) sized aerosol particles. This chapter concerns itself with inferring the microphysical process rates in POCs based on the measured drop size distributions in order to compare the process rates between the POC clouds and clouds found in the overcast region. The microphysical process rates concerned here are the rates at which the cloud and drizzle drops collide and coalesce with each other, namely autoconversion, accretion, and cloud droplet self-collection.

3.1 Introduction - estimating microphysical process rates in POCs

In the previous chapter we identified several common aspects that differentiate the POC boundary layer from the boundary layer of surrounding overcast regions. The most consistent difference between the POC and overcast boundary layer is the low accumulation-mode aerosol concentration in the POC ranging from 24 to 40 cm^{-3} in the subcloud layer, compared to 65 to 324 cm^{-3} in the overcast region. In the cloud-layer of the POC, accumulation mode aerosol concentrations can be as low as 1 cm^{-3}. This low concentration leads to much lower cloud droplet number concentrations (N_d) in the POC. Because reduced N_d has been associated with higher precipitation rates [e.g., VanZanten and Stevens, 2005, Comstock et al., 2004, Terai et al., 2012] and indeed precipitation rates are higher in POCs (Table 2.2), it logically follows that we expect higher drizzle-forming collision-coalescence rates in the POC. The occurrence of radar reflectivities >10 dBZ (roughly corresponding to precipitation rates >10 $\mathrm{mm\,d}^{-1}$) are also far more prevalent in the POC (Chapter 2). We also

find that the ratio of drizzle water mixing ratio (q_D) to cloud water mixing ratio (q_c) increases an order of magnitude in the POC. More specifically, droplet size distributions (as in Fig. 2.6) reveal a very distinct increase in the number of small ($< 100\,\mu$m) drizzle drops. Even within the POC, there are distinct differences in microphysics between active and quiescent clouds (Table 2.5). Except for the RF06 case, the number of drizzle drops (N_D) is particularly high in quiescent clouds, compared to active clouds. In this chapter, the collision-coalescence processes in the POC are examined using the droplet size distributions measured aboard the C-130 through application of the stochastic collection equations to understand why we observe these microphysical differences in the POC.

The collision-coalescence of cloud and drizzle droplets are normally categorized into four microphysical processes: autoconversion (collision of two cloud droplets to form a drizzle drop), accretion (collection of a cloud droplet by a drizzle drop), self-collection of cloud droplets (collision of two cloud droplets to form a bigger cloud droplet), and self- collection of drizzle drops. The self-collection of drizzle drops will not be included in the following analysis. To differentiate these processes, we need to define a threshold radius that differentiates cloud from drizzle drops. We choose a threshold of $25\,\mu$m, because it is the same threshold used by the bulk parameterization of Khairoutdinov and Kogan [2000], which is commonly used in many cloud resolving and larger scale models. By differentiating the collision-coalescence processes in the analysis, we are able to compare the rates calculated from the stochastic collection equation (SCE) with those calculated from bulk cloud microphysical parameterizations, in the same vein as Wood [2005] and Gettelman et al. [2013]. This will allow us to test whether bulk cloud microphysical relationships are adequate to capture the microphysical processes taking place inside the POC.

Modeling studies of POCs in large eddy simulations incorporating interactive aerosol microphysics have attempted to keep track of the sources and sinks of aerosols and water [Kazil et al., 2011, Berner et al., 2013]. For example, Berner et al. [2013] reported how autoconversion (A_u) and accretion (A_c), among other sources and sinks, contributed to the evolution of boundary layer CCN concentrations. In their simulation of POC-like clouds, accretion was found to be the dominant contributor to drizzle mass production, as well as the dominant sink for CCN-sized aerosols [Berner et al., 2013]. However, due to the computational costs

of using bin-microphysics, these studies employ bulk microphysical parameterizations to treat drizzle formation and impacts on aerosols. Because the bulk schemes are constructed to apply to clouds in typical drizzling conditions, and not specifically to POCs, where N_d is extremely low, it is unclear whether they capture process rates in POCs. We will address whether this is the case by comparing process rates calculated using bin microphysics with those calculated using bulk microphysics.

The data available to us constrain the questions and scope of our investigation. From the C-130 flights, we have measurements of cloud and drizzle drop size distributions (DSDs) from the CDP and 2DC probes, described in Chapter 2. Figure 2.6 provides one such example. These measurements were taken from the level flights legs, flown at cloud-level, typically 200 m below the cloud top. Although this provides us with continuous and consistent measurements of cloud measurements taken at one level, it does not provide us with much information about how DSDs vary with height in the POC and overcast clouds. Saw-tooth profile legs flown in the POC and overcast boundary layer may provide this information, but an examination of the saw-tooth legs shows that due to large horizontal variability in the POC clouds and the lack of cloud sampling, information on the vertical profile cannot be obtained in the POC.

Although there have already been a number of both observational and modeling studies on POCs, some questions remain unanswered and are addressed in this chapter. For example, what are the rates at which collision-coalescence removes CCN from the POC region? Are the removal rates substantially higher within the POC compared to neighboring overcast regions? What processes actually dominate precipitation formation and CCN removal? The current chapter is organized such that Section 3.2 provides the methods of how DSDs and the SCE solver by Bott [1998] are used to estimate microphysical process rates. Section 3.3 covers segment-mean process rates. Section 3.4 compares the process rates calculated using the Bott scheme with bulk parameterizations of Khairoutdinov and Kogan [2000]. Section 3.5 examines the sensitivity of the process rates to the length scales over which DSDs are calculated. Section 3.6 employs a simple parcel model to determine whether the DSDs of quiescent clouds can be obtained from the evolution of active cloud DSDs purely through collision and coalescence. Section 3.7 provides a summary and conclusions to the

chapter.

3.2 Droplet size distribution and stochastic collection equations

To estimate the rate at which cloud drops are converted into drizzle drops (both mass and number) and the rate at which aerosols are lost to collision-coalescence from autoconversion, accretion, and self-collection, we calculate the stochastic collection equations (SCEs) using a Linear Flux Method solver based on Bott [1998] as described by Wood [2005] and Wood and Hartmann [2006].

The SCE calculates how the DSDs evolve, based on the probability that two drops of different size collide and produce a larger drop. Applied to a size distribution, the equation takes the form

$$\frac{\partial n(x)}{\partial t} = \int_{x_0}^{x_1} n(x_c) K(x_c, x') n(x') dx' - \int_{x_0}^{\infty} n(x) K(x, x') n(x') dx', \tag{3.1}$$

where $n(x)$ is the concentration of drops with a mass of x, $x_c = x - x'$, $K(x_c, x')$ is the collection kernel describing the rate at which a drop of mass x_c is collected by a drop of mass x', x_0 is the mass of the smallest drop considered, and $x_1 = x/2$. The collection kernel $K(i, j)$ takes the form

$$K(i, j) = E(i, j)\pi(r_i + r_j)^2 \left| v_T(r_i) - v_T(r_j) \right|, \tag{3.2}$$

where $E(i, j)$ is the collision efficiency, summarized as the likelihood that two drops collide and coalesce given that their paths intersect, r_i and r_j are the radii of drops with mass i and j, and $v_T(r)$ is the terminal fall velocity of a drop with a radius of r. As noted by citetwood2005, the collision efficiencies are based on those reported by Hall [1980], Davis [1972], and Jonas [1972].

Unless otherwise noted, process rates are calculated on measured DSDs averaged over 10 seconds of data, which is equivalent to calculating process rate estimates every 1 km of horizontal flight. Because drop counts in the first three bins of the 2DC (radius < 43.75 μm) are not included due to quality control, a gap between the CDP and 2DC measurements exists. This poses a problem because the cutoff radius distinguishing cloud drops from

drizzle drops lies at 25 μm. Therefore, the concentration of droplets between the CDP and 2DC measurements are inferred by interpolating the concentrations between the CDP and 2DC concentrations. The interpolation scheme uses the last 3 CDP bin concentrations and first available 2DC bin to do a linear fit in log-log space. The linear fit provides interpolated concentrations in five bins equally spaced in log-space between the last CDP bin and first 2DC bin. Because the CDP has a smaller sampling volume than the 2DC, in calculating the linear regression, the CDP and 2DC measurements are weighted by the total number of counts that go into calculating the concentrations in each bin. When no counts are available for either the CDP or 2DC measurements to produce an interpolation, the concentrations in the gap are considered to be zero. An example of the interpolated DSDs based on the measured DSDs of RF08 is shown in Fig. 3.1.

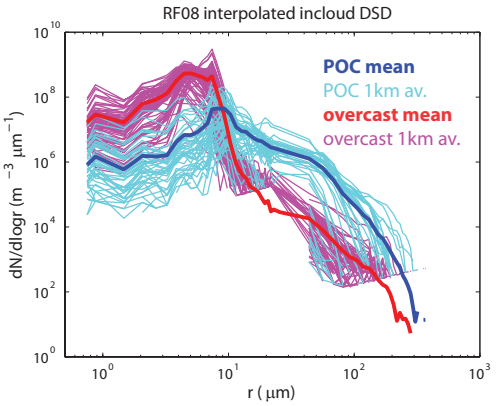

Figure 3.1: Droplet size distribution from RF08, where the gap between the the CDP and 2DC measurements are interpolated to provide a continuous size distribution. The cyan and blue lines indicate averages in the POC, whereas the magenta and red lines indicate averages from the overcast.

To estimate the process rates from the incloud flight legs, the following steps are taken. First, a 10-s-averaged DSD is calculated based on the CDP and 2DC measurements. Then, the measurement gap is interpolated to form a continuous DSD. Using the Bott SCE solver and using a threshold size of 25 μm, the mass and number autoconversion rate and accretion rate are calculated, in addition to the number loss rates due to self-collection of cloud drops.

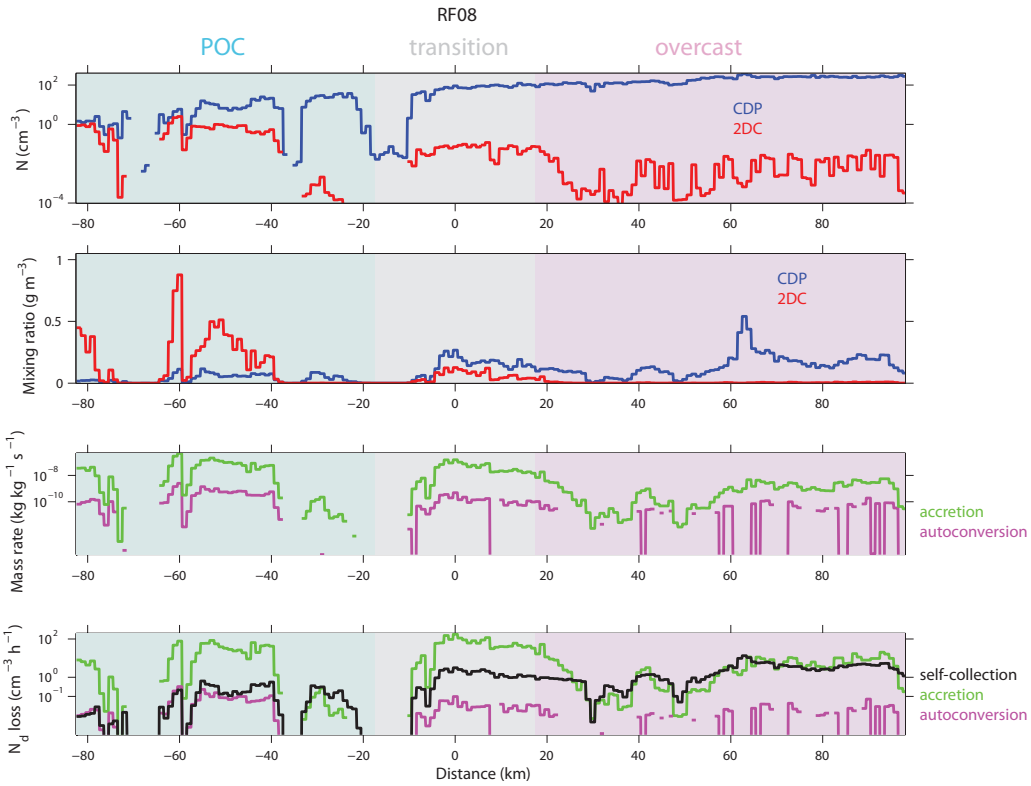

Figure 3.2: Cloud level measurements from RF08 of (a) cloud (blue) and drizzle (red) drop number concentrations; (b) cloud (blue) and drizzle(red) water mixing ratios; (c) accretion (green) and autoconversion (magenta) mass conversion rates; (d) cloud droplet loss rates due to self-collection (black), accretion (green), and autoconversion (magenta). Process rates are calculated based on 1 km averaged drop size distributions. The overcast, transition, and POC regions are indicated by the different colored backgrounds: red (overcast), gray (transition), and blue (POC).

3.3 POC-to-overcast transition and segment-mean process rates

Figure 3.2 plots the microphysical process rates calculated during the incloud flight leg of RF08 (same flight leg as that plotted in Fig. 2.4), along with the cloud and drizzle bulk microphysical properties as measured by the CDP and 2DC (cloud droplet number concentration N_d, drizzle drop number concentration N_D, cloud water mixing ratio q_c, and drizzle water mixing ratio q_D). If we examine the mass conversion rate from cloud to drizzle due to autoconversion (A_u) and accretion (A_c), we can see that A_c dominates the mass conversion rate in both the POC and overcast clouds. The difference between the two process rates increases considerably in the POC, where A_c appears to be two orders of magnitude higher than A_u. We also notice that there are considerable gaps in A_u in the overcast clouds where there are continuous cloud measurements. These gaps occur where q_D is nearly zero. As a result, there are scant drizzle counts for the DSD interpolation scheme to help fill in the concentrations of cloud drops around the 25 μm cutoff. This is one limitation of this method of trying to estimate process rates (especially A_u) from the measured DSD.

Shifting our focus to the N_d loss rates, we also incorporate the self-collection of cloud droplets in these calculations. When we incorporate self-collection into the comparison, we find that self-collection dominates the loss rates of cloud drops in the overcast clouds. Once substantial drizzle forms, such as in the POC clouds, accretion starts to dominate cloud droplet loss rates. From this flight transect alone, it is not clear though that cloud droplet loss rates are substantially higher in the POC. Subsequent sections will address whether cloud drop loss rates are indeed higher in POCs.

We continue the analysis by examining the segment-mean process rates from inside and outside the POCs from the five POC cases (RF06, RF07, RF08, RF09, and RF13). The autoconversion and accretion rates can be quantified in two ways, by tracking the mass budget of water or by tracking the number budget of the cloud and drizzle drops. Whether we examine the mass or the number budgets depends on the role of drizzle that we are interested in learning. If we are more interested in the rate of production of rain, then the mass budget is important. If we are more interested in the loss rate of aerosols through

collision-coalescence, then the cloud droplet number budget is important.

We first examine the segment-mean mass conversion rates in Fig. 3.3a, where the mass-conversion rates of accretion (A_c) are plotted against those of autoconversion (A_u). The open circles indicate segment-mean rates found in the overcast section, while the filled circles indicate segment-means from the POC section. Circles are colored by the POC case. A_u in the overcast region range from 10^{-11} to $1.5 \times 10^{-10}\,\mathrm{kg\,m^{-3}\,s^{-1}}$, while ranging from 5×10^{-11} to $10^{-9}\,\mathrm{kg\,m^{-3}\,s^{-1}}$ in the POC. Although the conversion rates overlap in the two areas, A_u is higher in the POC than in the neighboring overcast in every case. The same can mostly be said of A_c, except for RF09, where the A_c in the overcast region are higher than in the POC. A_c across cases and regions are also about two orders of magnitude higher than A_u. This indicates that the precipitation from clouds in and around POCs are produced primarily by accretion. Height dependence of A_u and A_c exist [Wood, 2005], but given the height dependence estimates that we present below, it is unlikely that A_u dominates production of rain in these clouds.

We now examine the number conversion rate in Fig. 3.3b and 3.3c, where the segment-mean number-conversion rates of accretion are plotted against those of self-collection (3.3b) and autoconversion (3.3c). Unlike Fig. 3.3a, the number-conversion rates are plotted on a linear scale. It is important to note that whereas accretion, autoconversion, and self-collection all lead to the loss of cloud droplets, only autoconversion increases N_D. As in the previous plot, we find that loss rates due to accretion dominate those of autoconversion (Fig. 3.3c) as well as self-collection, regardless of region (POC vs. OVC) or case. Accretion loss rates range in the order of 10 $\mathrm{cm^{-3}\ h^{-1}}$, while self-collection loss rates range are of order the 1 $\mathrm{cm^{-3}\ h^{-1}}$, and autoconversion loss rates of order 0.1 $\mathrm{cm^{-3}\ h^{-1}}$. It is important to note that these values are in-cloud loss rates, based on the measurements at one level and are not representative of boundary layer-mean loss rates. Whereas the mass conversion rates were generally higher in the POC than in the overcast region, the number loss rates are not consistently higher in the POCs. In RF09, RF13, and one of the legs from RF06, the loss rates in the overcast region are higher than in the POC. Contrary to what is expected from the simple explanation that aerosol concentrations are lower in the POC due to higher loss rates, a consistent picture of higher loss rates in the POC does not emerge from this

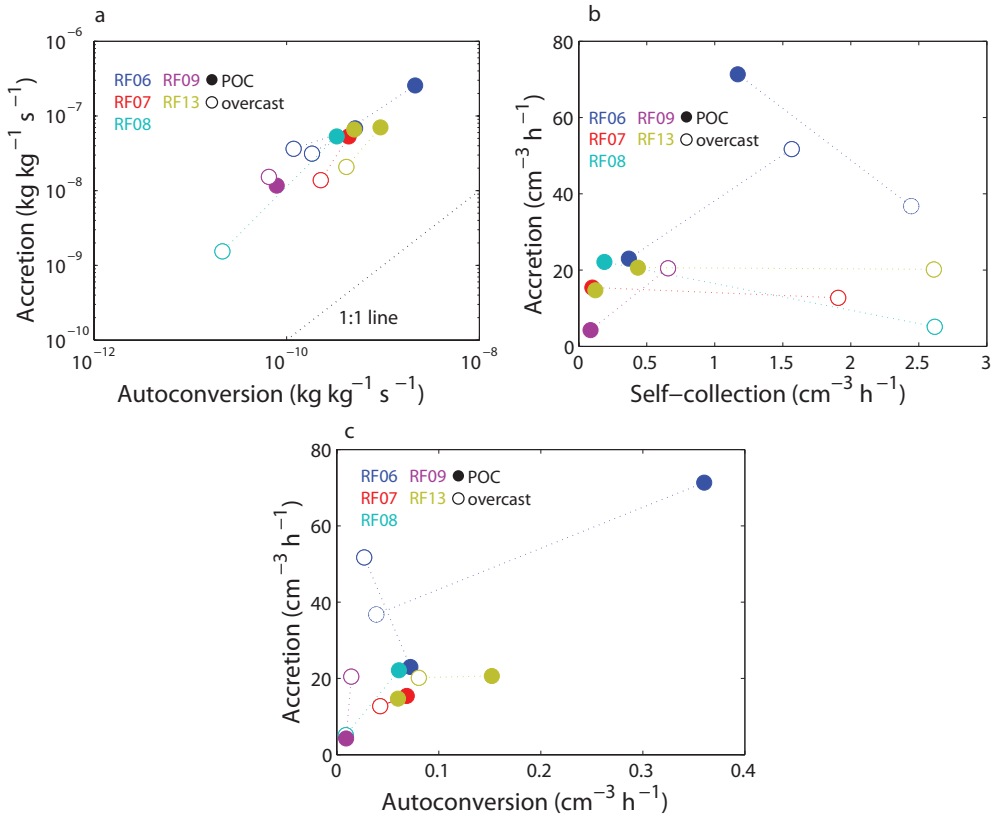

Figure 3.3: Estimated segment-mean rates of (a) mass conversion of cloud into drizzle water due to accretion and autoconversion, of (b) cloud number losses due to accretion and self-collection, and of (c) cloud number losses due to accretion and autoconversion. Open circles indicate segment means from the overcast section, while filled circles indicates means from the POC section of the in-cloud flight legs. Circles are colored by the POC case.

comparison. Part of this may be due to lack of cloud sampling. However, this can largely be understood by distinguishing between the conditions necessary to form POCs and those necessary to maintain POCs. All of POC cases here were sampled by the C-130 after the POC features had formed, hence we are examining to process rates that maintain POCs. Once the aerosol concentrations are reduced during the initial formation of POCs, the loss rates in the POC do not need to be higher than in the overcast region to maintain the low aerosol concentrations.

From this comparison, it is also unclear why N_D is much higher in the POC than in the overcast (see Table 2.4). From Fig. 3.3c, we not only can estimate the cloud drop loss rates, but can also estimate the production rate of drizzle drops. Given that the number concentration of drizzle drops is at least twenty times higher in the POC than in the overcast, we would have expected higher number conversion rates in the POC. It is possible that there is a different height dependence of conversion rates in the POC and overcast regions, but there are insufficient cloud profile transects exist to address this possibility. Therefore, we are left with a puzzle from the in-cloud flight leg observations of droplet size distributions.

In Fig. 3.3c, we found the cloud droplet number loss rates are not consistently higher within the POC despite larger drizzle water mixing ratios within the POC. The loss rates in the POC may sometimes be lower than in the overcast region by there being fewer cloud drops in the POC. Therefore, although loss rates may be lower in some of the POCs, the timescales over which cloud droplets are all collected in the POC would always be lower due to low N_d. By combining the number loss rates in Fig. 3.3b and 3.3c we estimate the cloud drop loss rate in POCs and in the overcast region by quantifying $\dot{N}_d/N_d$ against the *insitu*-derived precipitation rate from each segment (Fig. 3.4). Color and filled conventions of the data follow previous two figures.

As expected, the rate of complete removal of the cloud drops is consistently higher in the POC. Based on these observations, the time scale of complete removal in the POC is on the order of fifteen minutes to an hour. In contrast, the time scale in the overcast region is 2+ hours. We can compare our results with a CCN-loss rate parameterization from Wood and Hartmann [2006], based on the same methods used in this analysis, but with a different set of aircraft data. We notice that the parameterization does well in predicting the removal

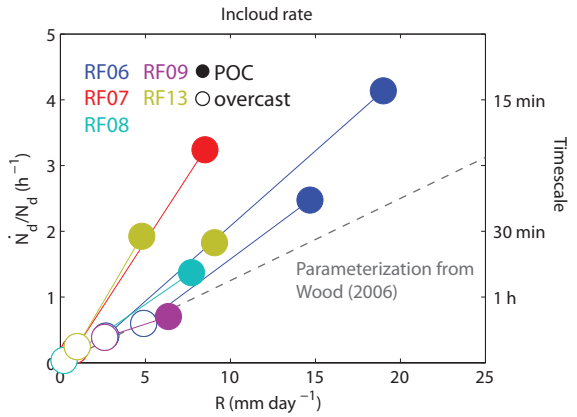

Figure 3.4: Estimated segment-mean rate of complete removal quantified as $\dot{N}_d/N_d$ plotted against the segment-mean precipitation rate. Color and filled conventions of the circles follow previous figure.

rates in the overcast clouds. However, we find that the removal rates in the POCs lie substantially above the line, indicating that the clean-out rate in the POC is quicker than that inferred from the precipitation rate based parameterization of Wood and Hartmann [2006]. This discrepancy is likely due to the choice of the coefficient for the mean collection efficiency (E_0) in the parameterization of Wood and Hartmann [2006]. Although further work is necessary to verify this, given the wide distribution of POC DSD, E_0 is likely higher in the POC compared to that of typical drizzling stratocumulus. This is likely due to the shift of the peak of cloud droplet concentrations to larger radii, where the collision efficiency with the collector drops is higher. To test this possibility, a closer inspection of which drop size ranges contribute to the total collision-coalescence loss rates will be necessary.

3.4 Comparison with bulk microphysics parameterizations

The results above are computed using the measured DSDs. The computational costs of running a bin microphysics scheme in large eddy simulation are high, and therefore, many studies of POCs using such models have employed bulk microphysics schemes to represent drizzle formation [e.g., Berner et al., 2011, Kazil et al., 2011, Berner et al., 2013]. Here, we assess how well the process rates from the Khairoutdinov and Kogan [2000] (KK00,

hereafter) bulk microphysics scheme compare with the process rates that we estimate from DSDs.

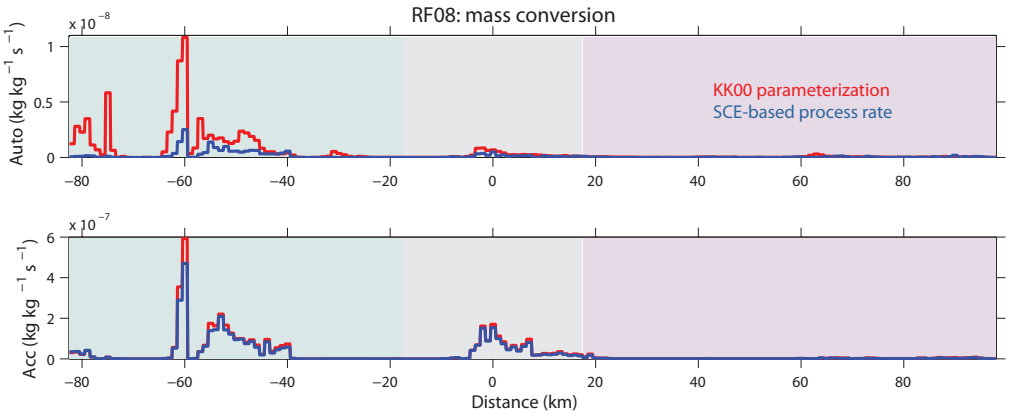

Figure 3.5: Cloud level estimates from RF08 of (a) autoconversion rates based on the Bott SCE-solver (blue) and the KK00 bulk parameterization (red); (b) accretion rates based on the Bott SCE-solver (blue) and the KK00 bulk parameterization (red). Process rates are calculated based on 1 km averaged drop size distributions and their bulk properties.

Figure 3.5a and 3.5b show A_u (Fig. 3.5a) and A_c from RF08 (Fig. 3.5b). Process rates calculated using the bulk KK00 formula are shown in red, while those calculated using the droplet size distribution are in blue. Apart from a few instances, especially for A_u inside the POC, the process rates agree quite well. The very good agreement in the A_c is especially reassuring, given that A_c dominates both drizzle formation and cloud drop loss rates in the POC.

Fig. 3.6a and b show how well the bin and bulk microphysical process rates agree in terms of segment means across the five POC cases. Whereas Ac between the SCE and KK00 parameterization agree very well, the KK00 Au are biased higher by approximately three to four times the SCE values. Surprisingly, this positive bias of KK00 accretion values is not unique to the POCs, but also appears in the overcast clouds. A similar comparison was done by Wood [2005], where A_c and A_u from the SCE were compared to those calculated using the KK00 parameterization. For the set of data examined by Wood [2005], the KK00 tended to overestimate A_u at rates $< 10^{-9}\,\mathrm{kg\,kg^{-1}\,s^{-1}}$. Our results are fairly consistent with

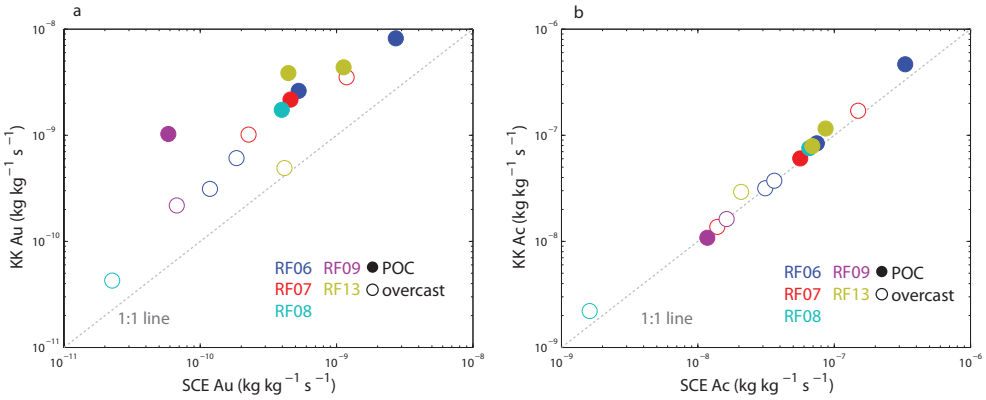

Figure 3.6: Comparison of SCE-based and KK00-based segment-mean rates (a) autoconversion and (b) accretion. Color and filled conventions of the circles follow previous two figures.

those of Wood [2005], although the bias appears to exist across all rates. This is curious given that the range of Au estimated from the aircraft observation lies within the range over which the KK00 parameterization was developed. A comparison with process rates from other VOCALS incloud legs will be necessary to verify whether the overcast and POC drop size distributions are unique to result in a large overestimation by the KK00 A_u.

3.5 Scale dependence

Because autoconversion and accretion are not linear functions of q_c, q_D, and N_d, we might expect that the length scales over which DSDs are averaged over to calculate the process rate to affect the segment-mean process rates that we calculate. When using the DSDs to calculate the process rates, we are constrained by two factors. First, if we take too large of a length to produce the DSDs, then we may miss cloud-scale variations in q_c, q_D, and N_d, leading to an underestimate of process rates [Larson et al., 2001]. On the other hand, if we choose too short of a segment to average over, we might not accumulate enough measurements of cloud drops, especially those with low concentrations, to create an accurate size distribution over which autoconversion and accretion rates may be calculated.

In the analyses of previous sections, DSDs were calculated every 10 seconds (1 km). We

test the effect of length scale on the segment-mean A_u and A_c that we calculate by comparing segment-mean A_u and A_c when we calculate the process rates over 5 seconds and 40 seconds. The comparison is shown in Fig. 3.7 (A_u in Fig. 3.7a and A_c in Fig. 3.7b). We notice that both A_u and A_c are rather insensitive to the choice of averaging length for the DSD (from 5-40 s). For A_u, averaging the DSDs over 40 s leads to slightly lower rates, compared to when they are averaged over 5 seconds. This lends confidence that the process rates that we previously using 10 s-averaged DSDs are not heavily dependent on the choice of averaging length. On the other hand, given the scales over which q_c and q_D vary in the flight leg (see Fig. 3.2) if we tried to average the DSDs over 20 km or longer, we may start to see larger differences.

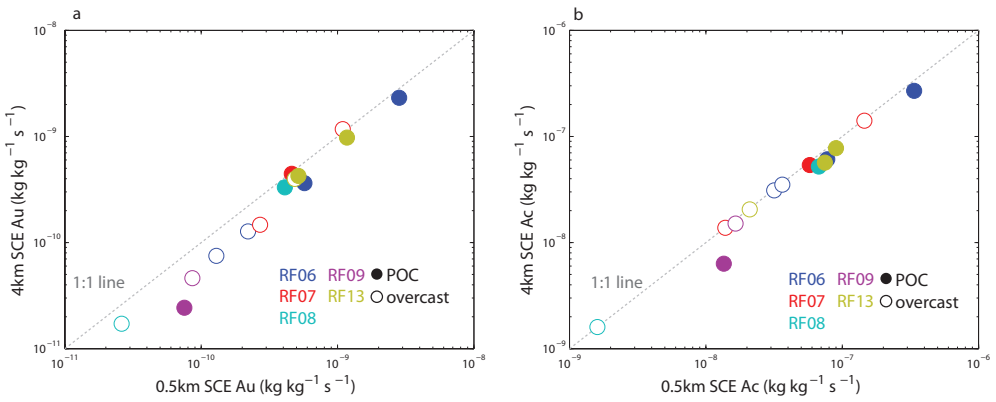

Figure 3.7: Comparison of SCE-based segment-mean rates of (a) autoconversion and (b) accretion for averaging lengths of 0.5 and 4 km. Color and filled conventions of the circles follow previous two figures.

3.6 Limitations to method

There are a number of limitations to our method in trying to compare microphysical process rates in POC and overcast clouds. One issue that we are unable to tackle is the issue of spatial heterogeneity of the clouds that asks to what extent our analysis is able to capture the true distribution of cloud microphysical process rates when we miss many of the clouds in the POC segments of the flight. One issue that we attempt to address here is one of the

vertical distribution of hydrometeors, and hence, of process rates. As mentioned earlier, sampling limitations inhibit us from examining the vertical distribution in POC clouds. However, we can examine the vertical structure of accretion and autoconversion rates in stratocumulus more generally by expanding the data to all VOCALS cloud profiles flown by the C-130.

The vertical cloud profiles from the C-130 aircraft data are combined and the A_u and A_c, based on 10-second averaged DSDs are calculated, much like the in-cloud level flight legs. After the cloud top and cloud base are determined using a 5-s-smoothed liquid water content cutoff of $0.01\,\mathrm{g\,m^{-3}}$ to define cloud, the data are normalized such that the cloud bottom is assigned a height of zero and the cloud top unity. Then the A_u and A_c values are binned into twenty height bins. Finally, the process rates are normalized by the profile-mean process rate. This allows us to examine how the height in cloud at which the aircraft samples affects the inferred process rates. Fig. 3.8 and 3.9 show the vertical structure of the mass conversion and number conversion rates from autoconversion and accretion, based on the VOCALS aircraft data. Each blue line is an individual profile, while the bold black line indicates the median and thin black lines indicate the 25th and 75th percentile values. As was found by Wood [2005], process rates increase with height. Accretion shows a wider distribution in what the vertical structure can look like from cloud to cloud, while autoconversion has a tighter distribution.

In the context of our observations of POC and overcast clouds, the aircraft generally flew roughly 200 m below the cloud top, which corresponds to about 1/2 to 2/3 height within the cloud. According to Fig. 3.8 and 3.9, this corresponds to roughly the profile *mean* accretion and autoconversion rate. It also corresponds to roughly 2/3 of the *maximum* accretion and half of the *maximum* autoconversion rate. Although we may expect POC clouds to have a different structure, this analysis shows that the process rates obtained from the level flight legs are not too different from the profile mean process rates.

3.7 Active vs. quiescent clouds

In this section, we attempt to reconcile the microphysical properties of the quiescent clouds of POCs by employing a parcel model. As the name implies, quiescent clouds are defined as

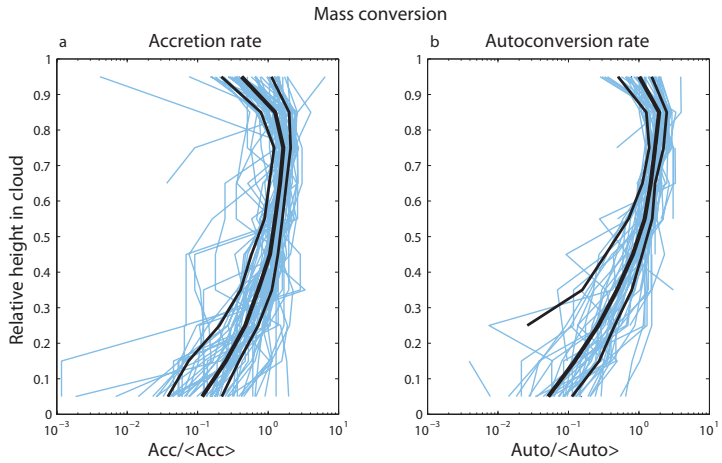

Figure 3.8: Relative changes in (a) accretion and (b) autoconversion mass conversion rates with height within clouds observed during VOCALS. The process rates are normalized by the profile-mean process rate. Each cyan line is an individual profile, while the bold black line indicates the median and thin black lines indicate the 25th and 75th percentile values.

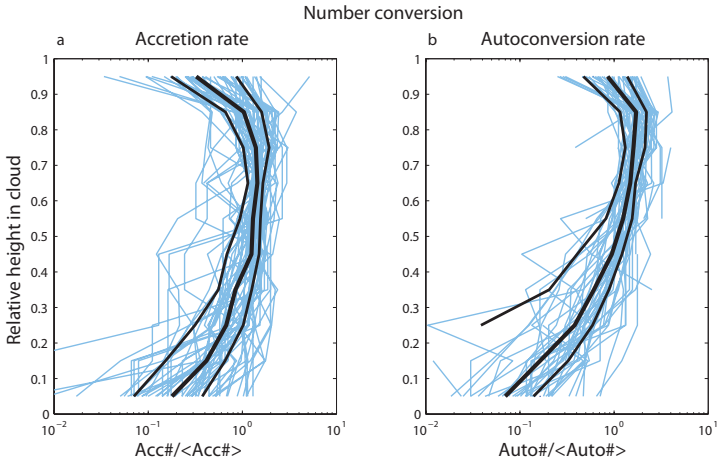

Figure 3.9: As in Fig. 3.8, but for the number conversion rate.

clouds in the POC that have very low turbulence [Wood et al. 2011]. In Section 2.5.3, we define quiescent clouds as cloudy areas in the POCs where the vertical wind variance is less than $0.1\,\mathrm{m}^2\,\mathrm{s}^{-2}$. Apart from covering a larger fraction of the POC area, quiescent clouds are characterized by lower N_d, lower q_c, and relatively high q_D compared to active clouds. The formation of quiescent clouds is still not well understood, but they are hypothesized to either be spatial extensions of active clouds or remnants of once active clouds [Wood et al., 2011a]. Another possibility is that quiescent clouds form *in situ* independent of active clouds.

Here, we will test the general hypothesis that quiescent clouds are spatial extensions of hydrometeors detrained from active clouds, as shown in the schematic of Fig. 3.10. We run various experiments with a parcel model with bin-microphysics to determine whether we can obtain the high concentration of small drizzle drops that are frequently observed in quiescent clouds, purely from collision-coalescence. In subsequent experiments, we will allow condensation to shift the droplet size distribution, because general ascent or cloud top cooling can lead to condensational growth of existing drops. Aerosol activation is not considered here but is not expected to be important for the drop size range being considered.

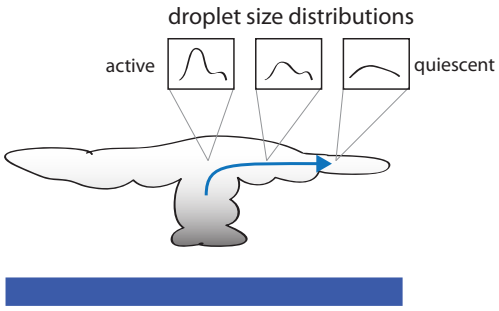

Figure 3.10: Schematic of quiescent cloud as a spatial extension of an active cloud and how drop size distributions evolve with air flow.

The observed DSD in active cells are used to initialize the model, and we examine how the DSDs evolve in a parcel model. The questions we hope to answer are, can we use a simple parcel model to see how the DSDs evolve over time? Do they approach the DSDs seen in quiescent clouds?

3.7.1 Experiment: No sedimentation

In these first experiments, we allow all the drops to stay within the box while the bin microphysics scheme of Bott [1998] allows bigger drops to collect smaller drops. The simulation is run out for 10 min. These experiments do not allow even the largest drizzle drops to sediment. Therefore, we are just examining the effect of collision-coalescence if the drops were not to sediment.

The results from a simulation initialized with the mean DSD of the active clouds measured during one of the RF06 cloud-level legs are plotted in Fig. 3.11. Following the evolution of N_d, q_c, and q_D, the bin model captures the general decrease in N_d and q_c and the increase in q_D that is observed when comparing active and quiescent clouds. Because the q_c+q_D is conserved in these simulations, it is not really surprising that we see an increase in q_D accompanying a decrease in q_c.

What the simulation fails to capture is the increase in N_D that we observed from the 2DC measurements of quiescent clouds. Across the 25-50 μm size, the number concentrations decrease throughout the simulation. Because there is drop sedimentation, the loss is either due to collection by larger droplets or self-collection of similar sized particles. Looking at the droplet mass distribution (Fig. 3.11b), it appears that both mechanisms are at work. In terms of autoconversion, accretion, and drizzle-drop self-collection, the self-collection loss rate of smaller sized drizzle drops outweighs the number increase from autoconversion.

As one would expect, very large droplets stay in the box and grow in this simulation, which seems unlikely unless very strong updrafts exist. The number of drops $>100\,\mu$m consistently increase throughout the simulation. This means that droplets in the smaller range are collecting similar-sized or smaller drops to populate the larger sizes. One must be careful about trying to do eyeball budgeting with these plots, because they are in log-scale.

3.7.2 Experiment: With sedimentation

In this set of experiments, we allow the droplets to sediment at their terminal velocity v_T out of a layer with prescribed thickness (100 m in our case). This is analogous to having a homogeneous layer cloud with sedimentation at the cloud base.

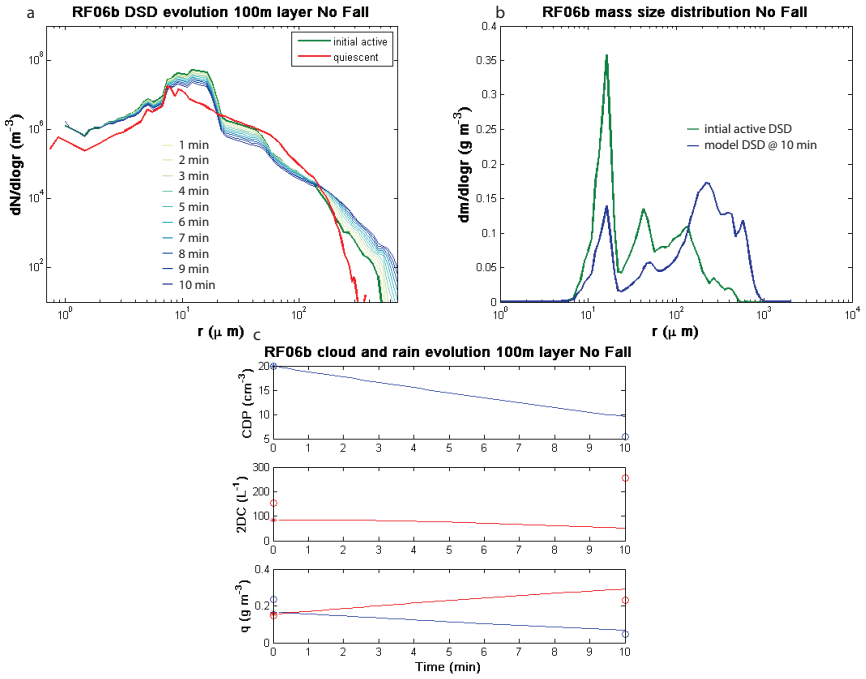

Figure 3.11: Results from 10 min long parcel model simulation where the drop size distribution (DSD) is allowed to evolve by collision coalescence alone. (a) The active cloud DSD used to initialize the model (green) is plotted alongside the quiescent cloud DSD (red) and the DSD from the simulation taken every minute. (b) The initial mass size distribution (green) and the final mass size distribution (blue). (c) The evolution of cloud droplet number concentration (top), where circle at time 0 indicates observed the concentration in the active clouds, as measured by the CDP and the circle at 10 min indicates the concentration in the quiescent clouds. The evolution of drizzle drop number concentration (middle), where circles are similar to top plot, but from 2DC measurements. The evolution of cloud (blue) and drizzle (red) water mixing ratio.

Similar to Fig. 3.11, results are plotted in Fig. 3.12. As in the no sedimentation experiments, we find that N_d and q_c decrease through the simulation. We also see a substantial decrease in q_D, mainly coming from a decrease in drops $>70\,\mu$m. The decrease in q_D reduces the drop in the q_c peak ($\sim 12\,\mu$m) in these simulations. However, we still see a decrease in the drizzle drops in the 25-80 μm sizes. This is indicative of either sedimentation of those drops or self-collection in that region.

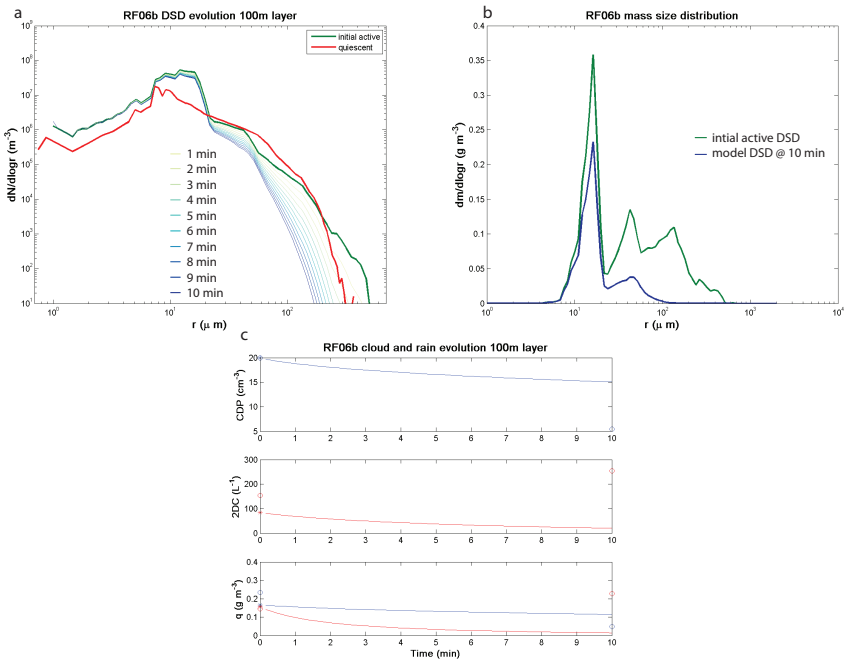

Figure 3.12: Similar to Fig. 3.11 but for results from 10 min long parcel model simulation where the drop size distribution (DSD) is allowed to evolve by collision coalescence and droplets are allowed to sediment out of a 100 m layer.

3.7.3 Experiment: Updraft

The updraft allows some particles to stay lofted within the layer without falling out. In the following experiments, three updraft speeds are used (0.15, 0.3, and 0.6 m s^{-1}), which correspond to v_T for drops with radii 37, 55, and 90 μm.

Results from a simulation with an updraft of 0.3 m s^{-1}are plotted in Fig. 3.13. If we add an updraft to the sedimentation simulations, then we see an increase in drop concentrations for droplets smaller than 100 μm. Whereas concentrations decrease across all radii for droplets in the sedimentation simulation, there are instances where concentration of middle sized drops (60-100 μm) can grow if we include the updraft. In the 0.6 m s^{-1} updraft simulations, the increase in drops with radii $>100\,\mu$m increases and comes closer to the no sedimentation simulations.

Either way, there is no increase in the small drizzle drop range or a maintenance

that leads to the increase in the 2DC number concentrations. An examination of the $0.15\,\mathrm{m\,s^{-1}}$simulation does not show an increase in the area of interest. It just allows the drops with radii $>50\,\mu$m to fallout more easily.

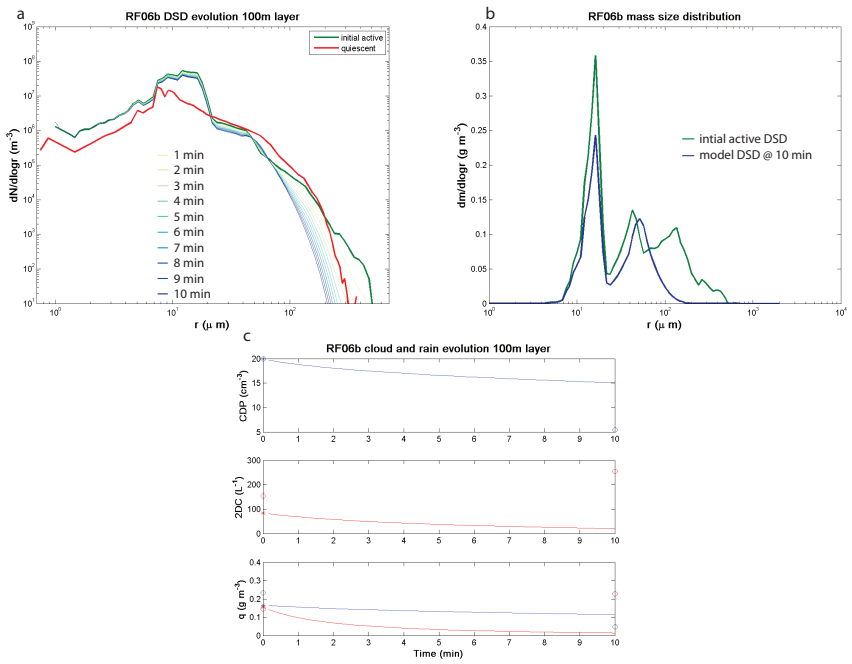

Figure 3.13: Similar to Fig. 3.11 but for results from 10 min long parcel model simulation where the drop size distribution (DSD) is allowed to evolve by collision coalescence, the drops are allowed to fall out of a 100 m layer but are held up by an updraft of speed $0.3\,\mathrm{m\,s^{-1}}$.

3.7.4 Experiment: Condensation included

In this set of experiments, condensational growth of drops is included in the simulation. For the initial set, supersaturation is set to 0.04 %, which is the supersaturation reported by Austin et al. [1995] in their study examining the condensation of large cloud drops and small drizzle drops by radiative cooling.

Results to the experiment are shown in Fig. 3.14. With the addition of supersaturation to the $0.3\,\mathrm{m\,s^{-1}}$ updraft, the most striking feature is the decrease in cloud droplet concentrations of small droplets ($<10\,\mu$m). Because they are small, they move rapidly up in size

over 10 minutes. The peak in cloud droplet mass also does not decrease as rapidly as when condensation is ignored. This feature is partially evident in the number size distribution, but more easily seen in the mass distribution. At larger radii, the difference is not as evident.

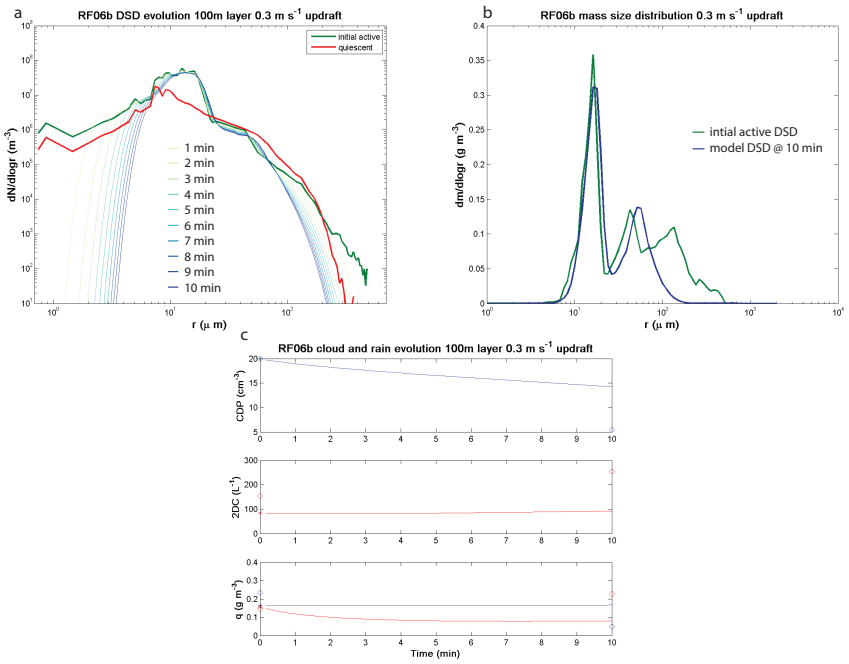

Figure 3.14: Similar to Fig. 3.11 but for results from 10 min long parcel model simulation where the drop size distribution (DSD) is allowed to evolve by collision coalescence and condensation (supersaturation of 0.04 %), the drops are allowed to fall out of a 100 m layer and are held up by an updraft of speed 0.3 m s^{-1}.

3.7.5 Experiment: Supersaturation as a function of updraft and condensation

For these experiments, the MATLAB ode45 ODE solver is used to balance the condensation, droplet growth, and supersaturation equations to run the condensation with variable supersaturations (SSs). The equations that are balanced with the ODE solver can be found in Appendix A. The fixed variables are updraft speed and starting temperature and pressure.

The results for an experiment with an updraft speed of 0.15 m s^{-1} are plotted in Fig. 3.15. As in the fixed supersaturations case, the smaller cloud droplets start to drop off precipitously as the supersaturation pushes the drops to larger sizes. There is no activation

to from new cloud drops in these experiments, so we just see a decrease in the smaller drops. Because there are only so many drops, the drops are being scavenged out by collision-coalescence and drop out of the layer, allowing relatively high supersaturations to develop. Especially for the lower drop concentrations, the supersaturation can get as high as 0.25 % (RF07) when the updraft speed is just $0.15\,\mathrm{m\,s^{-1}}$ or 0.5 % (RF07) for $0.3\,\mathrm{m\,s^{-1}}$. This suggests that unactivated aerosols will start to activate, such that there are little to no interstitial aerosols that are left. The kinetic effect or the size dependent supersaturation are not included, so it is likely that the supersaturation would be even higher if these processes were included. High enough supersaturations can be reached within the updrafts of cumulus clouds or even in the slow ascent (cooling) of quiescent clouds that we turn interstitial aerosols into cloud droplets, and they get scavenged by collision-coalescence processes.

The second effect of the high supersaturations in these simulations is to shift the peak of cloud droplets towards larger radii. Whereas the 0.06 % supersaturation runs did slightly shift the cloud droplets to larger radii, the peak in the cloud drop mass distribution did not shift. In simulations where the updraft was only set to $0.15\,\mathrm{m\,s^{-1}}$, the peak shifts from 16.3 to 17.9 μm. This may seem like a small difference, but the shift spills a large amount of mass into the 25 μm range, which initially lay in the valley between the cloud and drizzle drop masses.

3.8 Summary and conclusions

This chapter utilizes the measured droplet size distributions (DSDs) from the CDP and 2DC probes to estimate the microphysical process rates that control drizzle formation and CCN loss in the POC and neighboring overcast region. These values may be used to allow comparisons with large eddy simulations of POCs to verify whether precipitation is formed in the same way. Based on the analysis, accretion dominates autoconversion in both drizzle water formation, as well as the loss of cloud droplet number concentrations (N_d), which poses as a large sink for CCN-sized aerosols. In the overcast clouds, self-collection of cloud droplets is the dominant process by which N_d is reduced. Getting these process rates correctly will be important if models wish to accurately capture the aerosol-cloud-

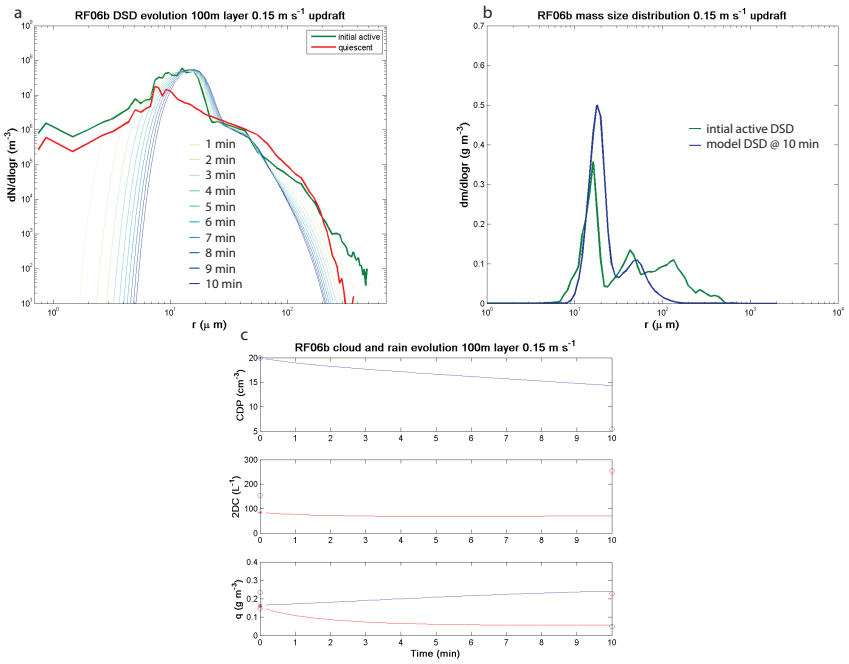

Figure 3.15: Similar to Fig. 3.11 but for results from 10 min long parcel model simulation where the drop size distribution (DSD) is allowed to evolve by collision coalescence and condensation, the drops are allowed to fall out of a 100 m layer and are held up by an updraft of speed $0.15\,\mathrm{m\,s^{-1}}$. The supersaturation is interactive and depends on the cooling rate from the updraft and the condensational growth rate of cloud drops.

precipitation interactions in POCs. Preliminary comparisons between LES and estimated loss rates from the aircraft measurements suggest loss rates from the observations are much higher. Part of the discrepancy may lie in the comparison between column-loss rates and incloud loss rates at the level of the flight leg. Closer inspection is necessary.

The time scale at which all cloud droplets can be completely removed by collision-coalescence, or the removal time scale, in the POCs is under an hour, and much shorter than in the overcast clouds. If we assume that cloud droplet number concentrations do not drastically change over time, this means that replenishment rates of cloud droplets have to be high ($\sim 10\,\mathrm{cm^{-3}\,h^{-1}}$) to keep up with the loss rates. The removal time scales in overcast are longer, roughly 2 hours. Because the POC-to-overcast boundary does not change drastically over time, this means that replenishment rates in the overcast clouds

also have to keep up with the high loss rates due to self-collection of cloud drops. If we assume that the typical lifetime of a parcel stays in the cloud is approximately 15 min [Feingold et al., 2013], then the fraction of cloud drop number that is lost is approximately one-eighth. Therefore, continued replenishment of cloud droplets due to activation at the cloud base of overcast clouds does not appear to be a substantial issue. For all the analyses presented, the lack of vertical structure is a limitation that inhibits generalization to POC-wide loss rates of cloud drops, but in typical drizzling stratocumulus clouds, examining the in-cloud measurements to infer process rates is found not to be an issue that leads to huge overestimation or underestimation of process rates.

Finally, a parcel model with bin microphysics is used to test whether quiescent cloud DSDs can be obtained purely from collision-coalescence and condensation of active cloud DSDs. The quiescent cloud DSDs cannot be obtained from these experiments, leaving us with a puzzle as to how such high concentrations of small drizzle drops are formed and exist in quiescent clouds. On the other hand, we find that given typical stratocumulus updraft speeds (0.3 m s^{-1}), because of the low N_d in POC clouds, supersaturations can reach as high as 0.5 % in the cloud, allowing the activation of even smaller aerosol particles. This may be an important aspect in maintaining the ultra-clean cloud layer.

Chapter 4

PRECIPITATION SUSCEPTIBILITY

4.1 Introduction

General circulation models and weather forecast models are increasingly incorporating processes by which aerosols can affect cloud properties. The effects of aerosols are represented in various ways, including impacts on cloud radiative properties and cloud microphysical processes. However, comparisons of the radiative forcing of aerosols between satellite retrieval-based estimates and global models show large disagreement, with models predicting a larger cooling effect of aerosols [Quaas et al., 2009, Boucher et al., 2013]. Part of the discrepancy may exist because global models inaccurately represent how precipitation depends on the cloud droplet number concentration [Wang et al., 2012].

Attempts to constrain the integrated effect of aerosols on the cloud radiative properties from observations have been confounded by covariances between meteorology and aerosol conditions [Mauger and Norris, 2007, George and Wood, 2010, Gryspeerdt et al., 2014]. Although efforts have been made to use conditional sampling of meteorology to isolate only the aerosol effect, concerns still exist [Gryspeerdt et al., 2014]. Another approach to constrain the effect of aerosols on clouds is to examine the intermediate processes that connect aerosol changes to cloud changes [Sorooshian et al., 2010].

In the cloud lifetime hypothesis proposed by Albrecht [1989], whereby increases in aerosol concentrations lead to increases in cloud lifetime, a crucial part of the argument hangs on the suppression of precipitation due to increases in aerosol concentrations. Our study attempts to constrain the strength of this precipitation suppression using the precipitation susceptibility metric of Feingold and Siebert [2009]. Because studies currently disagree on how susceptibility varies with cloud LWP liquid water path (LWP) [Sorooshian et al., 2009, Jiang et al., 2010, Terai et al., 2012, Mann et al., 2014], we also examine the cloud LWP dependence. The precipitation susceptibility metric S_R, proposed by Feingold and Siebert

[2009], quantifies the fractional decrease of precipitation rate (R) due to a fractional increase in aerosol or cloud droplet number concentration (N), defined as

$$S_R = -\left(\frac{\partial \ln R}{\partial \ln N}\right)_{macro}. \tag{4.1}$$

Initial studies examining the precipitation susceptibility in parcel models, satellite retrievals, and large eddy simulations of cumulus cloud fields noted that the susceptibility initially increases with increasing cloud LWP, reaches a peak value, and then decreases at higher LWP [Feingold and Siebert, 2009, Sorooshian et al., 2009, Jiang et al., 2010]. At the same time, steady-state simple models, aircraft observations, and ground-based cloud radar retrievals have found that susceptibility monotonically decreases with increasing cloud LWP [Wood et al., 2009, Terai et al., 2012, Mann et al., 2014]. Part of the difference lies in what aspect of precipitation is examined. As was noted by Terai et al. [2012], the susceptibility metric can be applied not only to the mean precipitation rate R, but also to the precipitation fraction f (analogous to the probability of precipitation - POP) and the precipitation intensity I (the precipitation rate of clouds that are precipitating). When the susceptibilities of the three variables were examined in aircraft measurements, Terai et al. [2012] found that $S_R \approx S_f + S_I$ and both S_R and S_f decreased with increasing LWP, while S_I stayed constant. Because S_f and S_{POP} are the same in construction, we will henceforth refer to S_{POP} to stay consistent with previous studies [Wang et al., 2012, Mann et al., 2014]. Susceptibilities of all three aspects of the precipitation will be examined in this study.

Even before the susceptibility metric was introduced in the literature, general circulation model (GCM) studies noted that changes in the autoconversion rate in GCMs led to changes in the strength of the aerosol indirect effect [Rotstayn and Liu, 2005]. Subsequent studies examining experiments where the microphysical process rates are perturbed have found the same response [Golaz et al., 2011, Wang et al., 2012, Gettelman et al., 2013]. Furthermore, they have suggested that an overestimate of the contribution of autoconversion to precipitation formation in GCMs may have led to overestimates in the aerosol indirect effect calculated within GCMs [Rotstayn and Liu, 2005, Wang et al., 2012]. The overestimate of the contribution of autoconversion has been argued to be due to the diagnostic treatment of

precipitation in GCMs, where the rain water is not carried over between model time-steps, but is instead diagnosed at every time-step [Posselt and Lohmann, 2008, Gettelman et al., 2013].

The magnitude of the precipitation susceptibility metric and the strength of aerosol indirect effect in GCMs were both examined by Wang et al. [2012] and found to correlate, such that models with strong precipitation susceptibilities also exhibited large changes in cloud radiative properties. In calculating the susceptibility, the authors used S_{POP}. Based on the high S_{POP} calculated in the default version of the Community Atmosphere Model ver.5 (CAM5) compared to the S_{POP} calculated from satellite retrievals, they argued that the aerosol indirect effect within CAM is likely overestimated [Wang et al., 2012].

In this study, we examine a different set of satellite retrievals, focusing on marine stratiform clouds over the tropical and subtropical Pacific to calculate the precipitation susceptibility. Then we use a simple column model based on the diagnostic precipitation treatment, used to diagnose the precipitation in low-level stratiform clouds in CAM, to determine whether we obtain a similar behavior and value of the susceptibility. Finally, we examine the microphysical processes and their relative importance within the diagnostic model to determine whether the relative importance of process rates in the model leads to the observed behavior in the susceptibility. Section 4.2 introduces the various methods to calculate susceptibility, the CloudSat and MODIS combined dataset, and the simple diagnostic model used in this study. Section 4.3 presents the susceptibilities from the CloudSat and MODIS retrievals, and any sensitivity to parameter choices. Section 4.4 presents the susceptibilities from the diagnostic model, any sensitivity to parameter choices, and compares them to those calculated from the satellite retrievals. Section 4.5 compares the satellite and model susceptibilities and assesses the ability of the column model to accurately capture the dependence of precipitation on cloud droplet concentrations. Finally in Section 4.6, we present a discussion and our conclusions.

4.2 Methods

4.2.1 CloudSat and MODIS combined dataset

The satellite retrievals used in this analysis are of warm cloud properties analyzed by Kubar et al. [2009] (K09, hereafter) and Wood et al. [2009]. They pertain to twelve months of CloudSat and MODIS retrievals of cloud LWP, effective cloud droplet number concentration, and radar reflectivity (September 2006 February 2007 and September 2007-February 2008) between 30°S and 30°N and between 100°E and 70°W, mostly consisting of clouds over the tropical and subtropical Pacific Ocean and Gulf of Mexico. K09 found that the relationship between precipitation and cloud properties were insensitive to the months used. Given the strict criteria to screen for stratiform clouds whose microphysical retrievals are less affected by cloud edges and heterogeneities [Zhang and Platnick, 2011], the cloud types analyzed here are low-level, marine, stratiform clouds. Of all MODIS-detected clouds in the region and during the time period, 21 % of them are included in this analysis (K09). The MAC06S0 version of the MODIS/Aqua level-2-cloud subset and the CloudSat 2B-GEOPROF data are used. Cloud liquid water path (LWP) is retrieved using the cloud optical thickness (τ) and effective radius (r_e) (K09). Effective cloud droplet number concentration (N_{eff}) is estimated assuming the clouds are adiabatic using the method of Bennartz [2007] (K09). Because accurate estimates of N_{eff} cannot be made around broken clouds, data is included only if the MODIS retrievals recorded a cloud fraction of 100 % in a rectangle with sides of 5 km along the satellite track and 15 km across the satellite track. The column maximum reflectivity is used to infer the presence of drizzle and to estimate precipitation rate. A reflectivity threshold of -15 dBZ is used to distinguish precipitating from non-precipitating clouds [Comstock et al., 2004, Kubar et al., 2009, Terai et al., 2012], and a $Z-R$ relationship from Comstock et al. [2004], based on warm stratocumulus clouds, is used to estimate precipitation rate from the column maximum reflectivity.

The analysis is constrained to warm, marine, stratiform clouds with optical depth greater than 3 (K09) due to MODIS retrieval uncertainties when clouds are thin or broken [Zhang and Platnick, 2011]. Thus, we are not considering the response of cumulus precipitation to aerosol concentrations and exclude thin clouds in the analysis or the response of mid-

latitude stratocumulus clouds, a large proportion of which have been found to precipitate as well [Leon et al., 2008, Muhlbauer et al., 2014]. However, unlike previous precipitation susceptibility studies of marine stratocumulus [Terai et al., 2012, Mann et al., 2014], we examine clouds over a wide geographic area with different ranges of aerosol and meteorological conditions. Because our retrievals of LWP and N_{eff} require sunlight, we restrict ourselves to examining clouds and precipitation observed ∼13:30 local, while acknowledging that diurnal differences in precipitation exist and that 13:30 is near the diurnal minimum of marine stratocumulus cloud cover [Leon et al., 2008, Burleyson et al., 2013].

4.2.2 Diagnostic model

The column diagnostic model used in this study has fundamental elements of the diagnostic treatment of precipitation described by Morrison and Gettelman [2008]. The diagnostic treatment allows the representation of precipitation given typical GCM time steps (∼20 min) without the need to consider the Courant criterion for droplet sedimentation [Ghan and Easter, 1992, Morrison and Gettelman, 2008]. The fundamental equation of diagnostic precipitation assumes that the fallout of precipitation is balanced by the production of precipitation by autoconversion (A_u) and accretion (A_c) at each level, such that the following relationship holds

$$\frac{d\left(vq_R\right)}{dz} = A_u + A_c, \tag{4.2}$$

where q_R is the rain water mixing ratio, v is the mass weighted mean fall velocity of rain, and z is the height coordinate.

As in Morrison and Gettelman [2008], A_u and A_c are represented by the Khairoutdinov and Kogan [2000] parameterization based on bulk cloud and rain properties

$$A_u = A{q_c}^{2.47}{N_d}^{-1.79} \tag{4.3}$$

and

$$A_c = B\left(q_c q_R\right)^{1.15}, \tag{4.4}$$

where $A = 7.42 \times 10^{13} \, (\mathrm{kg\,m^{-3}})^{-1.47}$, q_c is the cloud water mixing ratio, N_d is the cloud droplet number concentration, and $B = 67 \, (\mathrm{kg\,m^{-3}})^{-1.3}$. The model runs from the top of the cloud and follows down the sedimentation of the rain in the cloud. At the top level, q_R at the first grid level ($q_{R,1}$) is formed solely from autoconversion over the time step Δt, such that

$$q_{R,1} = A_u \Delta t. \tag{4.5}$$

For all other grid levels below the first one, we discretize Eq. 4.2 so that it applies to each grid level of our column model and obtain the following relationship for q_R at each grid level i:

$$q_{R,i} = q_{R,i-1} + \frac{\Delta z}{v_{i-1}} \left(A q_{c,i}^{2.47} N_d^{-1.79} + 67 \, (q_c q_R)^{1.15} \right), \tag{4.6}$$

where Δz is the geometric grid level thickness, the subscript i indicates variables at grid level i and subscript $i-1$ indicates variables in the grid level above level i. The mass-weighted mean fall velocity of rain v is obtained from an empirical fit of the drizzle droplet size distribution, which gives us the relationship between fall v and q_R,

$$v = 10.11 q_R^{0.25}. \tag{4.7}$$

Consistent with the microphysics scheme used in CAM5, a modified mid-point method is used to determine estimates of v_{i-1} (pers. comm. Hugh Morrison). In contrast to the microphysics scheme in CAM5, only q_R is diagnosed, and the rain drop number concentration (N_R) is not. A sensitivity study was conducted in which both N_R and q_R were diagnosed; this did not change the susceptibilities. For each set of experiments, we assume that N_d is constant with height, which observations show to be a good estimate in stratiform clouds [Wood, 2005], and that the cloud water profile is adiabatic and hence increases linearly with height [Pawlowska, 2003]. Although we conduct sensitivity experiments where the cloud water profile is changed, in the base case, the cloud LWP is controlled by increasing the depth of the cloud. The largest Δz used in the standard simulations is 10 m. Each simulation run is initialized with a particular N_d and cloud LWP profile. The precipitation rate

at the cloud base is used for calculating all susceptibilities.

We also conduct runs with the stochastically-peturbed microphysics, wherein autoconversion (A_u) and accretion (A_c) process rates are perturbed by a log-normally-distributed coefficient whose width depends on the ratio between the bulk and bin-estimates of A_u and A_c based on aircraft in situ measurements taken during the VOCALS Regional Experiment [Mechoso et al., 2014]. For a particular simulation, for example, the perturbed autoconversion rate $A_{u,p}$ at each level will take the form

$$A_{u,p} = X_{Au} A_u, \tag{4.8}$$

where X_{Au} is the coefficient $X_{Au}\sim\exp(N(0,(\sigma_{Au}^2)))$, σ_{Au} is the geometric standard error derived from the VOCALS measurements, and A_u is the unperturbed autoconversion rate. The geometric standard error of the bulk-estimate from the bin-estimate is used to construct a log-normal distribution with a geometric mean of 1 from which the coefficient is chosen randomly for each simulation run. For both process rates, the same coefficients X_{Au} and X_{Ac} are used throughout a simulation.

Based on the aircraft observations, the geometric standard error of A_u (σ_{Au}) is 2.47 and 0.79 for A_c (σ_{Ac}). Then the diagnostic model is run 1000 times for a given set of cloud LWP and N_d conditions with varying combinations of uncorrelated coefficients.

4.2.3 Susceptibility metric

The parameters that go into calculating the susceptibility can vary from study to study. For example, instead of the aerosol concentration N, the aerosol index (AI) [Nakajima et al., 2001] or the cloud droplet number concentration N_d, as is the case for this study, may be used. Susceptibilities are typically calculated in bins of cloud LWP to minimize the effect of LWP in contaminating the susceptibility estimates. A couple methods exist to calculate the susceptibility in each LWP bin, whether using linear regression in log-log space and using the slope to calculate susceptibility [Sorooshian et al., 2010] or binning the data by N or N_d, calculating the bin-mean N and R to calculate the susceptibility [Terai et al., 2012, Wang et al., 2012, Mann et al., 2014]. Most of the susceptibility calculations in this study

are made by taking linear regression of the bin-mean N_d and R in bins of N_d, but the tercile log-difference method of Terai et al. [2012], in which the log-difference in the means of the bottom and top terciles of N are used to calculate the susceptibility, is also used to show that they give nearly identical susceptibility values.

4.3 Results: Satellite susceptibility

4.3.1 Susceptibility with -15 dBZ

Before calculating the susceptibility, the satellite data are first binned according to LWP and N_{eff} values. Because there are approximately 400000 CloudSat shots used in the analysis and we divide the data into ten bins of LWP and ten of N_{eff} with relatively equal number of shots, each bin of given LWP and N_{eff} contains approximately 4000 shots, ranging from 1200 to 5500 (middle 90th percentile of 3090-4660). For each of the ten LWP bins, susceptibilities are calculated by taking the linear regression of the bin-mean precipitation metric R, POP, or I against the mean N_{eff}. We use a threshold of -15 dBZ, as in previous studies, to determine drizzling and non-drizzling clouds. We find that S_R equals approximately 0.6 at low LWP and slightly decreases to 0.5 with increasing LWP (Fig. 4.1a). This is in contrast with other observational studies of stratocumulus, which found that susceptibility decreased by a factor of two to four with increasing cloud LWP [Terai et al., 2012, Mann et al., 2014]. Note the large error bars for the susceptibility values at low LWP. These error bars are the 95 % confidence intervals in the slopes calculated by linear regression. Feingold et al. [2013] found that in their parcel model simulations, susceptibility was not just a function of LWP, but also of N_d, suggesting that the susceptibility is not linear across all N_d. That is what we find in our dataset, which we will expand on in Sect. 4.5.

If we break down S_R into S_{POP} and S_I, as in Terai et al. [2012], we find that S_{POP} decreases with increasing LWP (Fig. 4.1b), whereas S_I increases with increasing LWP. As in [Terai et al., 2012], $S_R \approx S_{POP} + S_I$. The decrease of S_{POP} with increasing LWP agrees with previous observational studies [Terai et al., 2012, Mann et al., 2014], but the increase in S_I does not [Terai et al., 2012]. The negative S_I values at low LWP are particularly difficult to explain in the context of our current understanding of how cloud droplet number con-

centrations affect warm rain processes. What Fig. 4.1 implies is that at LWP $< 150\,\mathrm{g\,m^{-2}}$, increased cloud droplets reduces frequency of precipitation (positive S_{POP}), but increases intensities (negative S_I). To verify whether this is an artifact of the method by which we calculated susceptibility, we use the tercile log-differencing (TLD) method, used by Terai et al. [2012], to calculate the susceptibility in Fig. 4.1d, and still find similar behaviors for S_R, S_{POP}, and S_I. Using the TLD method, the data is binned into terciles of N and then the log-differences in the mean N and R between the upper and lower terciles are used to calculate the susceptibility.

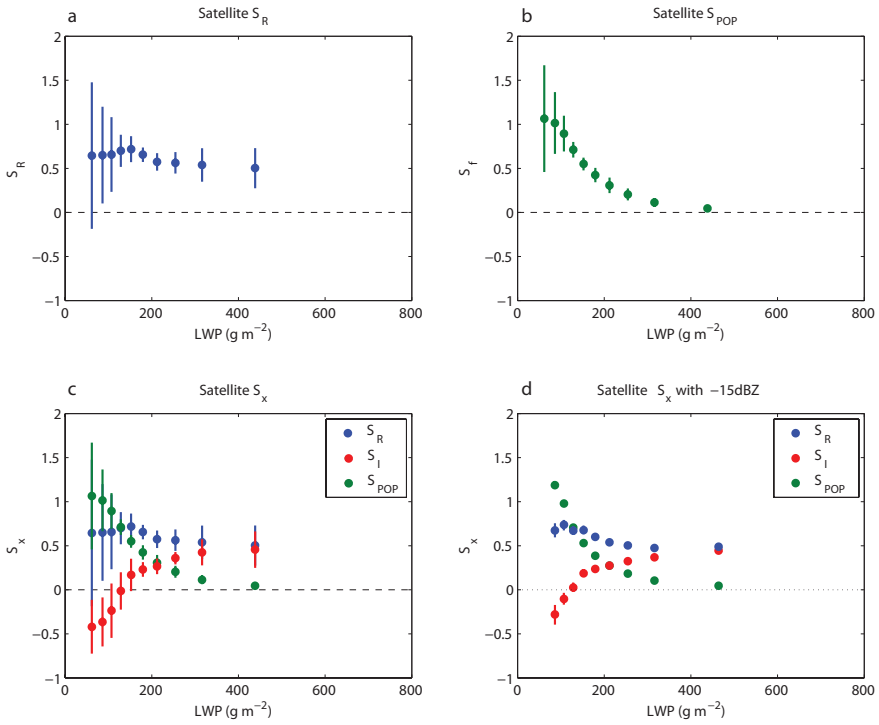

Figure 4.1: a) Susceptibility of mean precipitation rate (S_R) as a function of LWP, based on the satellite data and calculated using linear regression on N_{eff}-binned data. b) Susceptibility of probability of precipitation (S_{POP}) as a function of LWP, based on same data and method. c) S_R, S_{POP}, and susceptibility of precipitation intensity (S_I) as a function of LWP, based on same data and method. d) S_R, S_{POP}, and S_I, based on same data, but using the TLD method to calculate susceptibilities [Terai et al., 2012].

4.3.2 0 dBZ threshold

Previous studies have examined the susceptibility using a different precipitation threshold than the -15 dBZ that we have used [Sorooshian et al., 2009, Wang et al., 2012, Mann et al., 2014]. We examine how changing the threshold changes our results. In Fig. 4.2, we plot the susceptibility as a function of LWP if we use a minimum threshold of 0 dBZ. Increasing the minimum threshold leads to S_I of near zero values across all LWP, and S_{POP} values mostly represent S_R values. Although the S_{POP} at low LWP values decrease as a result of changing the threshold, we find that the overall S_{POP} values at higher LWP ($>150\,\mathrm{g\,m^{-2}}$) remain little changed. If anything, we have an increase in S_{POP}. This is mostly in agreement with Mann et al. [2014] who examined the sensitivity of results to changing thresholds and found little change, although Jiang et al. [2010] and Terai et al. [2012] found that susceptibilities are sensitive to choice of threshold.

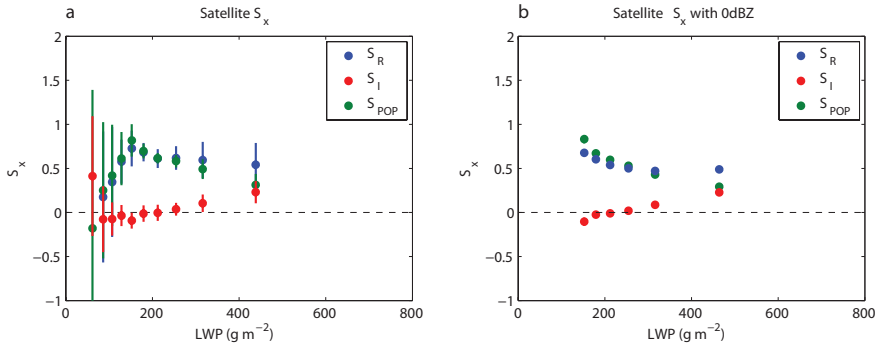

Figure 4.2: a) S_R, S_{POP}, and S_I as a function of LWP, as in Fig. 1c, but using a threshold of 0 dBZ to distinguish precipitating clouds. b) Same as a), but using the TLD method [Terai et al., 2012].

4.3.3 Regional differences

We acknowledge that N_{eff} and LWP are not the only controls on precipitation rate. L'Ecuyer et al. [2009] found that if they further binned their data by the lower tropospheric stability, in addition to LWP and aerosol index (AI), the proxy they used for aerosol concentration, they found that the probability of precipitation for clouds with LWP $> 500\,\text{g}\,\text{m}^{-2}$ were greater in stable conditions, regardless of high or low aerosol conditions. We have tried to account for stability regimes by exclusively analyzing marine stratiform clouds, but our susceptibility results may still be affected by mixing different lower tropospheric stability (LTS) regimes. Therefore, we examine the susceptibility metric in different regions of the tropical/subtropical Pacific and Gulf of Mexico to examine whether the behavior of the susceptibility varies by region. This will also allow us to examine whether the negative S_I values at low LWP are found across all regions, or whether it is a signal that grows out of including a particular region in the basin-wide analysis.

In Fig. 4.3, we examine S_R, S_{POP}, and S_I in seven regions, which largely correspond to regions identified by K09. We have not examined the ITCZ and SPCZ, where deep convective clouds dominate. The far southeast Pacific area is modified from that defined by K09 to encompass the area sampled during VOCALS-REx [Mechoso et al., 2014]. These seven regions encompass different aerosol and meteorological regimes. For example, due to continental influences, the Asian coast has a much higher mean N_{eff} and also a higher LWP, compared to the remote SEP (K09). Similar to the susceptibility that we calculated from all of the data, the susceptibilities here are calculated from binning the data in each region by LWP and N_{eff} and calculating the susceptibility using linear regression. Instead of the 100 total bins of (LWP, N_{eff}) used to calculate the susceptibility in the total data, the data in each region are binned into 25 total bins of (LWP, N_{eff}) such that the same number of shots exists in each bin.

In Fig. 4.3, there is a wide range of values and behaviors of S_R, S_{POP}, and S_I, which highlights how susceptibilities estimated from measurements made in one region will not necessarily agree with those from a different region. At the same time, however, consistent behaviors do appear. For example, S_{POP} across all regions decreases with increasing LWP.

The value of S_{POP} is lowest in the two most polluted regions (Gulf of Mexico and Asian coast). This behavior is consistent with future discussion in Fig. 4.7a, where S_{POP} appears to decrease for low LWP and high N_{eff}. In addition, it appears that S_I increases with increasing LWP. Whether the increase is large and at what LWP that increase occurs varies by region. Furthermore, at low LWP, S_I is statistically indistinguishable from zero at low LWP. S_R has the most diversity across the regions, and appears to largely be determined by the addition of S_I and S_{POP} behaviors, as in the Gulf of Mexico, where the increase in S_I is larger than the decrease in S_{POP} at low LWP, leading to an increase in S_R with LWP. We are therefore left with strong confidence in the universal decrease of S_{POP} with increasing LWP, but the behavior and value of S_R is more variable across regions and dependent on the behavior and value of S_I.

We expect the susceptibilities calculated over the VOCALS southeast Pacific region to agree with susceptibilities calculated by Terai et al. [2012]. Because the geographic regions over which they are calculated are the same, this provides a rough comparison of what different observational platforms can have on the susceptibility values. First, S_R values from Fig. 9 of Terai et al. [2012] agree with the values found in the southeast Pacific in Fig. 4.3. The sharp decrease in S_{POP} with increasing LWP is also observed in both results. However, the increase in S_I with increasing LWP, found in Fig. 4.3, is not found in the results of Terai et al. [2012]. Particularly, although the S_I values at LWP $\sim 200\,\mathrm{g\,m^{-2}}$ agree between the two estimates, at LWP $< 100\,\mathrm{g\,m^{-2}}$, the satellite data here suggest an $S_I \sim 0$, whereas, the results of Terai et al. [2012] suggest an S_I of 0.5 that stays constant with increasing LWP. Although not shown in Terai et al. [2012], we should note that S_I slightly increases (0.5 to 0.7) with LWP in the range of LWP that they examined. Part of this discrepancy between the satellite and aircraft retrievals may be due to sampling differences between the satellite and aircraft radar. Comparisons between the satellite and aircraft of reflectivities as functions of LWP and N_d will be necessary to better understand why this discrepancy exists.

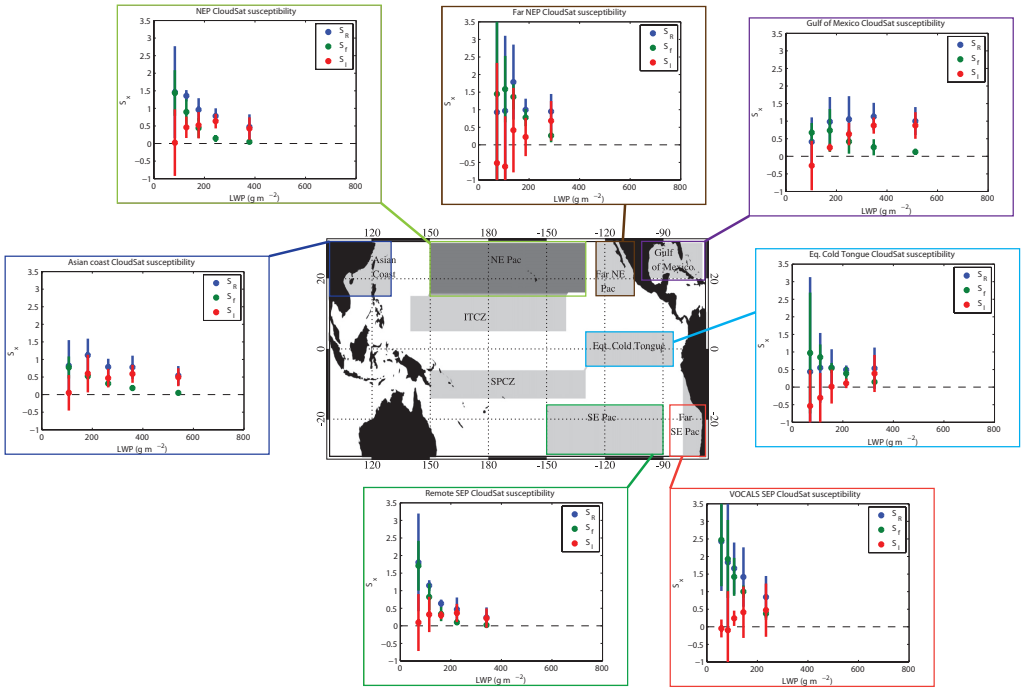

Figure 4.3: a) S_R, S_{POP}, and S_I as a function of LWP in seven different ocean basins: Asian coast, northeast Pacific, far northeast Pacific, Gulf of Mexico, equatorial cold tongue, VOCALS southeast Pacific, and remote southeast Pacific (adapted from Kubar et al., 2009).

4.4 Results: Diagnostic model susceptibility

4.4.1 Susceptibility with stochastic physics

100 sets of 1000 simulations of the column model are run, each initialized with the mean cloud LWP and cloud drop number concentration corresponding to each of the bins of the satellite data. The autoconversion and accretion rates are stochastically perturbed as described in Sect. 4.2. The susceptibility is then calculated, as with the satellite data, for each of the ten LWP bins using standard linear regression in log-space. This allows us to compare the susceptibilities for similar clouds between the satellite and column model. Using a threshold of $0.14\,\mathrm{mm\,d^{-1}}$, which according to the $Z - R$ relationship of Comstock et al. [2004], corresponds to a reflectivity threshold of -15 dBZ, S_R, S_{POP}, and S_I are

calculated and plotted as a function of LWP in Fig. 4.4. S_R decreases as a function of LWP, from a value ∼1.3 at 60 g m^{-2}, decreasing to a value of ∼0.4 at 420 g m^{-2}. If we decompose S_R into S_{POP} and S_I, we find that they are generally additive, such that $S_R \approx S_{POP} + S_I$ and that S_R decreases mainly because S_{POP} decreases. S_I, on the other hand, maintains a relatively constant value across the range of LWP examined. If we do not set a threshold of 0.14 mm d^{-1} to calculate susceptibility, we find that we get nearly identical values of S_R, whereas $S_{POP} = 0$ in that case. Because a minimum detection level for precipitation exists for all observations of precipitation, we find that defining a threshold provides a more consistent comparison of susceptibilities between the satellite retrievals and diagnostic model.

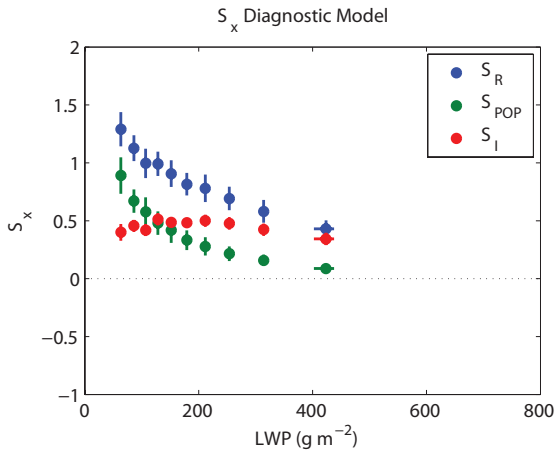

Figure 4.4: S_R, S_{POP}, and S_I as a function of LWP, based on the stochastically-perturbed-physics column model simulations and calculated using linear regression on N_{eff}-binned data. The error bars in S_x represent 95 % confidence intervals of the regression slope. The error bars in LWP represent the range in LWP used in the diagnostic model. The range of LWP and N_{eff} and precipitation threshold used in this figure are the same as that used for Fig. 1c.

4.4.2 Model sensitivity studies

To explore the sensitivities of our results to model configuration, we first examine how the susceptibility changes if we run the diagnostic model without stochastic variations in the

autoconversion and accretion rates. S_R as a function of the LWP is shown in Fig. 4.5a. The susceptibility value starts with a value of approximately 2 and decreases steadily until it has a value of approximately 1 at a LWP of $420\,\mathrm{g\,m^{-2}}$. Compared to S_R from the runs with perturbed physics, the values are generally much higher. No minimum threshold was set for the precipitation rate in Fig. 4.5a and $S_{POP} = 0$, because each combination of LWP and N_d only results in one particular precipitation rate. Therefore, we can get a decrease in S_R with LWP, without invoking stochastic variations in the microphysical process rates. However, the decrease in S_R occurs at much higher LWP compared to what we see in Fig. 4.4 and the relative decrease is smaller.

We also examine how S_R responds if we perturb the cloud water profile, the number of grid levels, and σ_{Au} and σ_{Ac} used to constrain the stochastic variance in the autoconversion (A_u) and accretion (A_c) in the model. We examine the sensitivity of the susceptibility to changes in the cloud water mixing ratio (q_c) profile in Fig. 4.5b. In all the previous analyses, we have assumed that q_c increases linearly with height (adiabatic cloud). We find that S_R varies by ~ 0.4 depending on whether we assume that q_c is constant with height or whether it increases quadratically with height. S_R systematically decreases as the q_c profile becomes more uniform with height. We define that the cloud of thickness 1000 m has a LWP of $1000\,\mathrm{g\,m^{-2}}$ for each profile shape and use the corresponding coefficient to produce the q_c profiles of clouds with other LWP values. Therefore, while the LWP values do not change with different profile shapes, the corresponding cloud thickness does.

In Fig. 4.5c, we perform a sensitivity test where we reduce the number of vertical grid levels of the column model from the default 100 levels to 10 and 3 levels and calculate the susceptibilities. The susceptibility increases as we reduce the number of grid levels. S_R for 3 levels is 2.1, compared to 1.3 for 10 and 100 levels in the lowest LWP bin, whereas they are indistinguishable for the highest LWP bin. This is important to note, considering that the vertical grid levels of most GCMs is on the order of 500 m. Indeed Ghan and Easter [1992] noted that the vertical spacing used by current GCMs can cause errors in precipitation rates. The reason for this increase may be due to the increased use of limiters and increased importance of the top grid level, where autoconversion is the only process, in determining the susceptibility.

Finally in Fig. 4.5d we examine how sensitive our susceptibility values are to varying σ_{Au} and σ_{Ac} that we calculated from the aircraft observations. Although we find that S_R is largely insensitive to varying σ_{Ac} (halving only resulted in a change of S_R of 20 % at most), S_R is highly sensitive to halving σ_{Au}. We can see that S_R for the lowest LWP bin more than doubles from 1.3 for the default σ_{Au} to 3 if we halve σ_{Au}. Not surprisingly, the largest S_R values are found if we halved both σ_{Au} and σ_{Ac}, although the changes are not additive. The increase in S_R for the case where both σ_{Au} and are halved is largely due to a dramatic decrease in the mean precipitation rate at higher N_{eff} values. If we examine the S_R without the $0.14\,\text{mm}\,\text{d}^{-1}$ minimum threshold, we see that the increase is not as dramatic (the maximum S_R increases to 2 instead of 3). The implications of this strong sensitivity of our susceptibility values to σ_{Au} is that the agreement between the susceptibilities obtained from the satellite and the diagnostic model may be coincidental. Overall, we find that susceptibilities of clouds $< 200\,\text{g}\,\text{m}^{-2}$ are especially sensitive to parameter choice.

4.5 Results: Satellite and model comparisons

4.5.1 Susceptibility as a function of LWP and N_{eff}

As we mentioned in Sect. 4.3, the $\log R$ vs. $\log N$ relationship, especially at low LWP, is not linear. As a result, we see particularly large error bars in the susceptibility values at low LWP in Fig. 4.1a. To examine the variation in susceptibility as a function of N_{eff}, in addition to LWP, we calculate the susceptibility for each LWP and N_{eff} bin by using three consecutive N_{eff} bins, rather than the full range of N_{eff}, to calculate the susceptibility. We might expect large uncertainties in the susceptibilities that we calculate from the slopes calculated from a linear regression of only three points, but this method allows us to better see whether there are systematic changes in susceptibility with N_{eff}. In previous sections we have found that satellite-derived S_I is negative for clouds with low LWP (Fig. 4.1)c) and that the S_{POP} behavior in satellite data and diagnostic model agree. We can examine both of these issues in more detail by considering how susceptibility varies with N.

S_R (Fig. 4.6a) and S_{POP} (Fig. 4.6b) are plotted as a function of LWP and N_{eff} from the satellite data. For comparison, S_R (Fig. 4.6c) and S_{POP} (Fig. 4.6d) from the diagnostic

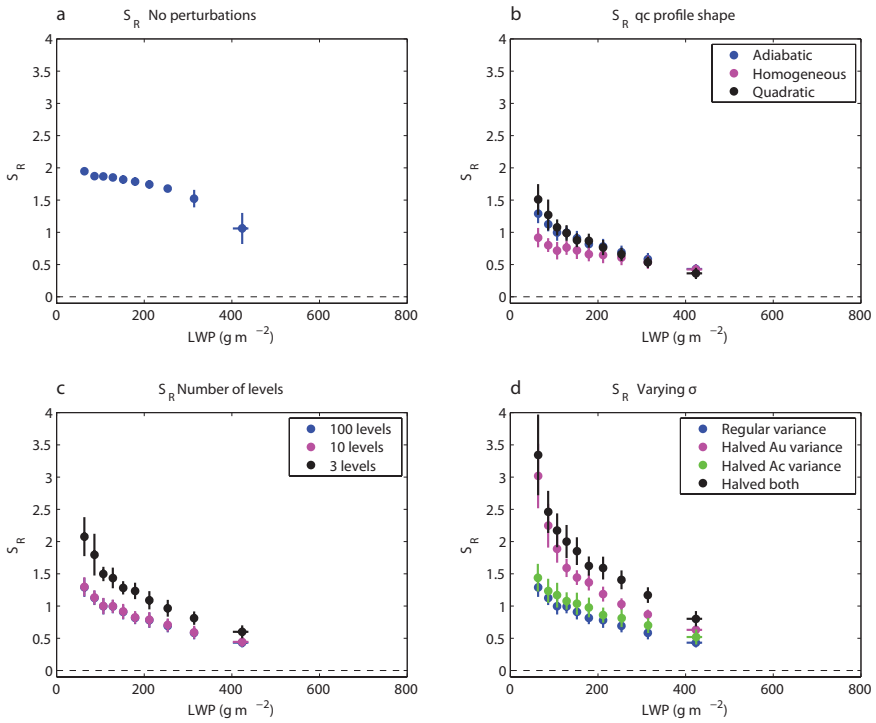

Figure 4.5: a) S_R as a function of LWP for simulations where autoconversion and accretion rates are not perturbed. b) S_R as a function of LWP for sensitivity experiments where the shape of q_c profile is perturbed from the default adiabatic profile (blue) to constant q_c (magenta) and quadratically-increasing q_c (black). c) S_R as a function of LWP for sensitivity experiments where the number of grid levels is reduced from 100 (default blue) to 10 (magenta) and 3 (black) levels. d) S_R as a function of LWP for sensitivity experiments where standard deviations σ_{Au} and σ_{Ac} that control the variance allowed in the autoconversion and accretion rates is changed from the regular variance (blue) to halving σ_{Au} (magenta), halving σ_{Ac} (green), and halving both σ_{Au} and σ_{Ac} (black).

model with stochastically-perturbed microphysics is also shown. In the satellite data, we find that S_R is highest at low LWP and low N_{eff} and decreases with increasing LWP and N_{eff}, such that susceptibilities are zero or slightly negative in low-LWP/high-N_{eff} and high-LWP/low-N_{eff} clouds. This largely follows the behavior of the S_{POP}. The drop off of S_{POP} at higher N_{eff} at low LWP likely explains why the S_{POP} values in the Gulf of Mexico and off the Asian coast in Fig. 4.3 are lower than the more remote regions. As can be inferred from the plots of S_R and S_{POP}, S_I is negative in low-LWP/high-N_{eff} clouds and positive in high-LWP/high-N_{eff} clouds (not shown).

If we compare the satellite susceptibilities with those from the diagnostic model, we find a different pattern. In the diagnostic model, both S_R and S_{POP} are highest in low-LWP/high-N_d clouds and decreases with increasing LWP and decreasing N_d. S_I, on the other hand, does not have a discernible pattern, where values are mainly around 0.5 (not shown). Whereas S_{POP} in the diagnostic model appears to largely have the same value and behavior as that observed in the satellites, its dependence on N_{eff} is very different. On the other hand, the susceptibilities in high-LWP/low-N_d clouds agree between the satellite and model.

4.5.2 Probability of precipitation (POP) values from model and satellites

Although our S_{POP} values from the satellites and diagnostic model agree well (Fig. 4.1b and Fig. 4.4), this agreement does not equate to model POP agreeing well with those estimated from the satellite retrievals. We examine a direct comparison of POP between the satellite observations and model in Fig. 4.7. The model tends to overestimate POP, especially for clouds with LWP $< 200\,\text{g}\,\text{m}^{-2}$. This is analogous to studies that have found that GCM precipitation tends to be too frequent and light [Stephens et al., 2010]. Because the actual precipitation rate determines the role of precipitation as a sink of water, care must be taken when examining the susceptibility values and trying to infer what it implies about the effect that aerosols have on precipitation-mediated cloud properties.

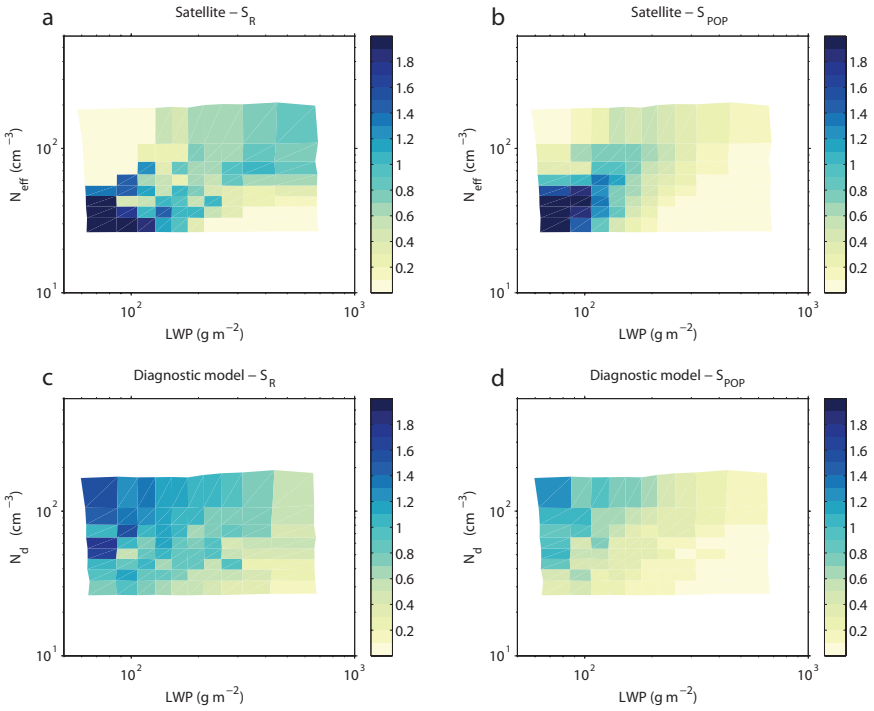

Figure 4.6: Susceptibility as a function of LWP and N_{eff} calculated from linear regression of three adjacent N_{eff} bins. S_R (a) and S_{POP} (b) from the satellite data are shown in the top row. S_R (c) and S_{POP} (d) from the column model are shown in the top row.

4.5.3 Process rates and susceptibility

Although the precipitation rates from the diagnostic model overestimate the probability of precipitation, we can use information on the process rates within the model to examine what aspects of the model lead to the simulated susceptibility. In addition to the fall velocity v of precipitation, autoconversion (A_u) and accretion (A_c) are the two main microphysical processes that determine the rain water mixing ratio at cloud base, and hence the cloud base precipitation rate. Previous studies have suggested that the proportion of autoconversion and accretion rate within the clouds determine the behavior of susceptibility with increasing cloud LWP [Wood et al., 2009, Terai et al., 2012, Feingold et al., 2013]. Autoconversion has a strong sensitivity to the cloud droplet number concentration (N_d), while accretion is not explicitly dependent on N_d (see Eq. 4.3 and 4.4). The argument follows that with

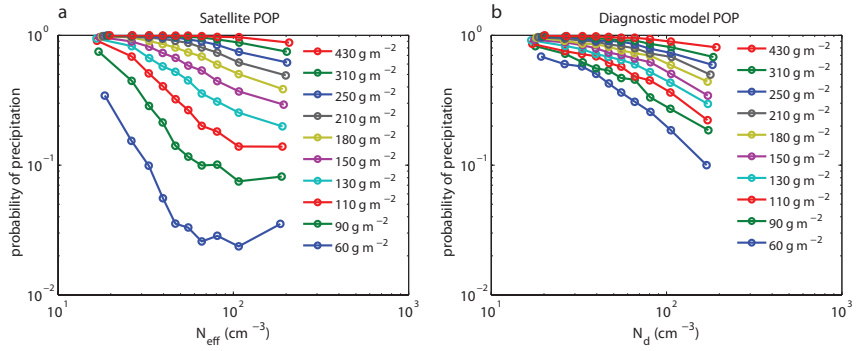

Figure 4.7: Probability of precipitation (POP) as a function of cloud droplet number concentration (N_{eff} or N_d) from satellite retrievals (a) and from the diagnostic model (b). Each line corresponds to the relationship in a particular LWP bin.

increasing importance of accretion in precipitation formation, autoconversion plays a smaller role in precipitation formation and the sensitivity of precipitation to N_d weakens, leading to a decrease in susceptibility. Examining, the accretion-to-autoconversion ratio (A_c/A_u) in Fig. 4.8, we see that the highest A_c/A_u ratios are found at high LWP and high N_d, when in Fig. 4.6c, we found the lowest susceptibility values is at high LWP and low N_d. Therefore, we find that although the A_c/A_u at first glance appears to be a good predictor of S_R, the relationship between A_c/A_u and S_R is not straightforward. Compared with A_c/A_u values estimated from VOCALS incloud profiles reported by Gettelman et al. [2013], we can see that the model generally underestimates the ratios. The profile estimates also do not show the general shift in A_c/A_u with LWP and N_d as seen in the model. It is also important to note the difference in the areas of highest and lowest A_c/A_u between Fig. 4.8 and Fig. 4a of Feingold et al. [2013]. The highest value of A_c/A_u in the diagnostic model is found at high LWP and high N_{eff} values, while in the Feingold et al. [2013] study with parcel models, it is found at high LWP and low N_{eff} values. These differences exist because of different model assumptions. The parcel model assumes that precipitation formation occurs in the upward moving parcel while the column model assumes precipitation formation is balanced by drop sedimentation and accumulates lower in the cloud. The difference leads to different processes being important in different types of clouds. It is likely that the parcel model,

where precipitation formation occurs over a single convective event, is more applicable to cumulus clouds, whereas the column model, which is based on the steady state assumptions balancing precipitation formation and loss, is more applicable to stratiform clouds.

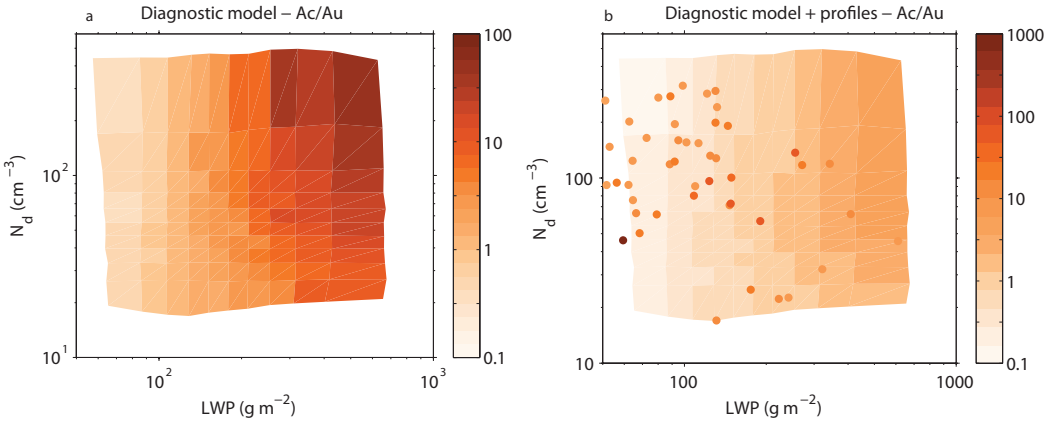

Figure 4.8: (a) The column-mean accretion-to-autoconversion ratio (A_c/A_u) as a function of LWP and N_d in the diagnostic model. (b) The same A_c/A_u from the model, but with column-mean A_c/A_u estimated from VOCALS incloud profiles [Gettelman et al., 2013]. Note the change in the color bar scale in (b).

4.6 Discussion and conclusions

In this study we use satellite retrievals and a simple diagnostic model to examine the precipitation susceptibility metric in marine stratiform clouds. Starting with the results that we find most confidence in, we find from the combined CloudSat-MODIS satellite dataset that the susceptibility of probability of precipitation (S_{POP}) decreases with increasing cloud LWP. This decrease in S_{POP} is in agreement with previous observations [Terai et al., 2012, Wang et al., 2012, Mann et al., 2014]. The value of S_{POP} is ∼1 at low LWP and decreases with increasing LWP. The magnitude is much larger than the values found by Wang et al. [2012], robust regardless of choice of region, and weakly sensitive to choice of dBZ threshold. The S_{POP} values are largely in agreement with Mann et al. [2014], who also found that their S_{POP} values were higher than those reported by Wang et al. [2012]. Although Wang et al. [2012] also used satellite retrievals to calculate S_{POP}, differences in the dataset exist. We

speculate the difference largely arises from the use of AI and N_{eff} as aerosol proxies, but further studies will be necessary to determine whether this difference explains the difference in the S_{POP}. The difference might also exist due to different types of clouds (cumulus vs. stratocumulus) that are examined, as suggested by Feingold et al. [2013].

We find that the decrease in S_{POP} is not just present in the satellite data, but that the simple diagnostic precipitation model predicts a decrease in S_{POP} with increasing LWP as well. We find that the values of S_{POP} calculated from the diagnostic model also agree with those from the satellite dataset. The trends in S_{POP} and S_R from the diagnostic model are insensitive to model parameters, such as number of grid levels or the variance parameter used to constrain the scatter in autoconversion and accretion rates in the perturbed physics runs, but their magnitudes are sensitive. With a decreasing number of vertical grid levels and decreasing value in the variance parameter for autoconversion, both S_{POP} and S_R increase. Although the model cannot help constrain the susceptibility values expected in the GCMs, it helps to inform what type of behavior we would expect of the susceptibility if we solely consider how the diagnostic precipitation treatment affects susceptibility.

From the simple diagnostic model, we are also able to examine whether accretion-to-autoconversion ratios are critical in determining how susceptibility changes with increasing LWP. Previous studies have speculated a tight relationship between the two [Wood et al., 2009, Terai et al., 2012], although an LES study of cumulus cloud fields found otherwise [Jiang et al., 2010]. We find that although the decrease in susceptibility with LWP in the diagnostic model is accompanied by an increase in the accretion-to-autoconversion ratio in the perturbed physics runs, simulations with stripped down versions of the model show that susceptibility can remain constant with increasing LWP, even when there are large increases in the accretion-to-autoconversion ratio. The increase in the accretion-to-autoconversion ratio may be a necessary condition for the susceptibility decrease, but it is not a sufficient condition.

Because of remaining discrepancies between the observation and model, we also find, with somewhat reduced confidence, that S_R slightly decreases with increasing LWP (Fig. 4.1a). We find this when we calculate S_R using data taken from all the examined regions, which largely encompass the tropical and subtropical Pacific. In a regional breakdown of S_R,

there exists a more pronounced decrease with increasing LWP in some regions, while a few others show a peak at intermediate LWPs. Certain behaviors, however, are shared across all regions. First, S_{POP} decreases with increasing LWP in all regions. Second, S_I slightly increases with LWP before reaching a plateau in most regions. Consistent with results from Terai et al. [2012], S_{POP} and S_I are largely additive to produce S_R in all regions. The difference in S_R, S_{POP}, and S_I values across different regions is not surprising, given that we find that susceptibility varies with LWP and N_{eff}. S_{POP} values are highest at low LWP and low N_{eff}, but decrease towards zero at high LWP and low N_{eff} and at low LWP and high N_{eff} (Fig. 4.6). This pattern does not show up if we examine the susceptibility in the diagnostic model with perturbed physics, in which S_{POP} is highest at low LWP and high N_{d} and decreases both with increasing LWP and decreasing N_{d}. This shows that although the diagnostic model is able to capture the satellite-observed S_{POP} with increasing LWP, it does not simulate the adequate processes to accurately capture the aerosol-cloud interaction. We come to the same conclusion when we compare the actual POP values as a function of N_{eff} in the satellite retrievals and model outputs (Fig. 4.7).

Finally, we are left with a couple of questions that cannot be addressed in the scope of this study. First, we cannot explain the negative S_I values that we find at low LWP when we examine the satellite data over the entire domain. No regional areas exhibit significant negative S_I and the negative values are substantial only in the far northeast Pacific and equatorial cold tongue regions. The more pronounced negative S_I in these two regions might be attributable to the large proportion of low LWP clouds, as is suggested in Fig. 2b of K09. Indeed, an examination of S_I as a function of LWP and N_{eff}, as in Fig. 4.6 show that S_I is negative at low LWP and high N_{eff}. The distribution of LWP and N_{eff}, however, does not completely explain regional differences, because the VOCALS southeast Pacific region also includes a large proportion of low LWP clouds. So the aggregation of data might explain the negative S_I values when we examine the satellite data over the entire domain, as was similarly found by McComiskey and Feingold [2012].

Second, we find that there is increasing agreement in how S_{POP} varies with LWP and that the values appear to be on the order of $\sim$1 at LWPs near the minimum needed to generate stratocumulus precipitation, decreasing to zero at much higher LWPs. However,

we have not addressed whether S_{POP} is a useful metric that can differentiate models with strong aerosol-cloud interactions from those with weak aerosol-cloud interactions. The three GCM study of Wang et al. [2012] suggests that S_{POP} is a useful metric to distinguish the strength of aerosol indirect effect. The large eddy simulation study of Lebo and Feingold [2014] suggest that the relationship between S_{POP} and cloud response depends on whether stratocumulus or cumulus regimes are examined. Further studies are necessary to diagnose why S_{POP} values distinguish cloud responses better than S_R as Wang et al. [2012] had found, and how it varies with models of varying complexities. Because precipitation susceptibility is an easier metric to measure in the current climate, compared to the total response of clouds to aerosol perturbations, if a physical mechanism can link strong precipitation susceptibilities to cloud responses in models, the susceptibility can indeed be a useful metric that helps to constrain the existing uncertainty in aerosol-cloud interactions among GCMs.

Chapter 5

CONCLUSIONS AND FUTURE WORK

5.1 Summary

In this dissertation a variety of observations, from in situ and remote sensing aircraft measurements to satellite cloud and precipitation retrievals, and a variety of simple models were employed to investigate the physical processes in stratocumulus-topped boundary layers.

In characterizing pockets of open cells (POCs) in Chapter 2, it was found that POCs form within a wide variety of large scale meteorological and aerosol conditions, and no particular large scale condition appeared to constrain where POCs were observed by the C-130. This finding lends support to our understanding that POCs are largely maintained by the reinforcement of processes that are internal to the boundary layer and the clouds that form within it. We also found that despite the variety of conditions in which they are observed, they all share particular properties, such as the preponderance of high precipitation rates, the existence of an ultraclean layer, and a narrow range of accumulation-mode aerosol concentrations in the subcloud layer.

In examining the cloud microphysical processes in Chapter 3, the rates at which cloud water mass is converted into drizzle water mass and the rates at which aerosol concentrations are reduced through in-cloud collision-coalescence properties were quantified. A comparison of autoconversion and accretion revealed that accretion rates are nearly two orders of magnitude higher than autoconversion rates in shifting cloud water to drizzle water. When evaluating the influence on collision-coalescence loss rates of cloud drops, it was found that accretion also dominates autoconversion in reducing cloud droplets number concentration, and that self-collection of cloud drops is more important than autoconversion. Although the reduced aerosol concentrations within the POC might suggest higher cloud droplet number loss rates in the POC, this was not always observed. Instead, because the cloud droplet number concentrations are lower in the POC, the time scales at which all cloud droplets

may be collected are much shorter in the POC. A series of experiments conducted with a parcel model with bin microphysics also showed that due to the reduced cloud droplet number concentrations in the POC, fairly high supersaturations ($\sim$0.4 %) can be reached with pretty low updraft speeds (0.15 m s^{-1}) even in the middle of the cloud. This can potentially lead to the activation of more interstitial aerosols and may be important in achieving the very clean conditions of the ultraclean layer.

Finally, examining the precipitation susceptibility metric in a wide variety of marine stratocumulus using satellite retrievals in Chapter 4 revealed an increasing agreement among observations that the susceptibility of the probability of precipitation (S_{POP}) decreases with increased cloud liquid water path (LWP) and that the mean susceptibility has a value of approximately 1. A comparison between the susceptibilities calculated from the satellite retrievals and those from a column model with the diagnostic treatment of precipitation showed that they both agree in the behavior of S_{POP} with LWP. Examining the susceptibility as a function of not only LWP but also cloud droplet number concentration (N_d) revealed that susceptibility is also a function of N_d. These can lead to discrepancies amongst different estimates of susceptibilities calculated from stratocumulus with different ranges of LWP and cloud droplet number concentrations.

5.2 Remaining questions and going forward

A series of questions and puzzles arise from the results presented above. First, we are unable to sufficiently explain why the subcloud accumulation-mode aerosol concentrations in the POC have such a narrow range, when compared to the variety of concentrations in the overcast region surrounding the POCs. A balance between sources and sinks appears to exist at such concentrations of accumulation-mode aerosols, but the exact mechanisms that maintain this balance were not identified. Because large eddy simulations (LES) of POC-like features also show similar aerosol concentrations in the subcloud layer, a series of experiments with LES where surface wind speeds are varied or where surface source rates of accumulation-mode aerosols are altered will be necessary to address this question.

Whereas the conditions in which POCs exist and are maintained have been identified in Chapter 2 and 3, the way in which they form and the conditions that lead to POC

formation have not been addressed here. Painter [2012] examined satellite retrievals of LWP and N_d to address this question. Although conditions favoring heavy drizzle appeared to tie formation mechanisms of all five POCs, Painter [2012] found that POCs do not form under one particular condition and that a variety of conditions may induce the heavy drizzle necessary to initiate POC formation. Although the LES work of Berner et al. [2013] showed that certain boundary layer conditions can lead to the transition of clouds from closed-cell to open-cell, a large-domain simulation will be necessary to test whether POC formation can be simulated with observed meteorological and aerosol conditions and whether POCs are features that can be forecast with much skill.

Although the microphysical process rates have been estimated from the observed droplet size distributions in POCs and the surrounding clouds, what has not been done here is a close comparison between the process rates and DSDs of the C-130 observations and those obtained from the LES. For example, early comparisons between precipitation rate and bulk drizzle water mixing ratios showed that the observations and LES do not agree. Since then, changes have been made to improve the representation of drop fall velocities within the LES, so further comparisons will be useful to verify whether the observations and LES agree now. These sensitivities and differences will be important if we are interested in identifying and mapping out the boundary layer conditions in which POCs are able to form.

LES may also be employed to extend the comparison between active and quiescent clouds. A preliminary examination of the LES fields suggests active and quiescent clouds form within the LES POCs as they do in observations. This provides a useful avenue to address the questions on their formation, maintenance, and role in maintaining the POC boundary layer characteristics.

Questions also arise from our susceptibility work. First, satellite retrievals reveal negative susceptibility of precipitation intensity (S_I) at low LWPs. This runs counter to our understanding of how cloud droplet number concentrations influence precipitation rates. The possibility exists that data aggregation is leading to these negative S_I values (analogous to what McComiskey and Feingold [2012] found with ACI) and that retrievals biases exist at low LWP, where MODIS cloud retrievals of effective radius are less reliable. Sampling the data by meteorological context and more investigation into the conditions in which

negative S_I are possible will be necessary to tackle this puzzle.

Another issue that remains unresolved after this susceptibility study is the discrepancy between the behavior of susceptibility found by Sorooshian et al. [2009], Jiang et al. [2010], and Duong et al. [2011] and the behavior found by Wood et al. [2009], Terai et al. [2012], Mann et al. [2014], and Chapter 4 of this study. Given that the first set of studies focused on cumulus precipitation and the second set, on stratocumulus precipitation, it is likely that the precipitation formation mechanisms in the two types of clouds are different such that they lead to different susceptibility behaviors. Feingold et al. [2013] imply that the timescales at which precipitation forms is a likely explanation for the discrepancy, but their study did not take into account the vertical distribution and development of precipitation.

Finally, while the susceptibility metric appears to be a useful metric to compare the sensitivity of precipitation to aerosol perturbations in a variety of observations and model outputs, it would be even more useful if it is able to differentiate models with high sensitivity of clouds to aerosol perturbations (high ACI) from those that have low ACI. The modeling study of Wang et al. [2012] appears to indicate that this is the case, based on their comparison of three general circulation models (GCMs). On the other hand, Lebo and Feingold [2014] indicate that these relationships may differ with the cloud regime that is examined. Again, further investigation is necessary to test whether susceptibility can be used as a metric to constrain the aerosol indirect effect in GCMs.

The ultimate goal of this series of work is to constrain the effect that aerosols have on determining the observed cloud properties. Advances in understanding the aerosol-cloud-precipitation interaction will be necessary as an increasing number of GCMs and weather forecast models incorporate processes that involve the interaction between aerosols, clouds, and precipitation. Much work remains to help bridge the understanding from observations with those of large scale models using a combination of simple models and complex cloud resolving models and to identify useful diagnostics that can help improve the models' representation of subgrid processes.

BIBLIOGRAPHY

S. J. Abel, D. N. Walters, and G. Allen. Evaluation of stratocumulus cloud prediction in the Met Office forecast model during VOCALS-REx. *Atmospheric Chemistry and Physics*, 10(21):10541–10559, November 2010. ISSN 1680-7324. doi: 10.5194/acp-10-10541-2010.

B. A. Albrecht. Aerosols, cloud microphysics, and fractional cloudiness. *Science*, 245(4923): 1227–1230, 1989.

G. Allen, H. Coe, A. Clarke, C. S. Bretherton, R. Wood, S. J. Abel, P. Barrett, P. Brown, R. George, S. Freitag, C. McNaughton, S. Howell, L. Shank, V. Kapustin, V. Brekhovskikh, L. Kleinman, Y.-N. Lee, S. Springston, T. Toniazzo, R. Krejci, J. Fochesatto, G. Shaw, P. Krecl, B. Brooks, G. McMeeking, K. N. Bower, P. I. Williams, J. Crosier, I. Crawford, P. Connolly, J. D. Allan, D. Covert, a. R. Bandy, L. M. Russell, J. Trembath, M. Bart, J. B. McQuaid, J. Wang, and D. Chand. South East Pacific atmospheric composition and variability sampled along 20 S during VOCALS-REx. *Atmospheric Chemistry and Physics*, 11(11):5237–5262, June 2011. ISSN 1680-7324. doi: 10.5194/acp-11-5237-2011.

G. Allen, G. Vaughan, T. Toniazzo, H. Coe, P. Connolly, S. E. Yuter, C. D. Burleyson, P. Minnis, and J. K. Ayers. Gravity-wave-induced perturbations in marine stratocumulus. *Quarterly Journal of the Royal Meteorological Society*, 139(670):32–45, January 2013. ISSN 00359009. doi: 10.1002/qj.1952.

BW Atkinson and J.W. Zhang. Mesoscale shallow convection in the atmosphere. *Reviews of Geophysics*, 34(4):403–431, 1996.

P. H. Austin, S. Siems, and Y. Wang. Constraints on droplet growth in radiatively cooled stratocumulus clouds. *Journal of Geophysical Research*, 100(D7):14231–14242, 1995. ISSN 0148-0227. doi: 10.1029/95JD01268.

M. B. Baker and R. J. Charlson. Bistability of CCN concentrations and thermodynamics in the cloud-topped boundary layer. *Nature*, 345(6271):142–145, 1990.

R. Bennartz. Global assessment of marine boundary layer cloud droplet number concentration from satellite. *Journal of Geophysical Research*, 112(D2):D02201, January 2007. ISSN 0148-0227. doi: 10.1029/2006JD007547.

A. H. Berner, C. S. Bretherton, and R. Wood. Large-eddy simulation of mesoscale dynamics and entrainment around a pocket of open cells observed in VOCALS-REx RF06. *Atmospheric Chemistry and Physics*, 11(20):10525–10540, October 2011. ISSN 1680-7324. doi: 10.5194/acp-11-10525-2011.

A. H. Berner, C. S. Bretherton, R. Wood, and A. Muhlbauer. Marine boundary layer cloud regimes and POC formation in a CRM coupled to a bulk aerosol scheme. *Atmospheric Chemistry and Physics*, 13(24):12549–12572, December 2013. ISSN 1680-7324. doi: 10.5194/acp-13-12549-2013.

A. Bott. A Flux Method for the Numerical Solution of the Stochastic Collection Equation. *Journal of the Atmospheric Sciences*, 55(13):2284–2293, July 1998. ISSN 0022-4928. doi: 10.1175/1520-0469(1998)055¡2284:AFMFTN¿2.0.CO;2.

O. Boucher, D. Randall, P. Artaxo, C. Bretherton, G. Feingold, P. Forster, V.-M. Kerminen, Y. Kondo, H. Liao, U. Lohmann, U. XRasch, S.K. Satheesh, S. Sherwood, B. Stevens, and X.Y. Zhang. Clouds and Aerosols. In T.F. Stocker, editor, *Climate Change 2013: The Physical Science Basis. Contribution of Working Group I to the Fifth Assessment Report of the Intergovernmental Panel on Climate Change*, chapter Clouds and. Cambridge University Press, New York, NY, 2013.

C. S. Bretherton, R. Wood, R. C. George, D. Leon, G. Allen, and X. Zheng. Southeast Pacific stratocumulus clouds, precipitation and boundary layer structure sampled along 20 S during VOCALS-REx. *Atmospheric Chemistry and Physics*, 10(21):10639–10654, November 2010. ISSN 1680-7324. doi: 10.5194/acp-10-10639-2010.

Christopher S. Bretherton, Taneil Uttal, Christopher W. Fairall, Sandra E. Yuter, Robert a. Weller, Darrel Baumgardner, Kimberly Comstock, Robert Wood, and Graciela B. Raga. The Epic 2001 Stratocumulus Study. *Bulletin of the American Meteorological Society*, 85 (7):967–977, July 2004. ISSN 0003-0007. doi: 10.1175/BAMS-85-7-967.

Casey D. Burleyson, Simon P. de Szoeke, Sandra E. Yuter, Matt Wilbanks, and W. Alan Brewer. Ship-Based Observations of the Diurnal Cycle of Southeast Pacific Marine Stratocumulus Clouds and Precipitation. *Journal of the Atmospheric Sciences*, 70(12):3876–3894, December 2013. ISSN 0022-4928. doi: 10.1175/JAS-D-13-01.1.

P. Caldwell and C. S. Bretherton. Large Eddy Simulation of the Diurnal Cycle in Southeast Pacific Stratocumulus. *Journal of the Atmospheric Sciences*, 66(2):432–449, February 2009. ISSN 0022-4928. doi: 10.1175/2008JAS2785.1.

A. Clarke, C. McNaughton, V. Kapustin, Y. Shinozuka, S. Howell, J. Dibb, J. Zhou, B. Anderson, V. Brekhovskikh, H. Turner, and M. Pinkerton. Biomass burning and pollution aerosol over North America: Organic components and their influence on spectral optical properties and humidification response. *Journal of Geophysical Research*, 112(D12): D12S18, June 2007. ISSN 0148-0227. doi: 10.1029/2006JD007777.

A. D. Clarke, S. R. Owens, and J. Zhou. An ultrafine sea-salt flux from breaking waves: Implications for cloud condensation nuclei in the remote marine atmosphere. *Journal of Geophysical Research*, 111(D6):1–14, 2006. ISSN 0148-0227. doi: 10.1029/2005JD006565.

. K. Comstock, S. E. Yuter, R. Wood, and C. S. Bretherton. The Three-Dimensional Structure and Kinematics of Drizzling Stratocumulus. *Monthly Weather Review*, 135 (11):3767–3784, November 2007. ISSN 0027-0644. doi: 10.1175/2007MWR1944.1.

K. K. Comstock, R. Wood, S. E. Yuter, and C. S. Bretherton. Reflectivity and rain rate in and below drizzling stratocumulus. *Quarterly Journal of the Royal Meteorological Society*, 130(603):2891–2918, October 2004. ISSN 00359009. doi: 10.1256/qj.03.187.

Z. Cui, A. Gadian, A. Blyth, J. Crosier, and I. Crawford. Observations of the variation in aerosol and cloud microphysics along the 20 S transect on 13 November 2008 during

VOCALS-REx. *Journal of the Atmospheric Sciences*, (November 2008):140421131926008, April 2014. ISSN 0022-4928. doi: 10.1175/JAS-D-13-0245.1.

M. H. Davis. Collisions of Small Cloud Droplets: Gas Kinetic Effects. *Journal of the Atmospheric Sciences*, 29(5):911–915, 1972. ISSN 0022-4928. doi: 10.1175/1520-0469(1972)029<0911:COSCDG>2.0.CO;2.

G. de Leeuw, E. L. Andreas, M. D. Anguelova, C. W. Fairall, E. R Lewis, M. Dowd, C. O .and Schulz, and S. E Schwartz. Production flux of sea spray aerosol. (2010):1–39, 2011. doi: 10.1029/2010RG000349.1.INTRODUCTION.

S. P. de Szoeke, S. Yuter, D. Mechem, C. W. Fairall, C. D. Burleyson, and P. Zuidema. Observations of Stratocumulus Clouds and Their Effect on the Eastern Pacific Surface Heat Budget along 20S. *Journal of Climate*, 25(24):8542–8567, December 2012. ISSN 0894-8755. doi: 10.1175/JCLI-D-11-00618.1.

H. T. Duong, A. Sorooshian, and G. Feingold. Investigating potential biases in observed and modeled metrics of aerosol-cloud-precipitation interactions. *Atmospheric Chemistry and Physics*, 11(9):4027–4037, 2011. doi: 10.5194/acp-11-4027-2011.

Ryan Eastman, Stephen G. Warren, and Carole J. Hahn. Variations in Cloud Cover and Cloud Types over the Ocean from Surface Observations, 19542008. *Journal of Climate*, 24(22):5914–5934, November 2011. doi: 10.1175/2011JCLI3972.1.

Graham Feingold and Holger Siebert. Cloud Aerosol Interactions from the Micro to the Cloud Scale. In *Clouds in the Perturbed Climate System: Their Relationship to Energy Balance, Atmospheric Dynamics, and Precipitation*, pages 319–338. 2009. ISBN 9780262012874.

Graham Feingold, Allison McComiskey, Daniel Rosenfeld, and Armin Sorooshian. On the relationship between cloud contact time and precipitation susceptibility to aerosol. *Journal of Geophysical Research: Atmospheres*, 118(18):10,544–10,554, September 2013. ISSN 2169897X. doi: 10.1002/jgrd.50819.

Michael J. Garay, Roger Davies, Clare Averill, and James a. Westphal. ACTINOFORM CLOUDS: Overlooked Examples of Cloud Self-Organization at the Mesoscale. *Bulletin of the American Meteorological Society*, 85(10):1585–1594, October 2004. ISSN 0003-0007. doi: 10.1175/BAMS-85-10-1585.

R. C. George and R. Wood. Subseasonal variability of low cloud radiative properties over the southeast Pacific Ocean. *Atmospheric Chemistry and Physics*, 10(8):4047–4063, April 2010. ISSN 1680-7324. doi: 10.5194/acp-10-4047-2010.

R. C. George, R. Wood, C. S. Bretherton, and G. Painter. Development and impact of hooks of high droplet concentration on remote southeast Pacific stratocumulus. *Atmospheric Chemistry and Physics*, 13(13):6305–6328, July 2013. ISSN 1680-7324. doi: 10.5194/acp-13-6305-2013.

A. Gettelman, H. Morrison, C. R. Terai, and R. Wood. Microphysical process rates and global aerosolcloud interactions. *Atmospheric Chemistry and Physics*, 13(19):9855–9867, October 2013. ISSN 1680-7324. doi: 10.5194/acp-13-9855-2013.

Steven J. Ghan and Richard C. Easter. Computationally Efficient Approximations to Stratiform Cloud Microphysics Parameterization. *Monthly Weather Review*, 120(8):1572–1582, August 1992. ISSN 0027-0644. doi: 10.1175/1520-0493(1992)120¡1572:CEATSC¿2.0.CO;2.

Jean-Christophe Golaz, Marc Salzmann, Leo J. Donner, Larry W. Horowitz, Yi Ming, and Ming Zhao. Sensitivity of the Aerosol Indirect Effect to Subgrid Variability in the Cloud Parameterization of the GFDL Atmosphere General Circulation Model AM3. *Journal of Climate*, 24(13):3145–3160, July 2011. ISSN 0894-8755. doi: 10.1175/2010JCLI3945.1.

E. Gryspeerdt, P. Stier, and D. G. Partridge. Satellite observations of cloud regime development: the role of aerosol processes. *Atmospheric Chemistry and Physics*, 14(3): 1141–1158, February 2014. ISSN 1680-7324. doi: 10.5194/acp-14-1141-2014.

William D. Hall. A Detailed Microphysical Model Within a Two-Dimensional Dynamic Framework: Model Description and Preliminary Results. *Journal of the Atmospheric*

Sciences, 37(11):2486–2507, November 1980. ISSN 0022-4928. doi: 10.1175/1520-0469(1980)037¡2486:ADMMWA¿2.0.CO;2.

Hongli Jiang, Graham Feingold, and Armin Sorooshian. Effect of Aerosol on the Susceptibility and Efficiency of Precipitation in Warm Trade Cumulus Clouds. *Journal of the Atmospheric Sciences*, 67(11):3525–3540, November 2010. ISSN 0022-4928. doi: 10.1175/2010JAS3484.1.

P. R. Jonas. The collision efficiency of small drops. *Quarterly Journal of the Royal Meteorological Society*, 98(417):681–683, 1972. doi: 10.1002/qj.49709841717.

C. R. Jones, C. S. Bretherton, and D. Leon. Coupled vs. decoupled boundary layers in VOCALS-REx. *Atmospheric Chemistry and Physics*, 11(14):7143–7153, July 2011. ISSN 1680-7324. doi: 10.5194/acp-11-7143-2011.

J. Kazil, H. Wang, G. Feingold, A. D. Clarke, J. R. Snider, and A. R. Bandy. Modeling chemical and aerosol processes in the transition from closed to open cells during VOCALS-REx. *Atmospheric Chemistry and Physics*, 11(15):7491–7514, August 2011. ISSN 1680-7324. doi: 10.5194/acp-11-7491-2011.

Marat Khairoutdinov and Yefim Kogan. A New Cloud Physics Parameterization in a Large-Eddy Simulation Model of Marine Stratocumulus. *Monthly Weather Review*, 128(1):229–243, January 2000. ISSN 0027-0644. doi: 10.1175/1520-0493(2000)128¡0229:ANCPPI¿2.0.CO;2.

S. A. Klein and D. L. Hartmann. The Seasonal Cycle of Low Stratiform Clouds. *Journal of Climate*, 6(8):1587–1606, August 1993. ISSN 0894-8755. doi: 10.1175/1520-0442(1993)006¡1587:TSCOLS¿2.0.CO;2.

P. Kollias, C. W. Fairall, P. Zuidema, J. Tomlinson, and G. A. Wick. Observations of marine stratocumulus in SE Pacific during the PACS 2003 cruise. *Geophysical Research Letters*, 31(22):3–6, 2004. ISSN 0094-8276. doi: 10.1029/2004GL020751.

Terence L. Kubar, Dennis L. Hartmann, and Robert Wood. Understanding the Importance of Microphysics and Macrophysics for Warm Rain in Marine Low Clouds. Part I: Satellite

Observations. *Journal of the Atmospheric Sciences*, 66(10):2953–2972, October 2009. ISSN 0022-4928. doi: 10.1175/2009JAS3071.1.

Vincent E. Larson, Robert Wood, Paul R. Field, Jean-Christophe Golaz, Thomas H. Vonder Haar, and William R. Cotton. Systematic Biases in the Microphysics and Thermodynamics of Numerical Models That Ignore Subgrid-Scale Variability. *Journal of the Atmospheric Sciences*, 58(9):1117–1128, May 2001. ISSN 0022-4928. doi: 10.1175/1520-0469(2001)058¡1117:SBITMA¿2.0.CO;2.

Z. J. Lebo and G. Feingold. *On the relationship between responses in cloud water and precipitation to changes in aerosol*, volume 14. May 2014. ISBN 1413233201. doi: 10.5194/acpd-14-13233-2014.

Tristan S. L'Ecuyer, Wesley Berg, John Haynes, Matthew Lebsock, and Toshihiko Takemura. Global observations of aerosol impacts on precipitation occurrence in warm maritime clouds. *Journal of Geophysical Research*, 114(D9):1–15, May 2009. ISSN 0148-0227. doi: 10.1029/2008JD011273.

D. C. Leon, Z. Wang, and D. Liu. Climatology of drizzle in marine boundary layer clouds based on 1 year of data from CloudSat and Cloud-Aerosol Lidar and Infrared Pathfinder Satellite Observations (CALIPSO). *Journal of Geophysical Research*, 113, November 2008. ISSN 0148-0227. doi: 10.1029/2008JD009835.

Julian a. L. Mann, J. Christine Chiu, Robin J. Hogan, Ewan J. O'Connor, Tristan S. L'Ecuyer, Thorwald H. M. Stein, and Anne Jefferson. Aerosol impacts on drizzle properties in warm clouds from ARM Mobile Facility maritime and continental deployments. *Journal of Geophysical Research: Atmospheres*, pages n/a–n/a, April 2014. ISSN 2169897X. doi: 10.1002/2013JD021339.

G. M. Martin, D. W. Johnson, and A. Spice. The measurement and parameterization of effective radius of droplets in warm stratocumulus clouds. *Journal of Atmospheric Sciences*, 51:1823–1842, 1994.

Guillaume S. Mauger and Joel R. Norris. Meteorological bias in satellite estimates of aerosol-cloud relationships. *Geophysical Research Letters*, 34(16):1–5, August 2007. ISSN 0094-8276. doi: 10.1029/2007GL029952.

A. McComiskey and G. Feingold. The scale problem in quantifying aerosol indirect effects. *Atmospheric Chemistry and Physics*, 12(2):1031–1049, January 2012. ISSN 1680-7324. doi: 10.5194/acp-12-1031-2012.

David B. Mechem and Yefim L. Kogan. Simulating the Transition from Drizzling Marine Stratocumulus to Boundary Layer Cumulus with a Mesoscale Model. *Monthly Weather Review*, 131(10):2342–2360, October 2003. ISSN 0027-0644. doi: 10.1175/1520-0493(2003)131¡2342:STTFDM¿2.0.CO;2.

David B. Mechem, Sandra E. Yuter, and Simon P. de Szoeke. Thermodynamic and Aerosol Controls in Southeast Pacific Stratocumulus. *Journal of the Atmospheric Sciences*, 69(4): 1250–1266, April 2012. doi: 10.1175/JAS-D-11-0165.1.

C. R. Mechoso, R. Wood, R. Weller, C. S. Bretherton, a. D. Clarke, H. Coe, C. Fairall, J. T. Farrar, G. Feingold, R. Garreaud, C. Grados, J. McWilliams, S. P. de Szoeke, S. E. Yuter, and P. Zuidema. OceanCloudAtmosphereLand Interactions in the Southeastern Pacific: The VOCALS Program. *Bulletin of the American Meteorological Society*, 95(3): 357–375, March 2014. ISSN 0003-0007. doi: 10.1175/BAMS-D-11-00246.1.

Hugh Morrison and Andrew Gettelman. A New Two-Moment Bulk Stratiform Cloud Microphysics Scheme in the Community Atmosphere Model, Version 3 (CAM3). Part I: Description and Numerical Tests. *Journal of Climate*, 21(15):3642–3659, August 2008. ISSN 0894-8755. doi: 10.1175/2008JCLI2105.1.

A. Muhlbauer, I. L. McCoy, and R. Wood. Climatology of stratocumulus cloud morphologies: microphysical properties and radiative effects. *Atmospheric Chemistry and Physics*, 14(13):6695–6716, July 2014. ISSN 1680-7324. doi: 10.5194/acp-14-6695-2014.

Teruyuki Nakajima, Akiko Higurashi, Kazuaki Kawamoto, and Joyce E Penner. A possible

correlation between satellitederived cloud and aerosol microphysical parameters. *Geophysical Research Letters*, 28(7):1171, 2001. ISSN 0094-8276. doi: 10.1029/2000GL012186.

G. M. Painter. A Lagrangian Study of Southeast Pacific Boundary Layer Clouds. Master's thesis, University of Washington, 2012.

Hanna Pawlowska. An observational study of drizzle formation in stratocumulus clouds for general circulation model (GCM) parameterizations. *Journal of Geophysical Research*, 108(D15):1–13, 2003. ISSN 0148-0227. doi: 10.1029/2002JD002679.

Markus D. Petters, Jefferson R. Snider, Bjorn Stevens, Gabor Vali, Ian Faloona, and Lynn M. Russell. Accumulation mode aerosol, pockets of open cells, and particle nucleation in the remote subtropical Pacific marine boundary layer. *Journal of Geophysical Research*, 111(D2):1–15, 2006. ISSN 0148-0227. doi: 10.1029/2004JD005694.

R Posselt and U Lohmann. Introduction of prognostic rain in ECHAM5: design and single column model simulations. *Atmospheric Chemistry and Physics*, 8(11):2949–2963, June 2008. ISSN 1680-7324. doi: 10.5194/acp-8-2949-2008.

J. Quaas, Y. Ming, S. Menon, T. Takemura, M. Wang, J. E. Penner, a. Gettelman, U. Lohmann, N. Bellouin, O. Boucher, a. M. Sayer, G. E. Thomas, a. McComiskey, G. Feingold, C. Hoose, J. E. Kristjánsson, X. Liu, Y. Balkanski, L. J. Donner, P. a. Ginoux, P. Stier, J. Feichter, I. Sednev, S. E. Bauer, D. Koch, R. G. Grainger, a. Kirkevå g, T. Iversen, Ø. Seland, R. Easter, S. J. Ghan, P. J. Rasch, H. Morrison, J.-F. Lamarque, M. J. Iacono, S. Kinne, and M. Schulz. Aerosol indirect effects general circulation model intercomparison and evaluation with satellite data. *Atmospheric Chemistry and Physics Discussions*, 9(3):12731–12779, June 2009. ISSN 1680-7375. doi: 10.5194/acpd-9-12731-2009.

Johannes Quaas, Olivier Boucher, Nicolas Bellouin, and Stefan Kinne. Satellite-based estimate of the direct and indirect aerosol climate forcing. *Journal of Geophysical Research*, 113(D5):D05204, March 2008. ISSN 0148-0227. doi: 10.1029/2007JD008962.

Leon D. Rotstayn and Yangang Liu. A smaller global estimate of the second indirect aerosol effect. *Geophysical Research Letters*, 32(5):4–7, 2005. ISSN 0094-8276. doi: 10.1029/2004GL021922.

P. E. Saide, S. N. Spak, G. R. Carmichael, M. a. Mena-Carrasco, Q. Yang, S. Howell, D. C. Leon, J. R. Snider, a. R. Bandy, J. L. Collett, K. B. Benedict, S. P. de Szoeke, L. N. Hawkins, G. Allen, I. Crawford, J. Crosier, and S. R. Springston. Evaluating WRF-Chem aerosol indirect effects in Southeast Pacific marine stratocumulus during VOCALS-REx. *Atmospheric Chemistry and Physics*, 12(6):3045–3064, March 2012. ISSN 1680-7324. doi: 10.5194/acp-12-3045-2012.

Verica Savic-Jovcic and Bjorn Stevens. The Structure and Mesoscale Organization of Precipitating Stratocumulus. *Journal of the Atmospheric Sciences*, 65(5):1587–1605, May 2008. ISSN 0022-4928. doi: 10.1175/2007JAS2456.1.

J. H. Seinfeld and S. N. Pandis. *Atmospheric chemistry and physics: From air pollution to climate change*. John Wiley, New York, 2nd edition edition, 2006.

Tarah M. Sharon, Bruce A. Albrecht, Haflidi H. Jonsson, Patrick Minnis, Mandana M. Khaiyer, Timothy M. van Reken, John Seinfeld, and Rick Flagan. Aerosol and Cloud Microphysical Characteristics of Rifts and Gradients in Maritime Stratocumulus Clouds. *Journal of the Atmospheric Sciences*, 63(3):983–997, March 2006. ISSN 0022-4928. doi: 10.1175/JAS3667.1.

William L. Smith, R. O. Knuteson, H. E. Revercomb, W. Feltz, N. R. Nalli, H. B. Howell, W. P. Menzel, Otis Brown, James Brown, Peter Minnett, and Walter McKeown. Observations of the Infrared Radiative Properties of the OceanImplications for the Measurement of Sea Surface Temperature via Satellite Remote Sensing. *Bulletin of the American Meteorological Society*, 77(1):41–51, January 1996. ISSN 0003-0007. doi: 10.1175/1520-0477(1996)077¡0041:OOTIRP¿2.0.CO;2.

Armin Sorooshian, Graham Feingold, Matthew D. Lebsock, Hongli Jiang, and Graeme L.

Stephens. On the precipitation susceptibility of clouds to aerosol perturbations. *Geophysical Research Letters*, 36(13):1–5, July 2009. ISSN 0094-8276. doi: 10.1029/2009GL038993.

Armin Sorooshian, Graham Feingold, M.D. Lebsock, Hongli Jiang, and G.L. Stephens. Deconstructing the precipitation susceptibility construct: Improving methodology for aerosol-cloud precipitation studies. *Journal of Geophysical Research*, 115(D17):D17201, 2010. doi: 10.1029/2009JD013426.

Graeme L. Stephens, Tristan L'Ecuyer, Richard Forbes, Andrew Gettlemen, Jean-Christophe Golaz, Alejandro Bodas-Salcedo, Kentaroh Suzuki, Philip Gabriel, and John Haynes. Dreary state of precipitation in global models. *Journal of Geophysical Research*, 115(D24):1–13, December 2010. ISSN 0148-0227. doi: 10.1029/2010JD014532.

Bjorn Stevens, Gabor Vali, Kimberly Comstock, Robert Wood, Margreet C. Van Zanten, Philip H. Austin, Christopher S. Bretherton, and Donald H. Lenschow. Pockets of Open Cells and Drizzle in Marine Stratocumulus. *Bulletin of the American Meteorological Society*, 86(1):51–57, January 2005. ISSN 0003-0007. doi: 10.1175/BAMS-86-1-51.

C. R. Terai and R. Wood. Aircraft observations of cold pools under marine stratocumulus. *Atmospheric Chemistry and Physics*, 13(19):9899–9914, October 2013. ISSN 1680-7324. doi: 10.5194/acp-13-9899-2013.

C. R. Terai, R. Wood, D. C. Leon, and P. Zuidema. Does precipitation susceptibility vary with increasing cloud thickness in marine stratocumulus? *Atmospheric Chemistry and Physics*, 12(10):4567–4583, May 2012. ISSN 1680-7324. doi: 10.5194/acp-12-4567-2012.

C. R. Terai, C. S. Bretherton, R. Wood, and G. Painter. Aircraft observations of five pockets of open cells sampled during VOCALS REx. *Atmospheric Chemistry and Physics Discussion*, 14:8287–8332, 2014. ISSN 1680-7324. doi: 10.5194/acpd-14-8287-20142.

Jason M. Tomlinson, Runjun Li, and Don R. Collins. Physical and chemical properties of the aerosol within the southeastern Pacific marine boundary layer. *Journal of Geophysical Research*, 112(D12):D12211, June 2007. ISSN 0148-0227. doi: 10.1029/2006JD007771.

T. Toniazzo, S. J. Abel, R. Wood, C. R. Mechoso, G. Allen, and L. C. Shaffrey. Large-scale and synoptic meteorology in the south-east Pacific during the observations campaign VOCALS-REx in austral Spring 2008. *Atmospheric Chemistry and Physics*, 11(10):4977–5009, May 2011. ISSN 1680-7324. doi: 10.5194/acp-11-4977-2011.

Jd Turton and S Nicholls. A study of the diurnal variation of stratocumulus using a multiple mixed layer model. *Quarterly Journal of the Royal Meteorological Society*, 113(477):969–1009, July 1987. ISSN 1477870X. doi: 10.1256/smsqj.47710.

M. C. VanZanten and Bjorn Stevens. Observations of the Structure of Heavily Precipitating Marine Stratocumulus. *Journal of the Atmospheric Sciences*, 62(12):4327–4342, December 2005. ISSN 0022-4928. doi: 10.1175/JAS3611.1.

M. C. VanZanten, B. Stevens, G. Vali, and D. H. Lenschow. Observations of Drizzle in Nocturnal Marine Stratocumulus. *Journal of the Atmospheric Sciences*, 62(1):88–106, January 2005. ISSN 0022-4928. doi: 10.1175/JAS-3355.1.

H. Wang, G. Feingold, R. Wood, and J. Kazil. Modelling microphysical and meteorological controls on precipitation and cloud cellular structures in Southeast Pacific stratocumulus. *Atmospheric Chemistry & Physics*, 10:6347–6362, 2010. doi: 10.5194/acp-10-6347-2010.

Hailong Wang and Graham Feingold. Modeling Mesoscale Cellular Structures and Drizzle in Marine Stratocumulus. Part I: Impact of Drizzle on the Formation and Evolution of Open Cells. *Journal of the Atmospheric Sciences*, 66(11):3237–3256, November 2009a. ISSN 0022-4928. doi: 10.1175/2009JAS3022.1.

Hailong Wang and Graham Feingold. Modeling Mesoscale Cellular Structures and Drizzle in Marine Stratocumulus. Part II: The Microphysics and Dynamics of the Boundary Region between Open and Closed Cells. *Journal of the Atmospheric Sciences*, 66(11):3257–3275, November 2009b. ISSN 0022-4928. doi: 10.1175/2009JAS3120.1.

Minghuai Wang, Steven Ghan, Xiaohong Liu, Tristan S. L'Ecuyer, Kai Zhang, Hugh Morrison, Mikhail Ovchinnikov, Richard Easter, Roger Marchand, Duli Chand, Yun Qian, and Joyce E. Penner. Constraining cloud lifetime effects of aerosols using A-Train satellite

observations. *Geophysical Research Letters*, 39(15):3–9, August 2012. ISSN 0094-8276. doi: 10.1029/2012GL052204.

R. Wood. Drizzle in Stratiform Boundary Layer Clouds. Part II: Microphysical Aspects. *Journal of the Atmospheric Sciences*, 62(9):3034–3050, September 2005. ISSN 0022-4928. doi: 10.1175/JAS3530.1.

R. Wood, K. K. Comstock, C. S. Bretherton, C. Cornish, J. Tomlinson, D. R. Collins, and C. Fairall. Open cellular structure in marine stratocumulus sheets. *Journal of Geophysical Research*, 113(D12):1–16, June 2008. ISSN 0148-0227. doi: 10.1029/2007JD009371.

R. Wood, C. S. Bretherton, D. Leon, A. D. Clarke, P. Zuidema, G. Allen, and H. Coe. An aircraft case study of the spatial transition from closed to open mesoscale cellular convection over the Southeast Pacific. *Atmospheric Chemistry and Physics*, 11(5):2341–2370, March 2011a. ISSN 1680-7324. doi: 10.5194/acp-11-2341-2011.

R. Wood, C. R. Mechoso, C. S. Bretherton, R. A. Weller, B. Huebert, F. Straneo, B. A. Albrecht, H. Coe, G. Allen, G. Vaughan, P. Daum, C. Fairall, D. Chand, L. Gallardo Klenner, R. Garreaud, C. Grados, D. S. Covert, T. S. Bates, R. Krejci, L. M. Russell, S. de Szoeke, A. Brewer, S. E. Yuter, S. R. Springston, A. Chaigneau, T. Toniazzo, P. Minnis, R. Palikonda, S. J. Abel, W. O. J. Brown, S. Williams, J. Fochesatto, J. Brioude, and K. N. Bower. The VAMOS Ocean-Cloud-Atmosphere-Land Study Regional Experiment (VOCALS-REx): goals, platforms, and field operations. *Atmospheric Chemistry and Physics*, 11(2):627–654, January 2011b. ISSN 1680-7324. doi: 10.5194/acp-11-627-2011.

Robert Wood. Rate of loss of cloud droplets by coalescence in warm clouds. *Journal of Geophysical Research*, 111(D21):1–6, November 2006. ISSN 0148-0227. doi: 10.1029/2006JD007553.

Robert Wood and Dennis L. Hartmann. Spatial Variability of Liquid Water Path in Marine Low Cloud: The Importance of Mesoscale Cellular Convection. *Journal of Climate*, 19 (9):1748–1764, May 2006. ISSN 0894-8755. doi: 10.1175/JCLI3702.1.

Robert Wood, Terence L. Kubar, and Dennis L. Hartmann. Understanding the Importance of Microphysics and Macrophysics for Warm Rain in Marine Low Clouds. Part II: Heuristic Models of Rain Formation. *Journal of the Atmospheric Sciences*, 66(10):2973–2990, October 2009. ISSN 0022-4928. doi: 10.1175/2009JAS3072.1.

M. Yang, B. W. Blomquist, and B. J. Huebert. Constraining the concentration of the hydroxyl radical in a stratocumulus-topped marine boundary layer from sea-to-air eddy covariance flux measurements of dimethylsulfide. *Atmospheric Chemistry and Physics Discussions*, 9(4):16267–16294, July 2009. ISSN 1680-7375. doi: 10.5194/acpd-9-16267-2009.

Q. Yang, J. D. Fast, H. Wang, R. C. Easter, H. Morrison, Y.-N. Lee, E. G. Chapman, S. N. Spak, and M. a. Mena-Carrasco. Assessing regional scale predictions of aerosols, marine stratocumulus, and their interactions during VOCALS-REx using WRF-Chem. *Atmospheric Chemistry and Physics*, 11(23):11951–11975, December 2011. ISSN 1680-7324. doi: 10.5194/acp-11-11951-2011.

Zhibo Zhang and Steven Platnick. An assessment of differences between cloud effective particle radius retrievals for marine water clouds from three MODIS spectral bands. *Journal of Geophysical Research*, 116(D20):D20215, October 2011. ISSN 0148-0227. doi: 10.1029/2011JD016216.

P. Zuidema, D. Leon, a. Pazmany, and M. Cadeddu. Aircraft millimeter-wave passive sensing of cloud liquid water and water vapor during VOCALS-REx. *Atmospheric Chemistry and Physics*, 12(1):355–369, January 2012. ISSN 1680-7324. doi: 10.5194/acp-12-355-2012.

Appendix A

COLLISION EFFICIENCIES AND EQUATIONS OF CONDENSATION SCHEME IN PARCEL MODEL

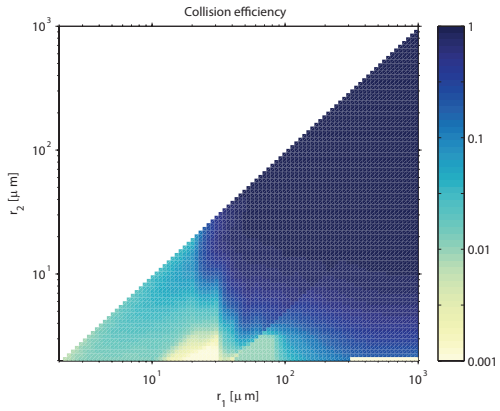

Figure A.1: The collision efficiencies used in the stochastic collection equation solver, based on Hall [1980], Davis [1972], and Jonas [1972]. Note that the color bar is in log-scale.

Condensation in these experiments is conducted by shifting the distribution by dr/dt at each one of the bins i. In these experiments, the curvature term and the solute term are not included, because I have only used a one-way advection of drops. The equations driving the condensation shift of drops are:

$$\frac{dr}{dt} = \frac{1}{r} G \left(S - 1 \right), \tag{A.1}$$

$$G = \left[\frac{\rho_w R_v T}{e_s D_v} + \frac{\rho_w L}{k_a T} \left(\frac{L}{R_v T} - 1 \right) \right]^{-1}, \tag{A.2}$$

$$\Delta r = \frac{dr}{dt} \Delta t, \tag{A.3}$$

$$\frac{dS}{dt} = Q_1 \frac{dz}{dt} - Q_2 \frac{d\chi}{dt}, \tag{A.4}$$

$$Q_1 = \frac{1}{T}\left[\frac{Lg}{R_v c_p T} - \frac{g}{R_d}\right], \tag{A.5}$$

$$Q_2 = \rho\left[\frac{R_v T}{e_s} - \frac{\epsilon L^2}{p c_p T}\right], \tag{A.6}$$

$$\frac{dN_i}{dt} = -\frac{N_i}{\Delta \ln r} G \frac{1}{r_i^2}(S-1) + \frac{N_{i-1}}{\Delta \ln r} G \frac{1}{r_{i-1}^2}(S-1), \tag{A.7}$$

$$\frac{d\chi}{dt} = \frac{4\pi\rho_w}{3\rho_a} \sum_i r_i^3 \frac{dN_i}{dt}, \tag{A.8}$$

where

- r is the radii of drops
- S is the ambient saturation ratio
- ρ_w is the density of water
- R_v is the gas constant for water
- T is the temperature
- e_s is the saturation vapor pressure of water
- D_v is the vapor diffusivity
- k_a is the thermal conductivity of air
- L is the latent heat of vaporization of water
- g is the standard gravity

- R_d is the gas constant of dry air
- ρ_a is the density of air
- c_p is the specific heat at constant pressure
- p is the ambient pressure
- $\epsilon = 0.622$
- N_i is the number concentration of drops over a given size range

Appendix B

CLOUDSAT/MODIS COMBINED DATASET AND LOCATION

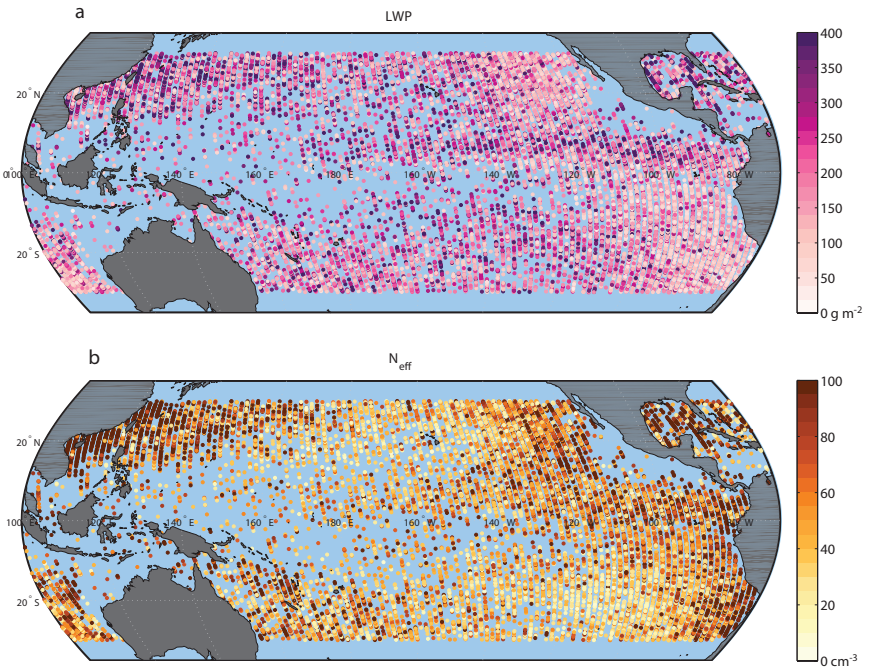

Figure B.1: The location of every 20 data points from the total CloudSat/MODIS combined dataset and the associated (a) LWP and (b) Neff retrievals are shown.

VITA

Christopher Terai is a graduate student who studies clouds. He attended St. Mary's International School, studied Physics at Amherst College, and studied Atmospheric Sciences at the University of Washington. One of his favorite things to do is to gaze at clouds out of airplane windows when he gets a chance to fly.